SISSA
Scuola
Internazionale
Superiore di
Studi Avanzati

Physics Area - PhD course in
Theory and Numerical Simulation of Condensed Matter

Quantum effects in glasses at ultra-low temperatures

Candidate:
Claudia Artiaco

Advisors:
Prof. Antonello Scardicchio
Prof. Michele Fabrizio

Academic Year 2020-2021

Abstract

Glasses at ultra-low temperatures present several puzzling phenomena. A notable example is the anomalous (i.e., non-Debye) behavior of thermodynamic quantities at temperatures lower than 1 K. A comprehensive quantum theory able to explain these phenomena has not been developed so far. In this thesis, we tackle this long-standing problem with different and innovative perspectives, employing various physical models, and several analytical and numerical techniques. We mainly explore two different but complementary approaches. In the first approach, we investigate the thermodynamics of models for ultra-low temperature glasses, with particular attention to mean-field models. Specifically, exploiting hard-sphere systems and constraint satisfaction problems as a minimal model for structural glasses, we explore their jamming transition both in the classical and the quantum regime. In the second approach, we focus on finite-dimensional models. We analyze the quantum dynamics of the two-level system model for glasses and generic many-body localized systems, providing clues for the presence of a deep connection between glasses and quantum many-body localized systems.

This thesis aims at estimating both qualitatively and quantitatively the effects of quantum mechanics on glasses at ultra-low temperatures. In the literature, only a few studies have considered glasses deep in their quantum regime, partly due to the analytical and computational challenges this posits. Nevertheless, this perspective promises to have wide-ranging applications. One of our ambitious goals is to take a first, substantial step to unveil the possible origin of long-standing discrepancies observed between theory and experiments in ultra-low temperature glasses. Moreover, we would like to predict the presence of new experimental regimes that might be interesting to investigate.

Acknowledgements

I warmly thank the external referees, Dmitry Abanin and Anushya Chandran, for offering their time and goodwill for reviewing my work.

I would like to thank my supervisors, Michele Fabrizio and Antonello Scardicchio, who supported me during my Ph.D. journey, offering me the possibility to deepen my knowledge and explore new fields every time I had the possibility to.

I owe special thanks to Giorgio Parisi, who has always inspired me with his brightness, intellectual curiosity, simplicity, and moral integrity.

I would like to thank my co-authors, with whom I spent a lot of fruitful time: Paolo Baldan, Federico Balducci, Andrea Nava, Markus Heyl, Federico Ricci-Tersenghi, Rafael Díaz Hernández Rojas and Angelo Russomanno.

A special thought goes to Angelo Giorgio Cavaliere, Francesca Franzon, and Davide Tisi, who have always helped me and with whom I hope to collaborate in the near future.

I would like to thank Jens Bardarson, Giuseppe Carleo, and Francesco Zamponi for giving me many opportunities.

I would also like to express my gratitude to my teachers, my fellow students and postdoctoral researchers at SISSA and ICTP. In particular, I would like to thank Thibaud Maimbourg and Valentina Ros, for sharing their knowledge and wisdom.

Contents

List of Figures

1. Introduction

In this Chapter, we briefly introduce the vast topic of glasses and present an overview of the low-temperature anomalies of structural glasses, i.e. glasses obtained by cooling a liquid. The first theoretical model aimed at explaining such anomalies, namely the two-level system model, is then discussed. We illustrate why it cannot be considered satisfactory, focusing in particular on the description of the discrepancies between its predictions and some experimental measurements. Finally, we discuss some recent, puzzling observations on vapor-deposited and hyperaged glasses.

Glasses are amorphous, disordered materials which, despite the lack of periodicity, are mechanically rigid like solids [1, 2, 4–14]. Specifically, in a glassy material the typical relaxation time scale becomes much larger than the typical duration of experimental measurements or numerical simulations. Adopting this definition, various systems can be considered glassy materials. Examples are: natural glasses, as obsidian, and structural glasses, as fused quartz (in the physics of liquids); type-II superconductors in the presence of disorder (in hard condensed matter); colloidal suspensions, emulsions, foams, and granular materials (in soft condensed matter); spin glasses (among abstract models). Glassy systems are therefore present at diverse time and length scales, as illustrated in Fig. 1.1a. One important common denominator of glassy systems is the presence of disorder, being it quenched, as in spin glasses, or self-induced, as in structural glasses. As a consequence, they all present a highly non-trivial energy landscape in the high dimensional space of configurations, composed of many minima and saddles. A pictorial illustration of it is shown in Fig. 1.1b. In some systems, e.g. spin glasses and hard spheres, the landscape has been found to be even more complex than expected, showing a fractal and hierarchical topology [15–17].

Systems approaching the glass transition do not show any appreciable change in their structure, despite a massive change in their dynamical properties. A clear signature of the incipience of the glass transition is the formation of two steps in the relaxation of dynamic correlation functions and the appearance of dynamical heterogeneities. In structural glasses, which are formed by cooling a liquid "fast enough" [11], both features appear approximately at $T \approx 1.2\,T_{\text{glass}}$, where T_{glass} is the glass transition temperature. As depicted in Fig. 1.2, dynamical heterogeneities are spatio-temporal fluctuations in the local dynamical behavior. They have been observed also in living cells [18], and it is expected that we will encounter them even farther afield [19]. Recent research [1, 11, 20–24] has highlighted the importance of dynamical heterogeneities, indicating that they might be helpful in understanding the nature of the glass transition.

D. L. Anderson described the nature of the glass transition as "the deepest and most interesting unsolved problem in solid-state theory" [25]. Indeed, despite the presence of many theoretical frameworks [26–30], a comprehensive and generally accepted theory on the nature of the glass transition and the physics of glasses has not been developed so far. One of the most important, long-standing open questions is the behavior of structural glasses at ultra-low temperatures (1 K and below). The presence of anomalous behaviors of several thermo-

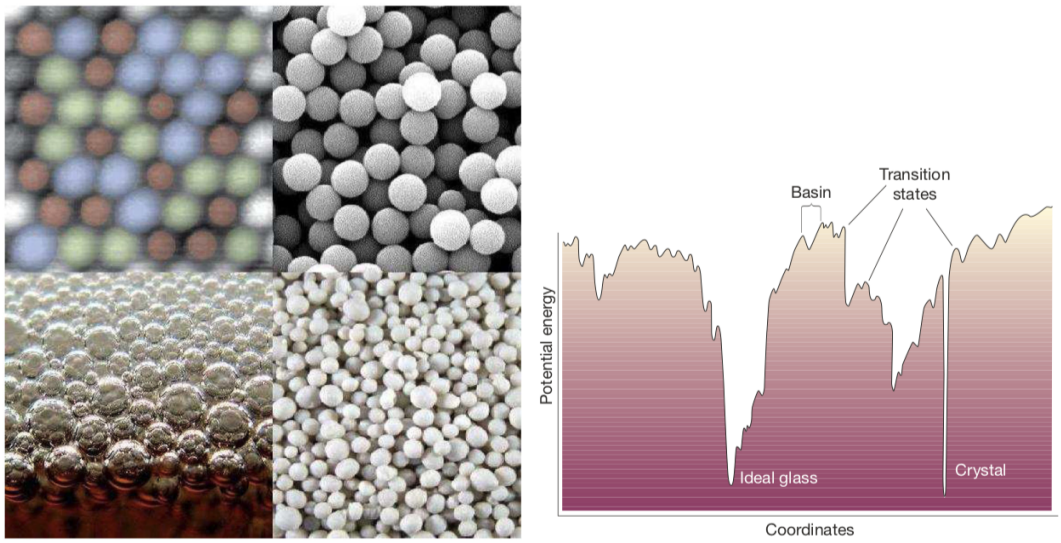

(a) (b)

Figure 1.1.: (a) Glassy phases occur at low temperature or large density in various systems, spanning a broad range of length scales: (top left) atomic force spectroscopy image of an alloy; (top right) colloidal system; (bottom left) beer foam; (bottom right) granular material. Picture extracted from [1]. (b) Schematic illustration of the energy landscape in a glass. The x-axis represents all configurational coordinates. Picture extracted from [2] (adapted from [3]).

dynamic quantities at $T < 1$ K was first noticed by C. Zeller and R. O. Pohl in 1971 [31]. They found that different noncrystalline solids do not follow the behavior predicted by the Debye theory, in contrast to insulating crystals. Such observation was unexpected because long-wavelength acoustic vibrations dominating low-temperature thermal properties were supposed to be insensitive to atomic positional disorder. C. Zeller and R. O. Pohl observed that vitreous silica (SiO_2), selenium (Se), and silica- and germania- based glasses present the same thermal conductivity κ within a factor of 5 in the range $0.05 < T < 100$ K, with the characteristic behavior $\kappa \sim T^\delta$ with $\delta \sim 1.8$ for $T < 1$ K (see Fig. 1.3), in contrast to the Debye cubic behavior. Furthermore, the specific heat was found to vary as $C_V \sim AT + BT^3$ in the temperature range $0.1 < T < 1$ K, instead of the purely cubic dependence observed in crystals. Thus, the specific heat of amorphous silica is several orders of magnitude larger than that of its crystalline counterpart, as illustrated in Fig. 1.4. In Ref. [31], it has been also observed that between 3 and 10 K the thermal conductivity displays a plateau followed by a rise (see Fig. 1.3b), while the specific heat plotted as C/T^3 vs. T displays a bump if plotted in log-log scale (see Fig. 1.4). The latter features are associated with the so-called *boson peak* [32]. In this thesis, however, we will be interested only in the ultra-low temperature properties, i.e. $T < 1$ K. The experimental findings of Ref. [31] in the ultra-low temperature regime do not have a simple explanation, as the authors themselves conclude; they indeed opened up a long and fruitful scientific research line.

The first plausible model able to explain the enigmatic observations of Ref. [31] was published independently by W. A. Phillips [35] and P. W. Anderson, B. I. Halperin, and C. M. Varma [34] in 1972. They introduced the two-level system (TLS) model, which is based on the idea that the physics of glasses at ultra-low temperatures is dominated by *tunneling two-level systems*. The model assumes that, due to their amorphous structure, glassy materials present some entities, such as single atoms, groups of atoms, or even single electrons, that

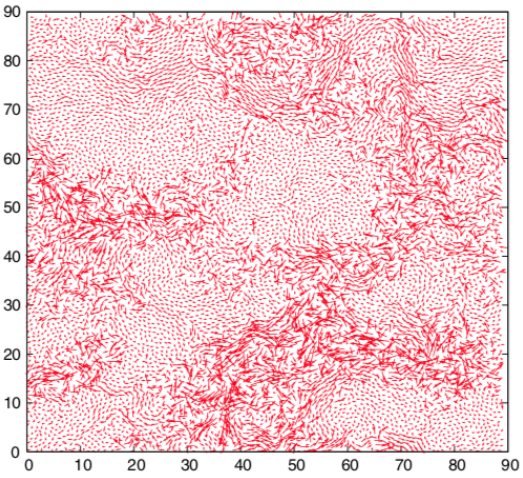

Figure 1.2.: Single particle displacements in the numerical simulation of a diatomic Lennard-Jones liquid in two dimensions. The displacement of each particle over a time window comparable to the structural relaxation time is indicated by the length of the arrow: different particles have different mobilities and form dynamically correlated clusters. Reprinted from [1].

can tunnel between two nearby degenerate configurations, and constitute the only effective degrees of freedom of glasses at ultra-low temperatures. As illustrated in Fig. 1.5, each tunneling entity can be modeled as a double-well potential, where the wells correspond to the two nearby equilibrium configurations. The model is completely specified by the energy difference between the two wells, ε, and the tunneling amplitude, $\Delta \propto \exp(-\sqrt{\frac{2mV}{\hbar^2}}L)$, where m is the mass of the tunneling entity, V is the barrier height, and L is the distance (measured in the generalized coordinate x) between the two equilibrium positions. The TLSs are considered independent, i.e. they do not interact with each other. With a plausible choice of the disorder distributions of the model parameters ε and Δ, one can reproduce quantitatively the values of several equilibrium quantities, including a linear specific heat $C_V \sim T$, and a quadratic thermal conductivity $\kappa \sim T^2$. The original TLS model has undergone considerable elaboration in the last 50 years. An interesting viewpoint has been suggested by the mosaic picture of the random first-order transition theory (RFOT) for structural glasses, when P. Wolynes and collaborators tried to postulate the existence of TLSs as a consequence of processes occurring at the glass transition [36].

Both the strength and the weakness of the TLS model resides in its generality: the microscopic nature of the tunneling entities is not specified, and one can tune the disorder distributions of the model parameters, i.e. $p_\varepsilon(\varepsilon)$ and $p_\Delta(\Delta)$, to reproduce the expected experimental behaviors, such as a linear relation $C_V \sim T$, and a quadratic relation $\kappa \sim T^2$. Despite a large number of experimental [37] and numerical [38, 39] studies aimed at identifying and quantifying the TLS disorder distributions, they have not been fully characterized yet. Their shape and support in the literature are usually inferred from heuristic arguments [33], not without generating some controversies [40, 41].

A series of classical experiments [42–48] have confirmed and expanded the seminal observations of Ref. [31]. New measurements have also brought to light the presence of numerous discrepancies between the experiments and the TLS model [49]. Hence, many authors have tried to extend the model beyond the original works to account for such experimental facts [50–52], while others started to not trust in the TLS model predictive qualities, and criticized

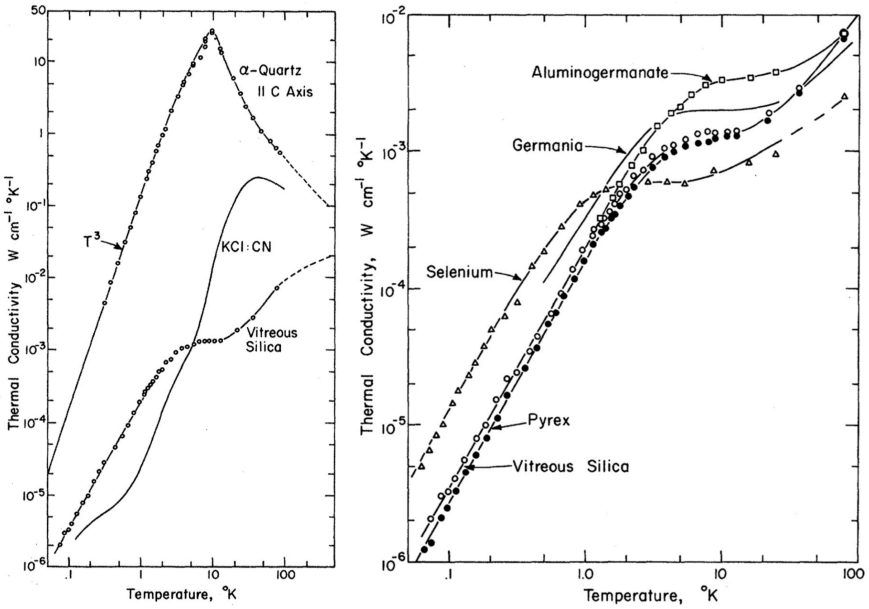

(a) (b)

Figure 1.3.: Thermal conductivity as a function of temperature. (a) Thermal conductivity of crystalline and vitreous SiO_2, and of crystalline KCl:CN. (b) Thermal conductivity of vitreous SiO_2, Pyrex 7740, Se, and of aluminiumgermenate glass at $0.06 < T < 100$ K. Plots extracted from [31].

it as a glorified curve-fitting procedure [36, 53–55]. For example, in Ref. [55], A. J. Leggett and D. C. Vural have extensively examined the problems of the TLS model both at a philosophical and a practical level. One of the central points of their criticisms is whether the TLS model is as unique as it is usually assumed to be. They suggest that this is not the case, and *any* modeling of the system energy levels and stress matrix elements, if properly tuned, would reproduce the experimental behavior of glasses at ultra-low temperatures.

Among the main experimental and theoretical problems of the TLS model, the first is linked to the presence of few direct observations of the tunneling entities. The existence of TLSs in amorphous solids has been established by direct experimental observations only in few systems [56], while in others, such as in amorphous solid toluene [57], evidence for the absence of TLSs has been found. Unfortunately, no definite measurements have been made to test whether the thermal and acoustic properties of the latter systems are analogous to typical glasses. Therefore, clear insights on the TLS microscopic nature are still lacking. While TLSs are generally electrically neutral, in some materials, such as disordered oxide barriers used in Josephson junctions, TLSs have been observed to carry electric dipole moments [58]. Second, as already highlighted, the TLS model predictions depend uniquely on the particular choice of the disorder distributions, which work as fitting parameters. Consequently, the model does not necessarily represent a correct physical description of ultra-low temperature glasses, although it is certainly a good-fitting procedure. Third, most recent experiments have shown that the specific heat and the thermal conductivity vary in temperature as $C_V \sim AT^{\alpha} + BT^3$ with $\alpha \in [1.2, 1.4]$, and $\kappa \sim T^{\delta}$ with $\delta \in [1.8, 1.9]$ [59, 60]. The TLS model instead predicts a purely linear and quadratic behavior, respectively. Fourth, recent experiments have indicated that TLSs are strongly coupled to magnetic fields, which is inexplicable within the TLS model [61, 62]. The lack of direct observations of TLSs at the microscopic length scale has brought some authors to attribute the anomalous magnetic-field dependence of the

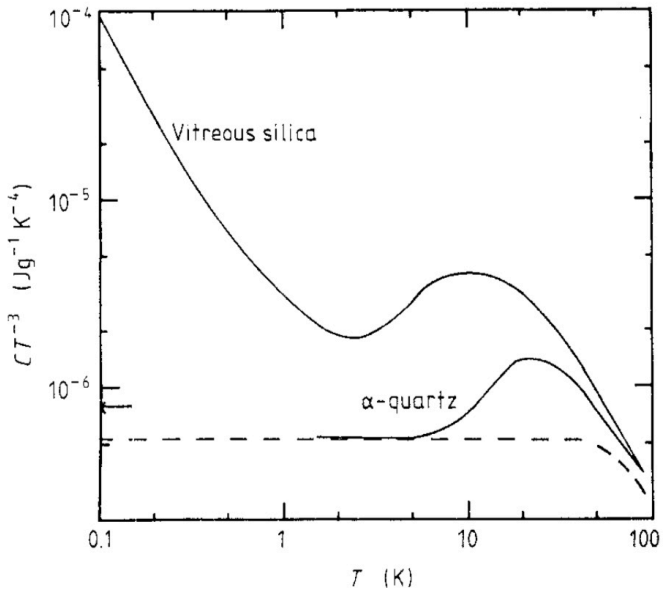

Figure 1.4.: Specific heat as a function of temperature for vitreous silica and crystalline quartz, plotted as C_V/T^3 versus T. Plots extracted from [33].

heat capacity to the presence of multi-minima local potentials, rather than to strictly *two*-level systems as in the original model [63, 64]. Another puzzling question on the validity of the TLS model comes from the surprising quantitative universality of some properties of glasses. In particular, ultrasonic and dielectric measurements have shown that acoustic and dielectric absorptions in glasses are strongly enhanced with respect to crystalline solids and that the dimensionless quality factor Q is notably large, $Q \sim 10^4$, and independent of the chemical composition of the glass in the temperature range $0.1 \lesssim T \lesssim 10$ K. Within the TLS model, Q is given by the product of 4 independent factors; thus, the universality of Q could be only explained via a striking fine-tuning of the model parameters [65, 66]. The final important shortcoming is that the TLS model considers TLSs as independent entities, while consolidated experimental evidence indicates that TLSs interact one with another via the strain field [56, 67–71]. This feature is evident, for instance, from the measurements of the sound velocity, the dielectric constant and the internal friction at $T < 100$ mK [72]. TLS–TLS interactions have been the subject of extensive studies [68, 73–76]. They can be ascribed to the interaction of TLSs with the phonon (or photon) bath.

The interaction between TLSs and phonons was already considered in the original TLS model [34, 35]. However, the generated interactions among TLSs were assumed to be negligible. The TLS-phonon interaction is also responsible for the equilibration of the TLSs at the bath temperature. In the literature, TLSs have always been assumed to be thermal on all experimentally accessible time scales, and standard thermodynamic ensembles have been applied. The issue of how, and on which time scales thermalization takes place has been overlooked so far.

The picture on ultra-low temperature glasses has become even more cluttered when experimental, numerical, and theoretical studies have started to explore *vapor-deposited glasses* [77–82]. These are highly stable glasses prepared by vapor deposition: they are constructed depositing one layer at a time on a substrate. Vapor-deposited glasses can show higher density and kinetic stability with respect to structural glasses. Fig. 1.6a depicts the specific-heat behavior in vapor-deposited glasses of indomethacin, denoted as ultra-stable glasses (USG-1–

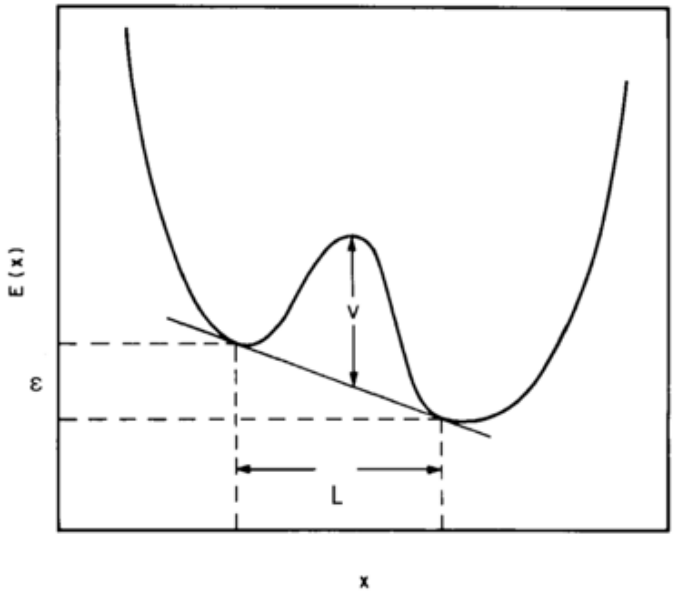

Figure 1.5.: Pictorial representation of a two-level system. The plot shows the energy of the system E as a function of the generalized coordinate x, measuring the position along a line connecting the two nearby local minima of E. The two minima are at distance L; V denotes the energy barrier that separates them, and ϵ denotes their energy difference. Illustration extracted from [34].

USG-2), compared with a crystalline solid, a conventional glass, and a degraded USG, that is a vapor-deposited sample exposed to longer aging in different vacuum conditions[1]. The specific heat of vapor-deposited glasses varies as predicted by the Debye theory: $C_p/T^3 \propto$ const., i.e. the linear term ascribed to TLSs is completely suppressed. At first, this has been considered proof for the depletion of TLSs in all kinds of ultra-stable glasses. However, when a series of experiments on hyperaged (20–110 million-year-old) glasses of geological amber have been performed [83, 84], the idea that vapor-deposited glasses are prototypical examples of ultra-stable glasses has been called into question. Indeed, Refs. [83, 84] show that the features of conventional glasses persist unchanged in hyperaged samples. In particular, it has been found that the specific heat at the lowest temperatures vanishes as $C_V \sim T^{1.27}$, and remains unaltered when considering the pristine hyperaged amber, or the partially and fully rejuvenated amber samples[2]. These results, depicted in Fig. 1.6b, suggest that vapor-deposited glasses do not represent highly stable conventional glasses, maybe because of their layered structure, observed in Ref. [80]. However, no conclusive results are available to solve this issue.

For decades, the striking universality of the ultra-low temperature properties of glasses has been deeply studied both qualitatively and quantitatively; nevertheless, neither a closed theory nor a clear explanation for its origin has been found. In the 1980s and 1990s, many experiments have been focused on crystalline solids with some kind of disorder (different from the translational one of structural glasses). For instance, *orientational glasses* have been

[1] While USG samples were stored in vacuum-sealed bags with desiccant to minimize aging before the specific-heat measurements, the degraded sample was stored in a poor-vacuum bag for two months (see *Materials and Methods* in Ref. [80].

[2] Rejuvenation is a process to erase the thermal history of a glassy sample. In Ref. [84], it is used to transform the hyperaged amber in a less stabilized, conventional glass: the rejuvenation is conducted stepwise, by performing several isothermal treatments to the pristine sample near the glass transition.

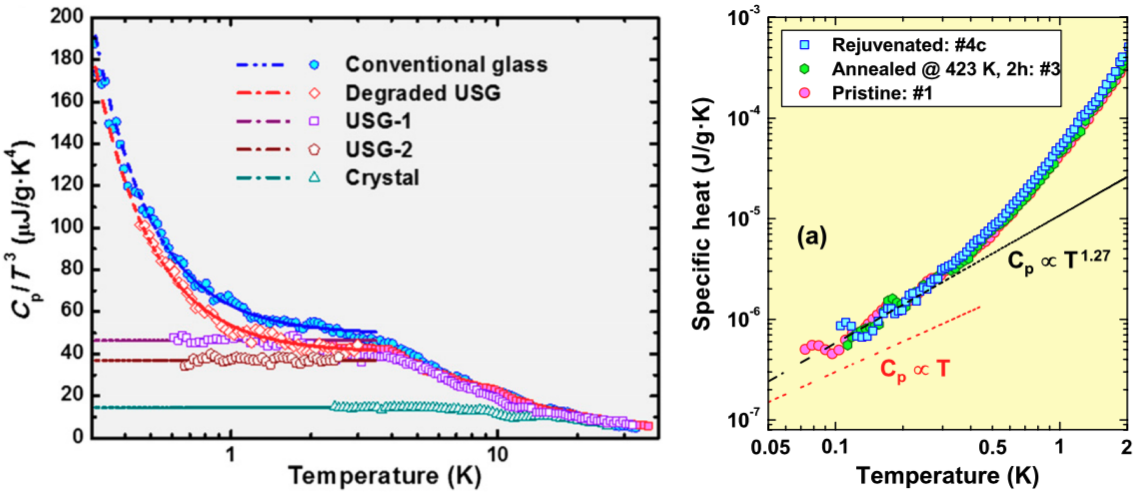

(a) (b)

Figure 1.6.: (a) Specific heat data on ultrastable glasses (USG-1–USG-2) of indomethacin made by vapor deposition. The thin films employed have thickness: 50 μm for USG-1, 80 μm for USG-2. The results are compared with the crystalline phase, the conventional glass, and the degraded USG. Dashed lines follow the fits $C_p = AT + BT^3$. Figure extracted from [80]. (b) Specific heat of hyperaged (100 million-year-old) amber at $0.05 < T < 2$ K. Three different glassy samples are compared: pristine, partially rejuvenated, and fully rejuvenated hyperaged amber. The upper dashed line shows the best quasi-linear fit to the experimental data at $T < 0.4$ K, given by $C_p \propto T^{1.27}$. Figure extracted from [84].

investigated. These are alkali cyanide and other mixed crystals grown with a fixed amount of orientational disorder controlled by the concentration. Orientational glasses exhibit ultra-low temperature specific heat and thermal conductivity with analogous behaviors to amorphous glasses [85]. Over the years, it has been found that a large number of diverse disordered crystals show low-energy lattice vibrations which are quantitatively the same as those measured in amorphous solids [65]. Such observations have suggested that the absence of long-range order is not a sufficient nor a necessary feature for the existence of the low-energy excitations typical of glasses [86]. Consequently, some authors have started to investigate to what extent the anomalous behavior of glasses at ultra-low temperatures is really universal [60]. Reviewing all the available experimental data on the specific heat C_p, it has been realized that the glassy C_p excess, namely the almost linear contribution, is far from being universal among all glassy materials. While in some molecular crystals the linear coefficient is larger than in standard amorphous materials, it assumes a negligible value in few amorphous solids.

To shed new light on the possible origin of the anomalous behavior of glasses at ultra-low temperatures, this thesis explores two main approaches. The first one relies on mean-field models for glasses; we will investigate their thermodynamic properties, both in the classical and the quantum regime. The second one is a finite-dimensional approach, based on the well-known two-level system model for glasses and standard many-body localized systems; we will analyze their quantum dynamics.

A detailed outline of the thesis can be found in the next Chapter.

Summary of the thesis

In this Chapter, we present the outline of the thesis. We introduce the main ideas, physical results, and analytical and numerical techniques discussed in the following Chapters. We list the publications and pre-prints containing the original achievements presented in the thesis.

As discussed in the Introduction, structural glasses at ultra-low temperatures present several puzzling phenomena, such as an anomalous (i.e., non-Debye) behavior of thermodynamic quantities at temperatures lower than 1 K. The goal of this thesis is to explore the effects of quantum mechanics on the properties of glasses at ultra-low temperatures. This aim is pursued by employing two different approaches. On the one hand, we introduce new suitable quantum models for glasses at ultra-low temperatures, and we study their thermodynamic properties. This approach relies mainly on mean-field models for hard spheres and constraint satisfaction problems. On the other hand, we investigate the quantum dynamics of the standard model for ultra-low temperature glasses, namely the two-level system model, showing that it presents the signatures of quantum many-body localization. Moreover, we show that quantum observables in many-body localized systems exhibit a dynamical behavior similar to classical glasses.

Hence, the thesis is divided into two Parts, where my original achievements are reported: Part I focuses on the first approach, and is entitled **Thermodynamics**; Part II is dedicated to the second approach, and entitled **Quantum Dynamics**. The structure of the thesis is as follows.

- Chapter 2 opens Part I of this thesis; it introduces the jamming phase diagram as a unifying picture for different kinds of glassy systems. Specifically, we focus on hard-sphere systems as the minimal model for structural glasses. We describe their jamming transition, which is a mechanical transition that brings the system to form a mechanically rigid packing. Importantly, the jamming critical point seems to be independent both of the preparation protocol and the dimension of the system. We sketch the dynamical phase diagram of mean-field hard spheres and discuss their connection with constraint satisfaction problems.

- Chapter 3 is devoted to the exploration of the jamming transition in hard spheres, and to testing its independence of the system dimensionality. We present a novel iterative linear programming algorithm for studying jamming in hard spheres in arbitrary dimensions, highlighting its strengths and applicability range. By means of that algorithm, we are able to explore the structure of the jamming landscape as a function of the packing fraction in three-dimensional hard spheres. We find that the jamming landscape is rough and hierarchically organized. Remarkably, this topology corresponds to the one analytically predicted for infinite-dimensional hard spheres, thus supporting the universality of the jamming transition.

- Chapter 4 is devoted to the investigation of the quantum jamming transition in the

quantum mechanical perceptron model. First, the classical version of the model is presented, and its relation with hard-sphere systems is underlined. Then, we generalize the perceptron to the quantum realm. Employing this model, we are able to explore for the first time the jamming transition of mean-field quantum hard spheres deep in the quantum regime. We expect these results to have implications both for the theory of glasses at ultra-low temperatures and for the study of quantum machine-learning algorithms. In the perceptron model, we observe that quantum effects affect sensibly the transition, changing the critical exponents with respect to the classical ones. Moreover, we find that the quantum critical point is not confined to the zero-temperature axis, and the classical results are recovered only at $T = \infty$. This suggests that quantum effects have a crucial role also in the case of low-temperature structural glasses.

– Chapter 5 opens the second Part of this thesis, which is dedicated to the quantum dynamics of glasses at ultra-low temperatures. In this Chapter, we outline the main features of many-body localization, which is a non-ergodic state of matter existing only in the quantum realm. As glasses, however, many-body localized systems fail to thermalize even at infinite times. We discuss the common aspects and the differences between many-body localized and glassy systems.

– Chapter 6 contains the investigation of the quantum dynamics of an ensemble of two-level systems (TLSs) coupled with a phonon bath in the weak-coupling limit. In the literature, TLSs have always been considered thermal on all experimentally accessible time scales, and standard thermodynamic ensembles have been applied. However, the presence of the strong, long-tailed disorder characterizing the distributions of the model parameters, suggests that quantum effects might be consistent. By integrating out the phonons within the framework of the Gorini-Kossakowski-Sudarshan-Lindblad (GKSL) master equation, we find that the dynamics of the system at short and intermediate time scales presents clear signatures of many-body localization physics (in particular, a power-law decay of the concurrence), even in the presence of dissipation, if the latter is not too large. Remarkably, we show that such signatures of localization should be experimentally accessible in real glassy samples at ultra-low temperatures, using for instance ultra-fast laser probes. Hence, our findings show that glasses might be a privileged platform for probing many-body localization in real materials.

– Due to the uncertainty in the characterization of the disorder parameters entering the two-level system model, in Chapter 7 we re-analyze the quantum dynamics of TLSs coupled with phonons within the strong-coupling approximation. In this regime, by applying a simple unitary transformation to the full Hamiltonian of the system, we find that the bare tunneling amplitudes of the TLSs become exponentially suppressed by the polaron effect. Interestingly, the polaron effect can thus justify the small values and the wide distributions usually attributed in the literature to the tunneling amplitudes. By means of a perturbation theory in the tunneling amplitudes, we are able to compute analytically the dissipation rates of the TLSs: their typical value results the smallest energy scale of the problem. Finally, we derive a new phenomenological master equation for the TLSs in the GKSL form, showing the presence of a localized transient regime for the TLS dynamics, in agreement with the result within the weak-coupling approximation.

– In Chapter 8, we address an original aspect of many-body localized systems, namely the spatio-temporal behavior of quantum entanglement. We investigate the relaxation times of the onsite concurrence, as a measure of the time scale of local entanglement.

As disorder increases or energy decreases, the distribution of the relaxation times becomes wider, and longer-range spatial correlations are observed. The spatial correlation of the onsite entanglement allows us to introduce a new dynamical correlation length for many-body localized systems. The spatio-temporal behavior of entanglement exhibits a striking resemblance with dynamical heterogeneities in classical glasses. Since entanglement is a genuine quantum object, which is with no classical analog, the observed similarity to the classical case is even more remarkable.

– Chapter 9 contains the concluding remarks of the thesis. We summarize the original achievements reported, and we highlight the possible future research directions that the present studies have opened.

List of publications

The original achievements reported in Chapters 3–8 are based on the following publications and pre-prints:

1) Artiaco, C., Baldan, P., & Parisi, G. (2020). "Exploratory study of the glassy landscape near jamming", Phys. Rev. E, 101 (5), discussed in Chapter 3.

2) Artiaco, C., Rojas, R. D. H., Parisi, G., & Ricci-Tersenghi, F., (2021). "An iterative Linear Programming algorithm for jamming hard spheres", in preparation, discussed in Chapter 3.

3) Artiaco, C., Balducci, F., Parisi, G., & Scardicchio, A. (2021). "Quantum jamming: Critical properties of a quantum mechanical perceptron", Phys. Rev. A 103 (4), L040203, discussed in Chapter 4.

4) Artiaco, C., Balducci, F., & Scardicchio, A. (2021). "Signatures of many-body localization in the dynamics of two-level systems in glasses", Phys. Rev. B 103 (21), 214205, discussed in Chapter 6.

5) Artiaco, C., Balducci, F., Fabrizio, M., & Scardicchio, A. (2021). "Signatures of many-body localization in the dynamics of two-level systems in glasses in the strong-coupling limit", in preparation, discussed in Chapter 7.

6) Artiaco, C., Balducci, F., Heyl, M., Russomanno, A., & Scardicchio, A. (2021). "Spatio-temporal heterogeneities of entanglement in the many-body localized phase", arXiv:2108.05594, discussed in Chapter 8.

Not discussed in the thesis, there is an oncoming work on the dynamics of the wetting layer in the presence of phase coexistence in an open quantum system:

7) Artiaco, C., Nava, A., & Fabrizio, M. (2021). "Lindblad dissipative dynamics of the wetting layer in the presence of phase coexistence", in preparation.

Part I.

Thermodynamics

2. Introduction to Part I

In this Chapter, we present the jamming phase diagram which provides a framework for unifying the physics of different kinds of glasses. The jamming transition in hard-sphere systems is then described. We sketch the dynamical phase diagram of mean-field hard spheres and highlight their link with finite-dimensional systems. Finally, we discuss the connection between hard spheres and continuous constraint satisfaction problems.

As discussed in Chapter 1, glasses are ubiquitous: diverse and various systems fall into the category of glasses, such as structural glasses, granular materials, emulsions, foams, and colloidal suspensions. The important ingredient that pools these systems together is the presence of an amorphous structure and of the dynamical arrest. Indeed, in glassy systems, the typical relaxation time is much larger than the typical duration of experiments or numerical simulations. Therefore, their dynamics ceases, and they remain *static* for all the observation time. It is clear, however, that all these systems present completely different microscopic natures and, historically, different control parameters. So, a question of paramount interest would be whether such glassy phases and transitions share general features in common, both at a qualitative and quantitative level. In other words, one can ask, for instance, whether the dynamical arrest of colloidal suspensions as pressure or packing fraction are raised is profitably comparable with the freezing of a liquid into a structural glass. In Ref. [87], it has been proposed the first unifying framework of glassy systems, namely the *jamming phase diagram*, illustrated in Fig. 2.1. In such a diagram, the phase boundary marks the point where the system becomes so sluggish that it appears stuck for any experimental time scale. The so-called jamming phase is enclosed in the boundaries. It might be entered as different parameters are varied: temperature, density, or load. Hence, the jamming phase diagram opens interesting scenarios. First, the diagram implies that the three control parameters are important for all systems, or conversely that each system is controlled by all the three variables. It suggests, for example, that the glass transition temperature of structural glasses should diminish if the density of the system increases or the shear stress applied to it decreases. Second, it put in contact the thermal glass transition with the athermal jamming transition. Specifically, it suggests that one can have insights into the physics of structural glasses and their low-temperature properties, exploring simpler systems, such as hard spheres, mainly controlled by density. Finally, the diagram indicates that the jamming region might control the behavior nearby, thus suggesting an explanation for the similarities observed in different kinds of systems as the glass transition is approached.

The jamming phase diagram has been successfully exploited in experiments on solidification of attractive colloidal suspensions [88]. Nevertheless, its extent of validity is still under debate among the glass physics community. Several hints have been found suggesting that the physics of structural glasses, in particular their free-energy landscape, share many features in common with other systems. In particular, in Ref. [17] it has been argued that structural glasses might present a fractal structure of the free-energy landscape similarly to hard spheres. However, more recent studies [89–91] have pointed out that the situation might be

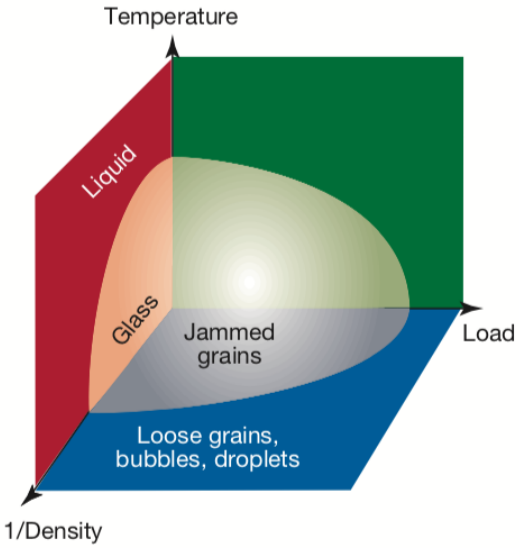

Figure 2.1.: Jamming phase diagram proposed in Ref. [87]. The jamming phase is enclosed in the shaded region around the origin. The picture proposes a unifying interpretation for the glassy phase in structural glasses, colloids, and granular materials. The extent of validity of the jamming phase diagram is still an open question. Picture adapted from [87].

more complicated [92]. Performing comprehensive numerical studies of three-dimensional molecular glasses, it has been observed that behaviors analogous to hard spheres near jamming, e.g. rejuvenation and memory effects expected in the Gardner phase [93–96] (see also Chapter 3), are present only in some regions of the parameter space. In other cases, a hard-sphere phenomenology has been reported [97–99]. In addition, renormalization group studies have yielded controversial results [100–102].

Hard-sphere systems are formed by (typically spherical) particles that cannot overlap: spheres interact via a hard-wall potential which is infinite if two of them overlap, and it is zero otherwise. The jamming transition of hard spheres can be easily visualized; its pictorial representation is shown in Fig. 2.2. We see that the jamming critical point is encountered at increasing the system density. When the density is low (left panel), there are many configurations in which particles do not overlap. At increasing density, however, the free volume left by the particles diminishes, and at a certain density value the particles cannot move further without overlapping one with another: this is the jamming transition point (central panel). Hard spheres at jamming become stuck under the exertion of external stress due to the creation of a force network, depicted in Fig. 2.3 for a two-dimensional system. The picture shows the presence of some particles (in orange) which are not part of the force network. They are known as rattlers; they disappear as the dimension of the system increases and are completely absent in the mean-field case. If the density increases further (right panel of Fig. 2.2), there would be overlapping particles. This situation is not allowed for hard spheres. However, this regime might be reached by defining a soft potential and transforming hard spheres into an optimization problem.

The jamming transition of infinite-dimensional hard spheres has been analytically solved. The exact theory for the critical behavior of mean-field hard spheres at jamming, along with the scaling laws among different critical exponents, is reviewed in Ref. [95]. Mean-field models have always been fundamental platforms to study the intricate physics of glassy sys-

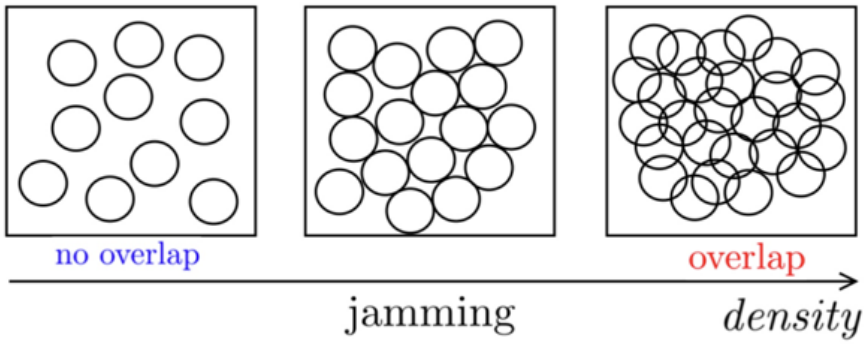

Figure 2.2.: Pictorial representation of the jamming transition in sphere systems. When the density is low, the particles can freely move without overlapping with each other. At increasing the system density, the free space available diminishes. At the jamming threshold, the system becomes completely stuck: the particles cannot move further, otherwise, they would overlap. If the density increases further, there are overlaps among particles. This situation is not allowed in hard-sphere systems.

tems [15]. In recent years, infinite-dimensional hard-sphere systems have gained plenty of attention among the glass physics community [16]. Their dynamics and thermodynamics have been investigated around the dynamical, Gardner, and jamming transitions. The phase diagram of infinite-dimensional hard spheres presents three dynamical phases, which are illustrated in Fig. 2.4.

The control parameters of hard-sphere systems are the pressure and the packing fraction[1], ϕ. Different regions of the phase diagram can be identified by the behavior of the mean-square displacement (MSD), defined as $\Delta(t) := \frac{1}{L}\sum_{i=1}^{L} |\mathbf{r}_i(0) - \mathbf{r}_i(t)|^2$, where L is the system size, and $\mathbf{r}_i(t)$ is the position of the particle i at time t. When the pressure is small, the system is ergodic, and $\lim_{t\to\infty} \Delta(t) = \infty$ (Fig. 2.4, left column). An equilibrium compression of the liquid can be carried out only up to ϕ_d, the dynamical transition point. At ϕ_d, the phase space becomes clustered into exponentially many glassy states. These clusters are mutually inaccessible and trap the dynamics at infinite times: $\lim_{t\to\infty} \Delta(t) = \Delta_1 < \infty$. For $\phi_g > \phi_d$, it is possible to define a restricted equilibrium state [104]. This is known as the stable glass phase: the system can completely relax inside the metastable state but long-time diffusion is forbidden. The particles of a stable glass are caged by their neighbors and vibrate around their "amorphous equilibrium positions" in *cages* whose typical size is Δ_1 (Fig. 2.4, central column). Compressing further the stable glass up to $\phi_G(\phi_g)$, one encounters the Gardner transition, where even the restricted equilibrium is lost: the stable glass state breaks into a hierarchical structure of marginal states (landscape marginal stability) (Fig. 2.4, right column). This implies the existence of delocalized soft modes, diverging susceptibilities [105], and anomalous rheological properties [106]. Beyond the Gardner transition, the number of minima of each cage is expected to diverge exponentially in the number of components of the system [107]. Finally, compressing the system up to the point where the pressure diverges, the system jams. At jamming, the packings are mechanically rigid and isostatic, meaning that the number of mechanical constraints is equal to the number of degrees of freedom [108]. Isostaticity implies that the system is mechanically marginally stable. Hence, at the jamming

[1]The packing fraction ϕ is defined as the fraction of the volume occupied by the particles. In a monodisperse system, $\phi = \frac{4}{3}\pi r^3 \rho$, where $\rho = \frac{N}{V}$ is the density and r is the radius of the spheres.

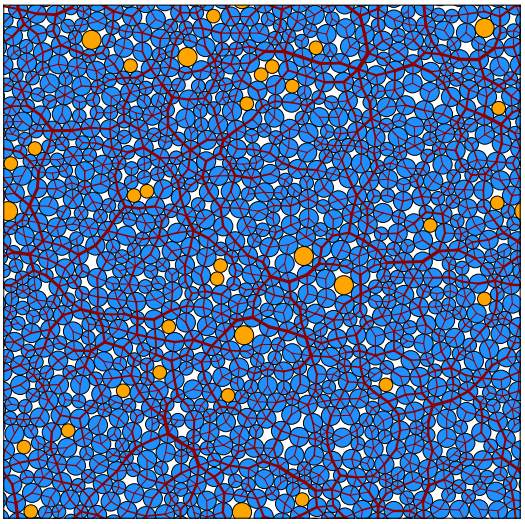

Figure 2.3.: Jammed packing of bidisperse hard spheres in two dimensions. The full network of contacts is shown in red; the thickness of the lines is proportional to the force magnitude. Orange particles are not part of the force network; they are called *rattlers*. They disappear as the dimension of the system increases. Figure extracted from [103].

point, the number of soft modes is enhanced.

It has been found that the mean-field theory provides reliable predictions for many properties of finite-dimensional systems. Remarkably, recent numerical simulations have pointed out that the critical properties of the jamming transition might be *universal*, i.e. independent both of the preparation protocol and of the dimension[2] of the system for $d \geq 2$. The results discussed in Chapter 3 follow exactly this research line, trying to assess whether the jamming landscape of three-dimensional hard spheres shows the same properties of infinite-dimensional ones. The universality of jamming of hard spheres is a very promising quality: it implies that one can use the exact results on the mean-field model to predict the properties of finite-dimensional systems. In addition, considering the unifying picture given by the jamming phase diagram, the mean-field model of hard spheres should be also connected to structural glasses. Therefore, one can try to shed light on the physics of structural glasses employing infinite-dimensional sphere systems.

This picture still misses another important ingredient, which is revealed by the diagram sketched in Fig. 2.2: the jamming transition of hard spheres can be thought of as the satisfiability/unsatisfiability threshold of continuous *constraint satisfaction problems* (CSPs). The constraints are induced by the requirement that spheres cannot overlap. In the framework of CSPs, it has been found in Ref. [110] that the perceptron, introduced in 1958 in neural networks [111], is the simplest model in which jamming is in the same universality class of hard spheres in infinite dimensions. The perceptron model is a privileged point of view: thanks to its analytical tractability, it gives the possibility to explore special instances of the sphere problem [112], and even to analyze their quantum regime [113]. We will exploit the perceptron model in Chapter 4 to investigate the quantum jamming transition.

[2] However, when considering finite-dimensional systems, some minor effects come into play due, for instance, to *rattlers* and *bucklers* [109].

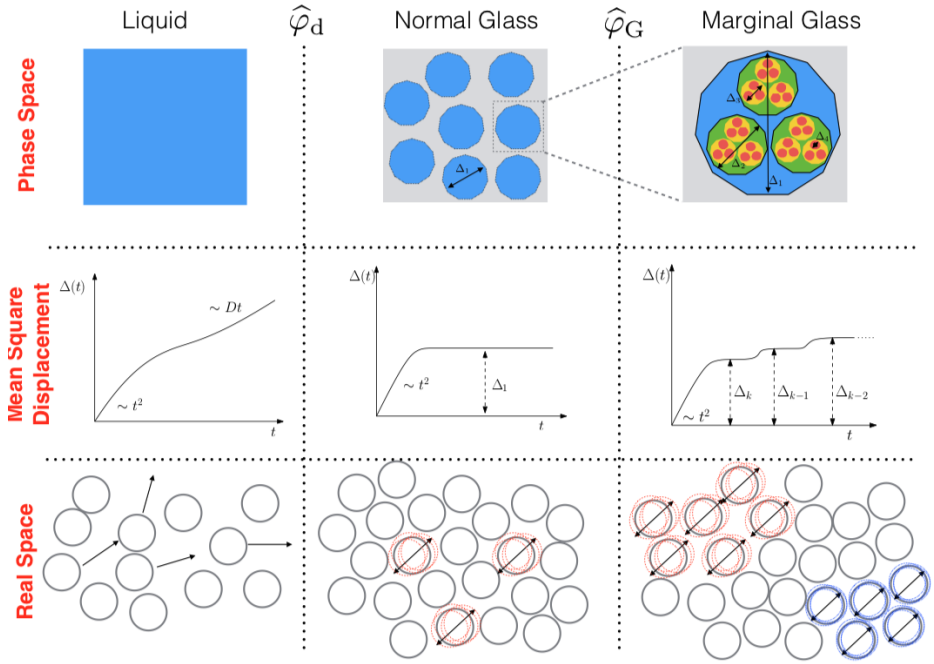

Figure 2.4.: The three dynamical phases of hard spheres. The left column shows the features of hard spheres in the liquid phase. The particles are free to move and the mean-square displacement (MSD) presents a ballistic regime at short times, followed by a diffusive regime. The central column depicts the normal glass, where the phase space is divided into disconnected basins. The MSD shows a plateau due to the presence of cages. In the right column, we observe the phenomenology of the marginally stable glass. Each cluster of configurations belongs to a basin which is subdivided into smaller sub-basins, hierarchically organized. Since the system presents the full replica symmetry breaking, the MSD presents infinitely many steps. Reprinted from [95].

3. Jamming landscape in three-dimensional hard spheres

This Chapter is devoted to the investigation of the properties of the jamming landscape of three-dimensional hard spheres as a function of the packing fraction. We show that, by employing a novel iterative linear programming algorithm, presented in Section 3.1, we are able to explore the landscape structure. In Section 3.2, we present an exploratory study on such landscape structure, starting from independent configurations in the same cage. We show that the landscape is rough and complex, and presents a large number of different minima which seem to be organized hierarchically. That points towards the universality of the jamming transition of hard spheres. The reference articles are Refs. [114, 115].

Validating the mean-field picture of hard spheres in finite-dimensional systems would greatly increase the global understanding of the glass transition, as already emphasized in Chapter 2. In particular, the presence of the Gardner transition in finite-dimensional glasses is still a matter of debate, due to the presence of controversial numerical and renormalization-group results. In this Chapter, we present a direct inspection of the presence of the Gardner phase in three-dimensional hard spheres at jamming, looking at the properties of the landscape local minima. This exploration is performed thanks to an innovative linear programming algorithm, able to access the jamming transition directly from the hard-sphere regime, i.e. without introducing any fictitious potential among particles, as standard algorithms do. We study the distribution of the packing fraction of the local minima, and their relative distance in the configuration space. We observe the presence of a large number of minima. The deepest minima are close both in terms of packing fraction and distance, and present large basins of attraction. Our analysis shows that the system undergoes a roughness transition, which brings about isostaticity on approaching jamming. Moreover, the signatures of an ultrametric structure of the landscape are found. These results agree with the exact solution of infinite-dimensional hard spheres.

3.1. An iterative linear programming algorithm for jamming in hard spheres

Linear programming algorithms are methods to solve linear optimization problems [116, 117]. As sphere systems can be formulated as constraint satisfaction problems (see Chapter 2), also jamming in hard spheres can be seen as an optimization problem: the objective is to maximize the particles' radii (equivalently, inflate the particles) without overlaps among particles. Notice that, in order to leave unchanged the degree of polydispersity of the systems, the inflation rate has to be equal for all the spheres. Similar algorithms have been implemented in Refs. [118, 119]. The variables of the optimization problem are the inflation rate α, and the particles' displacements $\mathbf{\Delta}$. Since we fix the position of a sphere to avoid

the rigid translation of the system as a whole, the latter are $3(L-1)$ scalar variables. The constraints of the problem are

$$(\boldsymbol{x}_i - \boldsymbol{x}_j)^2 + 2(\boldsymbol{x}_i - \boldsymbol{x}_j)(\boldsymbol{\Delta}_i - \boldsymbol{\Delta}_j) + (\boldsymbol{\Delta}_i - \boldsymbol{\Delta}_j)^2 - \alpha\sigma_{ij}^2 \geq 0 \tag{3.1}$$

where $\boldsymbol{x}_i$ indicates the position of the sphere i, $\sigma_{ij} = \frac{\sigma_i + \sigma_j}{2}$ is the sum of the radii, $\mid \Delta_i^{x,y,z} \mid \leq c$ and $0 \leq \alpha \leq c'$ for c and c' reasonable numbers with respect to the linear dimensions of the system. To employ linear programming algorithms we need to linearize the problem in Eq. (3.1): supposing that the particles' displacements are small, we can neglect the terms $(\boldsymbol{\Delta}_i - \boldsymbol{\Delta}_j)^2$. This assumption is asymptotically justified since, after few iterations of the linear programming algorithm, the increase of the particles' radii will reduce the magnitude of the possible displacements. Moreover, in Ref. [115] we analytically show that a solution of the linearized problem is also a solution of the *exact* optimization problem.

The final linear problem is a maximization problem with objective function α:

$$\begin{cases} (\boldsymbol{x}_i - \boldsymbol{x}_j)^2 + 2(\boldsymbol{x}_i - \boldsymbol{x}_j)(\boldsymbol{\Delta}_i - \boldsymbol{\Delta}_j) - \alpha\sigma_{ij}^2 \geq 0 \\ \max \alpha \end{cases} \tag{3.2}$$

For each couple of particles, the constraints in Eq. (3.2) are satisfied and the inflation α is maximized, when the spheres go as far as possible along the direction orthogonal to the constraint and are inflated until the constraint is saturated. Since each sphere has many neighbors and all the constraints have to be satisfied simultaneously, the displacements would not be only along this orthogonal direction and the physical constraints will not be saturated after only one iteration. This is why some iterations ($\sim O(10)$) are needed to reach the jamming point. Thus, the iterative solution of the linear problem in Eq. (3.2) defines the iterative linear programming (iLP) algorithm for jamming in hard spheres.

The main strength of the iLP algorithm is that it is able to reach the jamming point of hard spheres without introducing any fictitious potential, as standard algorithms do. The large employment in the literature of fictitious potentials is mainly due to the existence of numerous, powerful energy minimization techniques, such as FIRE [120]. However, their usage has two main drawbacks. First, the spurious interactions might affect the physical properties of the system close to the jamming point. Second, these algorithms identify the jammed packings as equilibrium states at zero temperature, while in hard spheres they should correspond to entropy minima. Both problems are overcome by the iLP algorithm. Therefore, an efficient iLP algorithm can be used not only to explore confidently the jamming transition of hard spheres but also to check that the results already obtained within the soft-sphere approach are fully consistent with the ones for hard spheres, as recently done in Ref. [121].

Importantly, it can be shown analytically that the configurations obtained with iLP are well-defined jammed states. Indeed: (i) iLP solutions satisfy the mechanical equilibrium conditions; (ii) they are isostatic (or at least they are never hypostatic); (iii) they reproduce the force balance equations that determine the force magnitudes in soft spheres; (iv) point (iii) implies that the Hessian obtained for hard spheres matches that of soft spheres, which has been found to reproduce the marginal stability condition expected from the mean-field solution.

The iLP algorithm has been employed in Ref. [114, 121, 122]. An extensive discussion on it and on its improved versions can be found in Ref. [115]. In particular, we show that it can be combined with another compression protocol, namely the Lubachevsky-Stillinger protocol, to perform efficiently detailed explorations of the jamming landscape.

3.2. An exploratory study of the glassy landscape near jamming

In this Section, we present the results obtained for the structure of the jamming landscape in three-dimensional hard spheres by means of the iLP algorithm of Section 3.1. We start from equilibrated independent configurations in the same cage (see Chapter 2) and we bring them to the jamming point via the iLP algorithm to look at the landscape local minima.

Since the number of minima of each cage is expected to be exponentially large in the system size, we restrict our study to 100, three-dimensional hard spheres. In order to enhance the equilibration process, the spheres diameters are drawn from the continuous probability distribution $P(\sigma) \propto \sigma^{-3}$, with $\sigma_{min}/\sigma_{max} = 0.45$ (see Ref. [123]). The equilibration has been achieved via the constant-pressure swap Monte Carlo algorithm[1] [124] to produce four glassy configurations in different cages at $\phi_g = 0.647$ ($\phi_d = 0.594$), whose position in the phase diagram of Fig. 3.1 is represented by the green square. Notice that in finite dimensions, since the energy barriers between metastable states are finite, the dynamical transition ϕ_d of the mean-field scenario (see Chapter 2) reduces to a crossover. For this reason, it is possible to numerically generate equilibrated glassy configurations even at $\phi_g > \phi_d$ via improved Monte Carlo algorithms, such as the swap Monte Carlo. Nevertheless, in conventional dynamics, the time spent by the system in a metastable state can be considered, to a good extent, infinite.

The absence of spatial order and long-time diffusion are key features of glasses. Hence, we first study the spatial structure of the initial glassy configurations, computing the radial distribution function [125], and we investigate their dynamical properties, measuring the mean-square displacement (MSD) as a function of time. Our analysis does not show any sign of crystalline order, phase separation, and long-time diffusion.

3.2.1. Sample generation and compression protocol

By means of an NVT Monte Carlo dynamics[2], we evolve in time each of the starting configurations. At $t = \tau_{\text{cage}}$, the system enters the caging regime, signaled by a plateau in the MSD (Fig. 2.4, central column). Saving the time-evolved configurations every $3\,\tau_{cage}$ sweeps, we create a set of independent configurations belonging to the same cage, called *clones*. The set of clones generated from the same initial configuration is called a *sample*. To prevent long-time diffusion and the breaking of the cage, we periodically restart the dynamics from the initial configuration. Indeed, due to the stochasticity of the Monte Carlo dynamics, we are guaranteed to sample different trajectories at each restart. We end up with a set of 2×10^5 independent glassy configurations in the same cage. Furthermore, via a fast compression[3] of the initial configuration, we generate a new glassy configuration at a higher packing fraction, $\phi = 0.68$. The fast compression does not distort the jamming landscape, but pushes the system into one of the subcages, if, at that packing fraction value, the cage is already broken

[1] The equilibration beyond the dynamical transition point via the Swap Monte Carlo algorithm has been carried out by L. Berthier and the Montpellier research group, that we warmly thank.

[2] In a sweep of the NVT Monte Carlo dynamics, we propose the displacement of each particle of the system. If the displaced particle overlaps another particle, the movement is refused. We measure the time in units of Monte Carlo sweeps.

[3] We move the particles via the NVT Monte Carlo dynamics and, after a fixed number of steps, we increase all the diameters of a factor $\gamma = 10^{-3}$. If in the new packing some spheres do overlap, we refuse the inflation and we further move the particles. The procedure stops when the packing fraction of the configuration reaches $\phi = 0.68$. We call this as *fast* compression because it carries the system out-of-equilibrium.

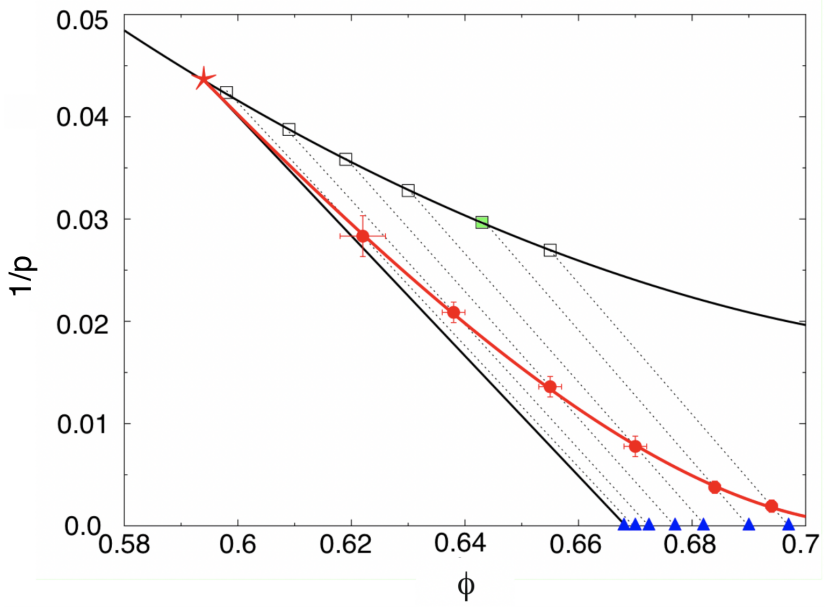

Figure 3.1.: Phase diagram of polydisperse hard spheres in three dimensions. The initial glassy configurations are equilibrated in correspondence of the green square. The green and the white squares lie on the equation of state of the liquid at various φ_g; the red line represents the Gardner transition line, $\varphi_G(\varphi_g)$, and the line with blue triangles represents the jamming line, $\varphi_J(\varphi_g)$ (see Chapter 2 for more details). Extracted from [114], adapted from [97].

into subcages[4]. From the new configuration, we produce another set of 2×10^5 packings in the same subcage. Thus, we follow two compression protocols: (i) taking each sample at $\phi = 0.647$, we bring each clone to the jamming point, via the instantaneous iterative linear programming (iLP) compression (see Section 3.1); (ii) we repeat the same procedure for each sample at $\phi = 0.68$.

In the hard-sphere regime, i.e. in the uncompressed region, the probability of having a hard-sphere packing at ϕ is proportional to $e^{-Lp/\phi}$, where p is a proxy for the pressure, and L is the system size. Hence, the jamming transition is reached at $p = \infty$ and the jammed packings maximize ϕ.

3.2.2. Numerical results

We now present the results obtained for the landscape local minima at jamming. Notice that larger values of the jamming packing fraction ϕ_J correspond to minima which are *deeper* in the landscape, while smaller values of ϕ_J coincide with minima *higher* in the landscape. Importantly, we verified that most of the jammed packings obtained using the iLP algorithm are isostatic, i.e. they verify $L_c = L_c^{\text{iso}} := (L-1)d + 1$[5], consistently with the mean-field solution. Several works [109, 126–129] have highlighted the importance of having $L_c =$

[4] We verified this important feature a posteriori, checking that the jamming packings reached from configurations at $\phi = 0.68$ are a subset of the ones reached from $\phi = 0.647$.

[5] $L_c = (L-1)d + 1$ is the isostaticity condition for a finite system under periodic boundary conditions (PBC) [109]. Here, L_c is the number of contacts of the jammed packing, L is the number of particles (excluding the rattlers, i.e. particles that are not part of the force network, and d is the dimension of the system.

L_c^{iso} to observe key aspects of jamming criticality. Therefore, we restrict our analysis to the packings with $L_c = L_c^{\text{iso}}$.

Local Minima

Compressing the clones of a sample up to jamming, we find many jammed packings with the same ϕ_J. This is especially true for high values of ϕ_J. Furthermore, the packings with the same ϕ_J present also the same arrangement of the particles but for a rigid translation [6], i.e. they represent the same local minimum at jamming. In each different cage, we find that the jamming local minima coming from $\phi = 0.68$ are a subset of those coming from $\phi = 0.647$, meaning that at $\phi = 0.68$ the starting cage is already broken into subcages. This result can be considered an indirect proof of the goodness of the iLP algorithm, since it shows that, starting from different heights of the same basin, the landscape local minima are not altered.

For each sample, we compute the local minima distribution at jamming, shown in Fig. 3.2. They have different supports, depending on the depth of the basin of that cage. The ϕ_J's distributions are not self-averaging quantities. The average ϕ_J values, merging the data from different cages, are $\overline{\phi}_{J,\,0.647} = 0.6955$ and $\overline{\phi}_{J,\,0.68} = 0.6957$. Two important features of the landscape are summarized by Fig. 3.2: many deep local minima are found with high probability and are characterized by similar ϕ_J values. We argue that the first feature means that their basins of attraction are large. We find that the ϕ_J distributions may be wider or narrower. The average differences between the highest and the lowest jamming packing fractions are $\overline{\Delta\phi}_{J,\,0.647}^{\text{max-min}} = 0.0035$ and $\overline{\Delta\phi}_{J,\,0.68}^{\text{max-min}} = 0.0016$. The average ratios between the number of distinct local minima found and the total number of clones in the same sample are, respectively, $f_{0.647} = 0.32$ and $f_{0.68} = 0.20$.

Ordering in a progressive way the jamming packing fractions, we can define

$$\delta_n = \phi_{n+1} - \phi_n \geq 0 \tag{3.3}$$

$$0 \leq r_n = \frac{\min\{\delta_n, \delta_{n-1}\}}{\max\{\delta_n, \delta_{n-1}\}} \leq 1 \tag{3.4}$$

If the ϕ_J's are uniformly distributed, one expects the level statistics to be Poissonian [130] and, thus, $P_{\text{Poisson}}(r) = 2/(1+r)^2$ with $\langle r \rangle_{\text{Poisson}} \simeq 0.386$. Computing $\langle r \rangle$ in each sample, the Poissonian statistics turns out to be almost valid. Indeed, the average on all the samples is $\langle r \rangle_{0.647} = 0.384 \pm 0.001$ and $\langle r \rangle_{0.68} = 0.382 \pm 0.002$.

Local minima in the Configuration Space

Since at jamming, in each sample, we find a huge number of distinct local minima ($\simeq 10^4 - 10^5$), here we study in detail the arrangement in the landscape only of a subset of them, the 1000 deepest minima. First of all, we want to understand how the deepest minimum (i.e. the one with the highest ϕ_J) of each sample is located in the configuration space. To do so, we compute its square distance

$$\Delta := \Delta^2_{\alpha\beta} = \frac{1}{M}\sum_{i=1}^{M}(\boldsymbol{x}_i^{\alpha} - \boldsymbol{x}_i^{\beta} - \boldsymbol{\delta})^2 \tag{3.5}$$

[6] The rigid translation is due to the translational invariance of the system. This effect has been taken into account in all the results shown in the present study. In particular, in computing the distance Δ (Eq. (3.5)) and the overlap Q (Eq. (3.6)), we subtracted the displacement of the center of mass among the two configurations.

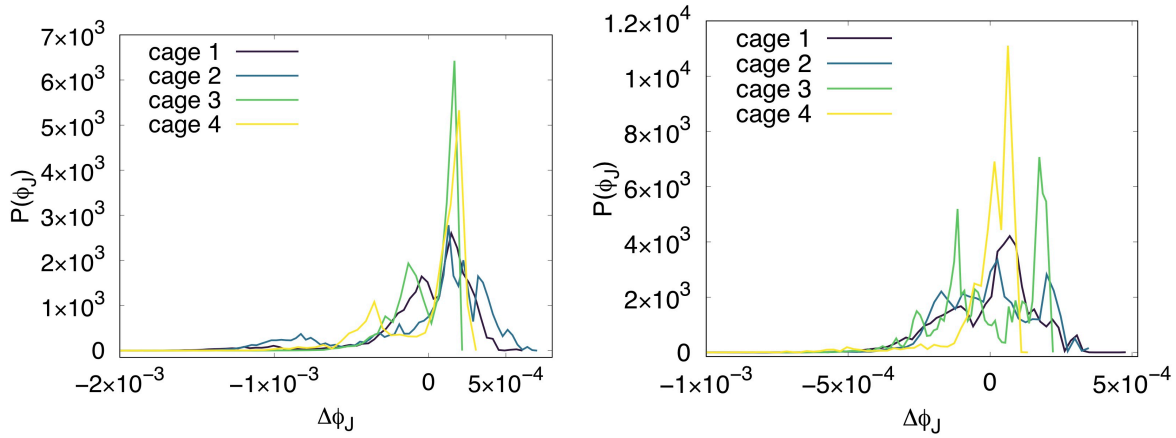

(a) (b)

Figure 3.2.: Probability distribution of the packing fraction of the local minima at jamming, obtained by compressing about 2×10^5 clones. On the x axis, $\Delta\phi_J = \phi_J - \langle\phi_J\rangle$, where $\langle\phi_J\rangle$ is the mean jamming packing fraction of the cage considered. On the y axis, the probability of finding ϕ_J. (a) Results of all the cages generating the clones at $\phi = 0.647$. (b) Results of all the cages generating the clones at $\phi = 0.68$.

from the other 200 deepest and the 200 highest minima of the same sample. Here, α and β are the minima index and i is the particle index; M is the total number of particles excluding the rattlers of both α and β and $\boldsymbol{\delta}$ is the distance of the centers of mass of the two minima. The Δ values have to be compared with the average values of the MSD in the caging regime, which are $\overline{\Delta_{\text{liq}}} := \overline{\text{MSD}}^{0.647}_{\text{plateau}} = 7.3 \times 10^{-3}$ and $\overline{\Delta}^{0.68}_{\text{liq}} := \overline{\text{MSD}}^{0.68}_{\text{plateau}} = 2.6 \times 10^{-3}$. In Fig. 3.3a, is shown the result for cage 1 generating the clones at $\phi = 0.647$. The deepest minimum of this sample appears to be located in a deep well where there are many other very deep minima of the cage (blue line). Moreover, the deepest minimum is far away from the highest minima (green line). We find almost the same behavior in all the samples. In Fig. 3.3b are shown the Δ distributions among the 200 and 1000 deepest minima, having joined the results of all the cages. It is clear that the deepest minima of the landscape in each sample are usually close one to the other.

In a sample, the configuration corresponding to the deepest minimum is usually found many times; however, it is not the one with the greatest number of occurrences. We denote the latter as *the most probable minimum*. Performing the same analyses of Fig. 3.3 on the most probable minimum, we find that it is close to many other highly probable minima; hence, in the landscape at jamming, there is a large basin of attraction made up by large sub-basins of attraction. Furthermore, studying in the same way the properties of the highest minima, we find that they are far apart from all the other minima and do not form a well. They have small basins of attraction. We can imagine them as narrow ponds on the walls of the landscape basins.

Another observable useful to understand the relative position of two local minima at jamming is the overlap [123]. It is defined as

$$Q := Q_{\alpha\beta} = \frac{1}{M} \sum_{i,j}^{1,M} \Theta\Big(a- \mid \boldsymbol{x}_i^{\alpha} - \boldsymbol{x}_j^{\beta} - \boldsymbol{\delta} \mid \Big) \tag{3.6}$$

As in Eq. (3.5), the sum is restricted to the M particles which are non-rattlers in none of the two configurations α and β; $\boldsymbol{\delta}$ is the distance of the centers of mass of α and β. Θ is the

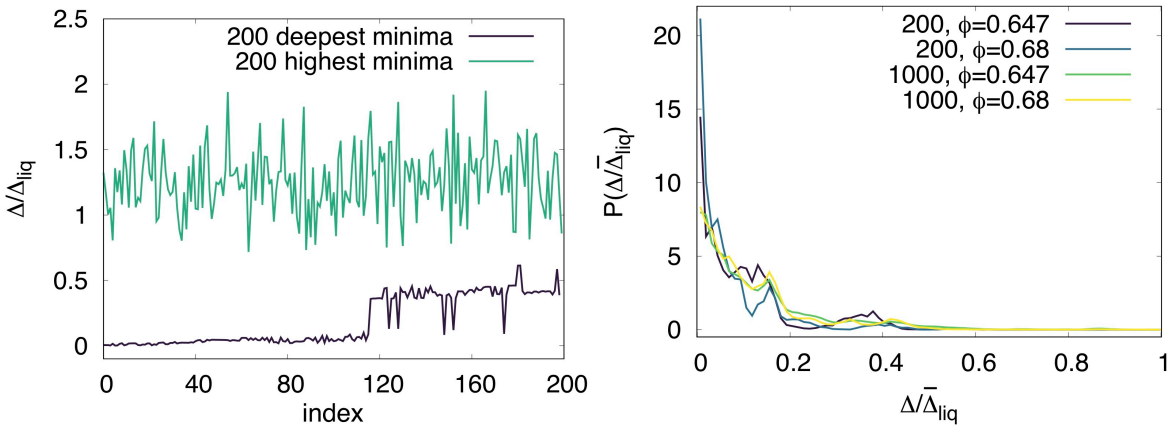

Figure 3.3.: (a) Data of cage 1 generating the clones at $\phi = 0.647$. On the y-axis, the distances Δ among the deepest minimum and the 200 deepest and 200 highest minima of the same sample, normalized to the MSD of cage 1 ($\Delta_{\text{liq}} = 0.0066$). On the x-axis, the index increases as ϕ_J decreases. (b) Δ distributions joining the data of all the cages. On the x axis, Δ is normalized to $\overline{\Delta_{\text{liq}}} = 7.3 \times 10^{-3}$. In blue and azure, the distance distributions among the 200 deepest minima starting the compressions up to jamming from, respectively, $\phi = 0.647$ and $\phi = 0.68$. In yellow and green, the same plots considering the 1000 deepest minima of each sample.

Heaviside step function. We choose $a = 0.03$. $Q \to 1$ when the number of displaced particles decreases. Q gives complementary information to Δ. For instance, a high value of Δ can be due to the presence of only one particle which has very different positions in the two packings α and β; if it is so, Q has a large value. Otherwise, if many particles are displaced by a small amount, the same Δ can correspond to a small value of Q. In Fig. 3.4 is shown the behavior of the overlap Q for the same minima used in Fig. 3.3b. In our results, given a couple of minima α and β there is not a direct correspondence between a high value of Q and a small value of Δ. However, Fig. 3.3b and Fig. 3.4 show that the deepest minima of each sample on average are close in terms of both Q (few particles are displaced) and Δ (small distance). This confirms our description of the landscape structure in terms of deep wells in which the deepest minima are contained.

Hierarchical Structure

According to the mean-field picture, we expect to find a hierarchical, specifically an ultrametric, structure of the basins. To verify this hypothesis, we construct the heatmaps of the 1000 deepest minima of each sample, using the distance Δ as a dissimilarity measure. In Fig. 3.5 are shown the heatmaps of cage 1 and cage 3 for the samples at $\phi = 0.647$ and $\phi = 0.68$, respectively. To provide a quantitative characterization of the clustering properties of the selected minima, we compute the agglomerative coefficient (AC) for each heatmap [7]. The average on all the samples are $\overline{\text{AC}_{0.647}} = 0.994$ and $\overline{\text{AC}_{0.68}} = 0.995$. These high values of AC tell us that the minima have a good clustering structure and, so, present a nearly ultrametric

[7] $\langle \text{AC} = 1 - m(i) \rangle$. For each observation i, $m(i)$ is the dissimilarity to the first cluster it is merged with divided by the dissimilarity of the merger in the final step of the algorithm.

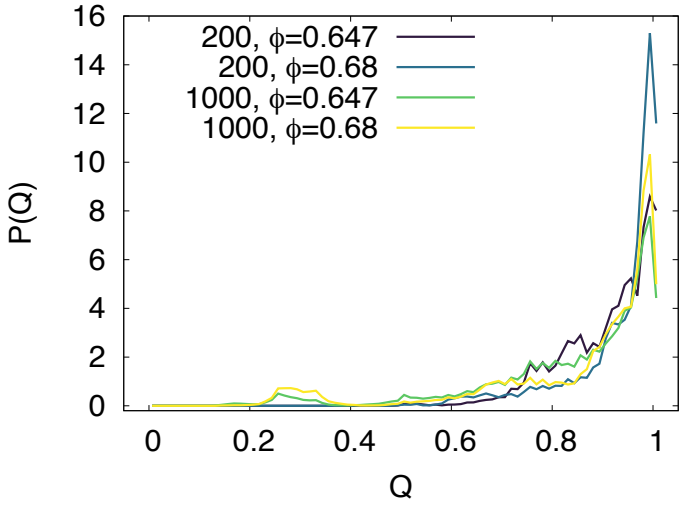

Figure 3.4.: Probability distributions of Q joining the data of all the cages. In blue and azure, the Q distributions among the 200 deepest minima starting the compressions up to jamming from, respectively, $\phi = 0.647$ and $\phi = 0.68$. In yellow and green, the same plots considering the 1000 deepest minima of each sample.

structure.

3.3. Conclusions and outlook

The results shown in the last Section are compatible with the picture expected for mean-field hard spheres. Therefore, their value is twofold. First, they suggest that the iLP algorithm implemented provides the correct picture of the landscape at jamming. Second, they point towards the universality of the jamming transition in hard-sphere systems and suggest the presence of a Gardner transition in finite-dimensional systems that determines the rough and fractal nature of the landscape.

Summarizing, the main features of the jamming landscape in three-dimensional hard spheres that we observed in this study are: (i) all the samples present a huge number of distinct local minima at jamming, showing that the landscape is very complex; (ii) the deepest minima of the landscape are found more often than the highest, and so we argue that their basins of attraction are larger; (iii) the dendrograms constructed with the 1000 deepest minima of each sample have good clustering properties, suggesting that the landscape is organized in an ultrametric structure; (iv) the arrangement of the local minima is compatible with several studies on disordered systems [132]: the deepest minima are close in the configuration space and form a large deep well, while the highest minima do not form a well and have small probabilities of being found; (v) the level statistics at jamming seems to be determined by Poisson statistics, meaning that there is no level-repulsion.

This exploratory study has pointed out that the iLP algorithm can be fruitfully exploited for investigating the properties of finite-dimensional hard spheres at jamming. We hope that it will be extensively employed in the future to unveil further properties of the jamming transition in finite dimensions and confirm results previously obtained by means of soft-sphere approaches. Starting from our qualitative results, one can perform comprehensive studies

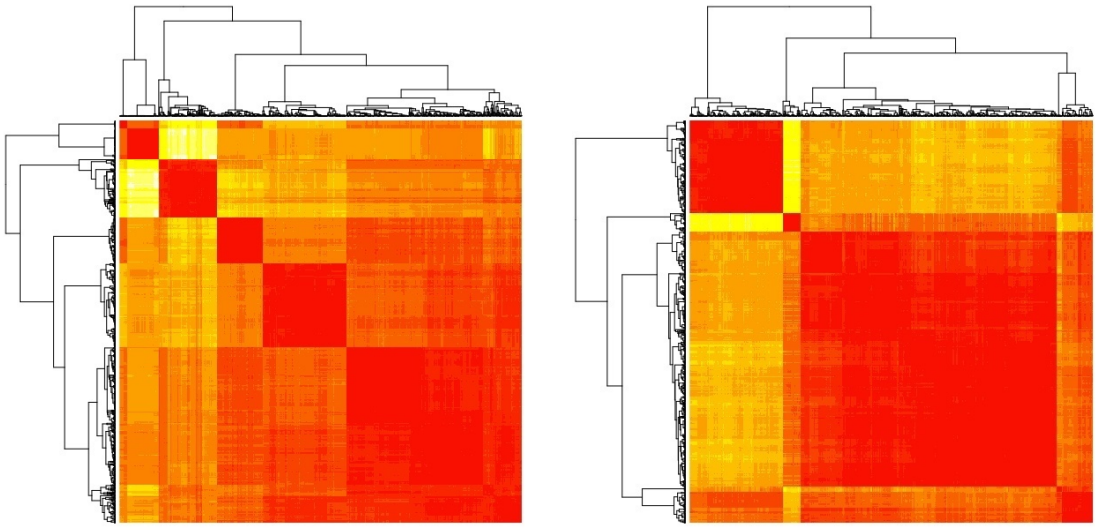

(a) (b)

Figure 3.5.: Heatmaps constructed with the 1000 deepest minima of a sample. (a) Heatmap for cage 1 coming from $\phi = 0.647$. AC $= 0.996$. (b) Heatmap for cage 3 coming from $\phi = 0.68$. AC $= 0.997$. The clusters are made with R using the average method [131].

on the jamming transition within the hard regime. For example, it would be important to increase the number of starting meta-basins, in order to perform good disorder averages and have deep control over sample-to-sample fluctuations. Moreover, repeating the same analysis with systems of different sizes and dimensions would allow one to determine the entity of finite-size effects and to properly extrapolate the thermodynamic limit of the observables. Finally, since it is known [97, 133] that the starting point of the compression plays an important role in determining the strength of the Gardner transition, it would also be important to repeat the analysis by starting from different points on the liquid equation of state and identify, in a clear way, the universal features of the behavior at jamming.

4. Quantum jamming transition: Critical properties of a quantum mechanical perceptron

In this Chapter, we investigate the critical properties of the jamming transition in the quantum mechanical perceptron model. After a brief introduction to the topic, in Section 4.1 we define the quantum perceptron model. Section 4.2 is devoted to the derivation of the self-consistency equations to determine the perceptron free energy within the replica-symmetric ansatz. In Section 4.3, we describe the iterative path integral Monte Carlo algorithm implemented to solve such equations. In Section 4.4, we present in detail the numerical results on the quantum jamming transition of the perceptron model, showing that its critical exponents are different from the classical case, and the quantum critical point is not confined to the zero-temperature axis. The reference article for this Chapter is Ref. [134].

The perceptron is an exceptionally powerful model because of its applications in several research fields, ranging from learning protocols to the effective description of the dynamics of an ensemble of infinite-dimensional hard spheres in Euclidean space. It was introduced in 1958 by F. Rosenblatt [111, 135] who, inspired by human neurons, designed this machine for image recognition. Although it was suddenly realized that the perceptron cannot be trained to recognize many classes of patterns, and it is only a linear classifier [136], nowadays the perceptron is extensively used in learning protocols [137, 138] and constitutes the building block of feed-forward neural networks with two or more layers [139].

The perceptron model belongs to the broad category of constraint satisfaction problems (CSPs) [140], which are nowadays extensively studied at the crossroad of computer science and statistical mechanics. CSPs often exhibit high computational complexity, requiring a combination of heuristics and combinatorial search methods to be solved in a reasonable time. Methods and ideas from the theory of disordered systems have been proposed to shed light on the possible origin of their computational difficulty [141–145] and have inspired efficient algorithms and valuable heuristics [146] to solve them.

A notable example of CSP with continuous variables is the sphere packing problem [110, 147]. As discussed in Chapter 2, sphere systems have gained plenty of attention among the glass physics community, and their jamming transition has been incorporated into the framework of glassy theory [17, 87, 95, 148, 149]. In this context, the perceptron, which is a continuous CSP as well, has been recognized as the simplest mean-field model presenting a jamming transition in the same universality class of high-dimensional sphere systems [110, 147, 150, 151]. Exactly solvable models have always played an important role in increasing our understanding of the physics of glasses, both qualitatively and quantitatively. Therefore, the perceptron promises to be an important viewpoint on these intriguing materials.

Recently, partly motivated by the technological progress in quantum computation [152], many authors have been looking at ways to use quantum dynamics to speed up the solution

of the classical problems. In the realm of discrete variable CSPs, a growing body of literature has investigated the impact of quantum dynamics on the spin-glass transition [153–158], and it has been found that disordered quantum systems display a plethora of new phenomena, such as many-body localization [159–169] (see also Chapter 5). On the other hand, despite the similar importance for computer science, the study of CSPs with continuous variables endowed with quantum dynamics is in its infancy. This is certainly due to the analytical and computational challenges they posit, but their investigation promises to have far-reaching implications. For instance, given the connection of the perceptron model with infinite-dimensional hard spheres, and thus with structural glasses, it might provide clues for the anomalous (i.e. non-Debye) behavior of thermodynamic quantities in glasses at ultra-low temperatures (see Chapter 2). These phenomena, such as $C_V(T \sim 0) \sim T$ [31, 80, 84], discussed in Chapter 1, are indeed naturally explained in terms of quantum mechanics [34, 35], but no firm results or solvable toy models exist (see [55] for a critical view). Indeed, no exhaustive mean-field model for quantum glasses, nor quantum hard spheres, has been developed so far.

The purpose of this Chapter is to address, for the first time, the jamming transition of sphere systems deep in the quantum regime [170] by means of the quantum perceptron model[1]. Employing an iterative path integral Monte Carlo algorithm, we show that quantum mechanical effects change the nature of the critical point radically. We find that, for any $\hbar \neq 0$, the critical exponents are different from the classical ones and independent of the temperature. We also find that $C_V(T \sim 0) \sim e^{-\Delta/T}$ at small T, while at higher temperatures the specific heat has a power-law behavior. Remarkably, the latter result, valid in the deep quantum regime, resembles the semiclassical results of Refs. [113, 172], connecting the physics on the two sides of the jamming transition. This work initiates the exploration of the effects of quantum mechanics on hard spheres and their jamming transition, employing a unique viewpoint as the quantum perceptron model. These results have implications for the ultra-low temperature properties of structural glasses and quantum machine-learning protocols.

4.1. Definition of the quantum perceptron model

The perceptron model can be thought as the model of a particle living on a N-dimensional sphere, subjected to a set of randomly placed obstacles. The vector $\boldsymbol{X}$ represents the position of the particle on the sphere ($\boldsymbol{X}^2 = N$), and the obstacles are represented by the N-dimensional vectors $\boldsymbol{\xi}^\mu = (\xi_1^\mu, \dots, \xi_N^\mu)$, where $\mu = 1, \dots, M = \alpha N$ and ξ_i^μ are independent identically distributed Gaussian random variables with zero mean and unit variance. For each obstacle, the constraint h_μ is defined as

$$h_\mu(\boldsymbol{X}) = \frac{1}{\sqrt{N}} \boldsymbol{\xi}^\mu \cdot \boldsymbol{X} - \sigma > 0. \tag{4.1}$$

Introducing the cost function

$$V = \sum_{\mu=1}^{M} v(h_\mu(\boldsymbol{X})), \tag{4.2}$$

the perceptron can be transformed into an optimization problem.

[1] Notice that the name *quantum perceptron* has been already used in the past for quantum algorithms for learning quantum states [171]. Our problem is different since we implement a quantum dynamics on a classical constraint satisfaction problem.

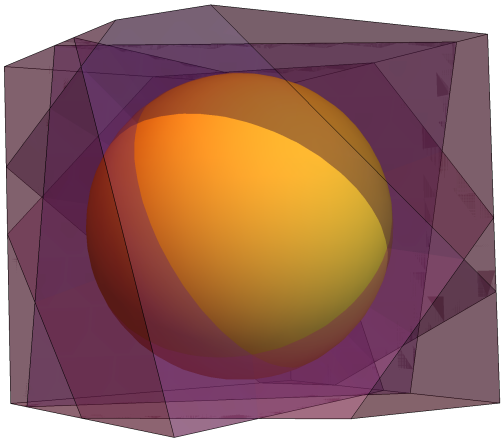

Figure 4.1.: Finite-dimensional representation of the perceptron model at $\sigma = 0$, $N = 3$, $M = 4$. Each constraint is represented by a plane passing through the origin and cuts the sphere in half. The particle can move in the allowed, light orange region on the sphere. The jamming transition is reached when the number of obstacles is such that (with probability 1 in the $N, M \to \infty$ limit) there is no light orange volume left anymore.

However, we are interested in the hard-wall potential case in which

$$v(h) = \begin{cases} 0 & \text{if } h > 0 \\ \infty & \text{if } h < 0; \end{cases} \tag{4.3}$$

hence, we require all the constraints to be satisfied. Fig. 4.1 shows a sketch of the perceptron model with hard-wall potentials for a particular choice of the parameters σ, N, M. However, the model is physically relvant only when the limits $N, M \to \infty$ are taken, keeping $\alpha := M/N$ finite.

The classical system (recovered for $\hbar = 0$) is independent of the temperature and presents two phases, determined by whether there is or there is not any volume left by the intersection of the M constraints. Specifically, one has to consider the limit of the set

$$\mathcal{W} := \bigcap_{\mu=1}^{M} \{\boldsymbol{X} \in \mathbb{R}^N : \boldsymbol{X}^2 = N \wedge h_\mu(\boldsymbol{X}) > 0\} \tag{4.4}$$

as $N, M \to \infty$: in the satisfiable (SAT) phase, a position $\boldsymbol{X}$ for the particle satisfying all the constraints can be found with probability one. In the unsatisfiable (UNSAT) phase, instead, $\mathcal{W}$ becomes empty and the CSP problem has no solution. The sharp SAT-UNSAT transition corresponds to the jamming transition of sphere systems, and it is induced by increasing the constraint density α up to $\alpha_c(\sigma)$.

The properties of the SAT-UNSAT transition depend on σ. In the classical case, the full phase diagram of the model has been solved in Ref. [147]; we report it in Fig. 4.2. Its main features are the following. For $\sigma > 0$, the constraints $\{h_\mu > 0\}$ force the particle $\boldsymbol{X}$ to be closer than some distance to each obstacle; thus, the allowed region is convex. The free

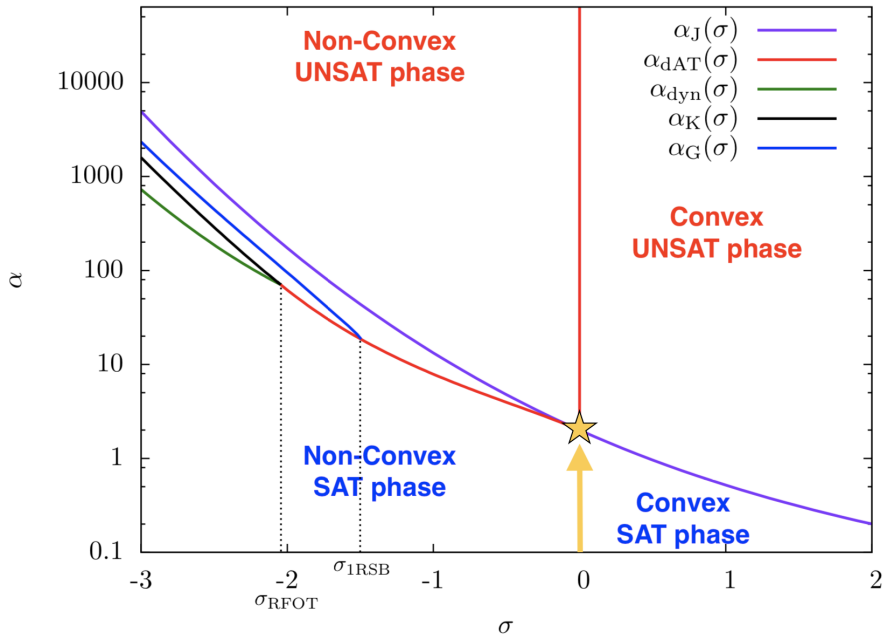

Figure 4.2.: Phase diagram of the classical perceptron model. $\alpha_J(\sigma)$ indicates the jamming transition, or equivalently the SAT-UNSAT threshold, analytically computed within the replica-symmetric (RS) ansatz. The RS ansatz is stable for $\sigma \geq 0$. For $\sigma < 0$, instead, the whole jamming line is contained in a phase in which the landscape is rugged, due to the full breaking of replica symmetry [15]. In particular, dAT stands for de Almeida-Thouless line, dyn for dynamical transition, K for Kauzmann transition, and G for Gardner transition. A complete discussion on the phase diagram of the classical perceptron model and on the diverse transition lines it presents can be found in Refs. [147]. We study the perceptron endowed with quantum dynamics moving along the orange arrow up to the star, i.e. $\sigma = 0$, $\alpha \to 2$. It corresponds to the border of the RS stable region. Picture adapted from [147].

energy has a single minimum and the replica-symmetric (RS) solution is everywhere stable. On the contrary, when $\sigma < 0$, the constraints are satisfied if the particle is away from each obstacle. The allowed region is non-convex and can be composed of disconnected islands. The SAT-UNSAT transition falls within a phase where the landscape is rugged and marginally stable. For our purposes, we will concentrate only on the value $\sigma = 0$, at the border of the RS stable region, for which the jamming point corresponds to $\alpha_c(0) = 2$. In this way, we can reach the jamming point within the RS ansatz, but capturing the physics of the glassy phase ($\sigma < 0$).

We quantize the model by imposing the canonical commutation relations $[\hat{X}_i, \hat{P}_j] = i\hbar\delta_{ij}$. The Hamiltonian reads

$$\hat{H} = \frac{\hat{\boldsymbol{P}}^2}{2m} + \sum_{\mu=1}^{M} v(h_\mu(\hat{\boldsymbol{X}})). \tag{4.5}$$

4.2. Derivation of the self-consistency equations

We wish to compute the quenched free energy of the quantum perceptron model in the RS ansatz [113]. The free energy depends on some variational parameters that can be found self-consistently from the free energy extremization.

The quenched disorder average of the free energy is given by

$$F = -\beta^{-1}\overline{\ln Z}, \tag{4.6}$$

where $Z = \mathrm{Tr}(e^{-\beta H})$ and H is given in Eq. (4.5). Introducing the imaginary times t and s, p replicas whose indices are labelled by $a, b = 1, ..., p$, and the Lagrange multipliers $\lambda_a(t)$ associated to the spherical constraint $\boldsymbol{X}_a^2(t) = N$, one can find F as a function of the overlap matrix

$$Q_{ab}(t,s) = N^{-1}\overline{\langle \boldsymbol{X}_a(t)\cdot\boldsymbol{X}_b(s)\rangle}, \tag{4.7}$$

where $Q_{ab}(t,s)$ is periodic in t and s with period $\beta\hbar$. The quenched free energy f, per dimension N and per replica p is given by

$$\begin{aligned} -\beta p f = \frac{1}{2}\ln\det\hat{Q}(t,s) + \frac{m}{2\hbar}\sum_a\int_0^{\beta\hbar} dt\,\partial_s^2 Q_{aa}(t,s)|_{s=t} \\ - \frac{m}{2\hbar}\sum_a\int_0^{\beta\hbar} dt\,\lambda_a(t)(Q_{aa}(t,t)-1) + \alpha\ln\zeta, \end{aligned} \tag{4.8}$$

where

$$\begin{aligned} \zeta = \exp\left(\frac{1}{2}\sum_{a,b}\iint_0^{\beta\hbar}\frac{dt}{\beta\hbar}\frac{ds}{\beta\hbar}Q_{ab}(t,s)\frac{\delta^2}{\delta r_a(t)\delta r_b(s)}\right) \\ \cdot\exp\left(-\frac{1}{\hbar}\sum_c\int_0^{\beta\hbar}dt\,v(r_c(t))\right)\Big|_{r_c(t)=0}. \end{aligned} \tag{4.9}$$

The RS ansatz for the saddle point consists in the assumption:

$$Q_{ab}(t,s) \overset{\mathrm{RS}}{=} [q_d(t-s) - q]\delta_{ab} + q \tag{4.10}$$

where the off-diagonal order parameter $q = N^{-1}\overline{\langle \boldsymbol{X}_a(t)\cdot\boldsymbol{X}_b(s)\rangle}$ (for $a\neq b$ and any t,s) is the overlap of two different replicas and is the analog of the Edwards-Anderson order parameter, while $q_d(t) - q = N^{-1}\overline{\langle \boldsymbol{X}_a(t)\cdot\boldsymbol{X}_a(s)\rangle} - q$ is the autocorrelation function of a replica. As usual, one shall send $p\to 0$ after computing the quantities involving Q. We need to find the saddle point with respect to variations of Q, namely of $q_d(t)$ and q, and $\mu := m\lambda$. To do this, it is convenient to define

$$G(t-s) := q_d(t-s) - q. \tag{4.11}$$

From the $\beta\hbar$-periodicity in imaginary time, we can consider as variables the countable set of Fourier components of $G(t)$, i.e. $\{G_n\}_{n\in\mathbb{Z}}$; we define the Fourier transform as

$$\bullet\,(\omega) := \int_0^{\beta\hbar}\frac{dt}{\beta\hbar}e^{-i\omega t}\bullet\,(t), \quad \bullet_n := \bullet(\omega_n), \tag{4.12}$$

$\omega_n := 2\pi n/\beta\hbar$ being the Matsubara frequencies.

Then, the quenched free energy in the RS approximation, per dimension N and replica p, is

$$-\beta f = \frac{1}{2}\sum_{n\in\mathbb{Z}}\ln G_n + \frac{q}{2G_0} - \frac{\beta m}{2}\sum_{n\in\mathbb{Z}}\omega_n^2 G_n - \frac{\beta\mu}{2}\Big[\sum_{n\in\mathbb{Z}}G_n - (1-q)\Big] + \alpha\gamma_q\star\ln\langle e^{-\beta\int_0^{\beta\hbar}\frac{dt}{\beta\hbar}v(r(t)+h)}\rangle_r, \tag{4.13}$$

where

$$\gamma_q\star\bullet(h) := \int_{-\infty}^{\infty}\frac{dh}{\sqrt{2\pi q}}e^{-h^2/2q}\bullet\,(h), \tag{4.14}$$

and we introduced a one-dimensional, $\beta\hbar$-periodic auxiliary process $r(t)$ with the same autocorrelation function:

$$\langle\bullet\rangle_r := \frac{1}{Z_0}\oint Dr\, e^{-\frac{1}{2}\int\int_0^{\beta\hbar}\frac{dt}{\beta\hbar}\frac{ds}{\beta\hbar}r(t)G^{-1}(t-s)r(s)}\bullet \tag{4.15}$$

with Z_0 a suitable normalization. Notice that the free energy in Eq. (4.13) is divergent. In Ref. [113] it is shown how to properly regularize and renormalize it. In particular, one finds that thermodynamic observables, like the specific heat and the order parameter, are divergence-free.

The saddle-point equations for the parameters G_n, μ and q are

$$G_n^{-1} = \beta m\omega_n^2 + \beta\mu + \beta\Sigma_n \tag{4.16}$$

$$\sum_n G_n = 1 - q \tag{4.17}$$

$$q = \alpha\gamma_q\star\langle r_0\rangle_v^2 \tag{4.18}$$

where we defined the self-energy as

$$\Sigma_n := \alpha\big(G_n^{-1} - G_n^{-2}\gamma_q\star(\langle r_n^* r_n\rangle_v - \delta_{n0}\langle r_0\rangle_v^2)\big)/\beta, \tag{4.19}$$

with

$$\langle\bullet\rangle_v := \frac{\langle e^{-\beta\int_0^{\beta\hbar}\frac{dt}{\beta\hbar}v(r(t)+h)}\bullet\rangle_r}{\langle e^{-\beta\int_0^{\beta\hbar}\frac{dt}{\beta\hbar}v(r(t)+h)}\rangle_r}. \tag{4.20}$$

For later convenience, we fix $\Sigma_0 = 0$.

The equations (4.14)-(4.20) define self-consistently the dynamics of the auxiliary random process $r(t)$. To solve them, we have implemented an iterative method, together with a Monte Carlo sampling able to calculate $\langle\bullet\rangle_r$. This is illustrated in the next Section 4.3. An analog calculation has been performed for the SK model in Refs. [173–176].

4.3. Iterative solution of the self-consistency equations

We wish to solve the self-consistency equations (4.14)-(4.20) for the parameters G_n, μ and q. This can be done numerically, by means of a path integral Monte Carlo (PIMC) on the auxiliary random process $r(t)$.

The parameters G_n, μ, and q can be initialized with arbitrary values. However, to accelerate the numerical convergence, it is convenient to proceed in a stepwise manner, from smaller to higher α's. The algorithm is composed of three steps.

The first step is to compute the self-energy Σ_n, defined in Eq. (4.19) and use it to update the autocorrelation function G_n, iteratively. However, the computation of the self-energy involves the averages $\langle \bullet \rangle_v$. To evaluate them, we use the PIMC simulating the dynamics of the $\beta\hbar$-periodic process $r(t)$, in the potential generated by $G^{-1}(t-s)$ and $v(r(t)+h)$, as sketched in Fig. 4.3. The former, when $\Sigma_n \equiv 0$, contains a kinetic term $(m\omega_n^2/2)$ plus a harmonic potential $(\mu/2)$; the latter is the hard-wall potential which forces $r(t) > -h$. When $\Sigma_n \neq 0$ both contributions (kinetic and potential) change, and the dynamics of $r(t)$ becomes non-trivial.

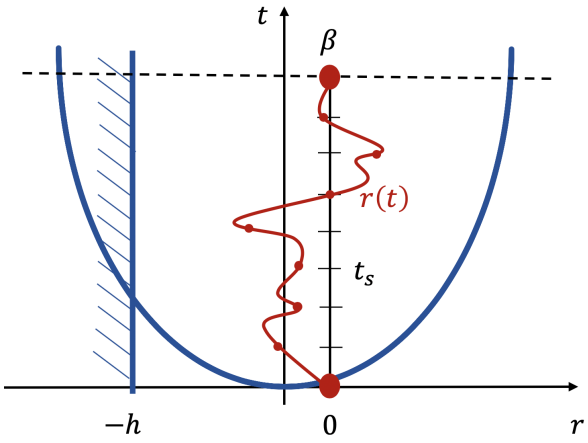

Figure 4.3.: Sketch of the path integral Monte Carlo (PIMC) used to simulate the dynamics of the $\beta\hbar$-periodic process $r(t)$ ($r(0) = r(\beta\hbar)$) in the potential generated by $G^{-1}(t-s)$ and $v(r(t)+h)$. The PIMC consists in proposing a move $r(t_s) \to r(t_s) + \delta(t_s)$ for every time step t_s, which is accepted or rejected according to the Metropolis algorithm. We improved this simple scheme using both the method of images and the rigid movement of the time chain $r(t_s)$, as discussed in the text.

Numerically, it is convenient to consider the period of the process as β, reabsorbing $\hbar$ in the mass $m \to m/\hbar$. Moreover, the period has to be discretized: the number of Trotter slices is $S = \beta/a$, where a is the time-slice amplitude, and, setting $\beta = 2^L$ and $a = 2^{-K}$, it holds $S = 2^{L+K}$. In this way, we can define a discrete Fourier transform $f_n = \frac{1}{S}\sum_{s=0}^{S-1} f(t_s)e^{i\omega_n t_s}$ where $\omega_n = 2\pi n/\beta$ with $n \in [0, S-1]$. Thus, increasing β the set $\{\omega_n\}$ becomes denser, while decreasing a one can access higher frequencies.

The PIMC algorithm consists in proposing a move $r(t_s) \to r(t_s) + \delta(t_s)$ for every time step t_s, which is accepted or rejected according to the Metropolis algorithm with weight given by G^{-1} and v. However, the presence of the hard-wall potential makes the convergence of the Monte Carlo very demanding, and it is not sufficient to reject the attempted moves with $r < -h$ to have a good numerical protocol. Thus, we implemented an improved Monte Carlo

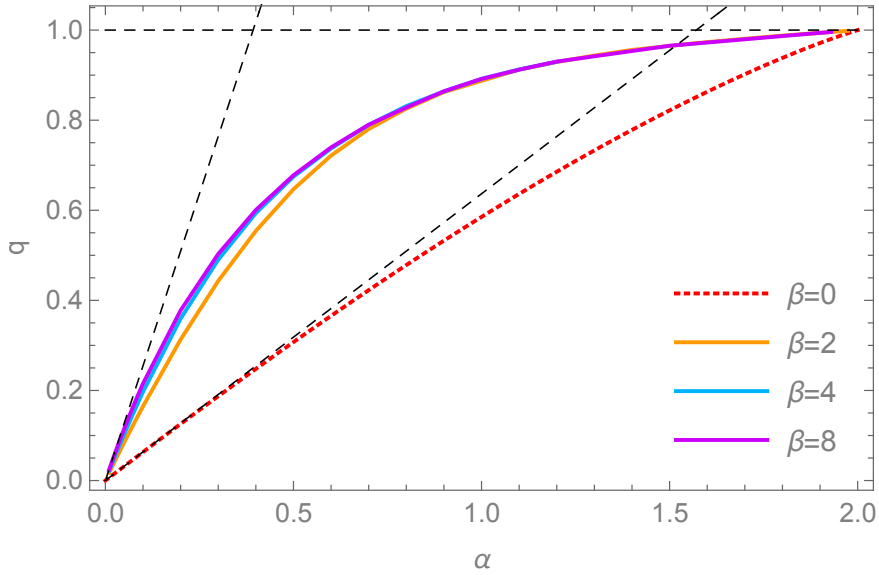

Figure 4.4.: Edwards-Anderson order parameter as a function of the constraint density α for various temperatures. From bottom to top: infinite temperature classical dynamics (red, dotted line) to finite temperature quantum dynamics ($\beta = 2, 4, 8$). The $O(\alpha)$, $\beta = \infty$ results are shown as dashed black lines (while the horizontal black line is a reference for the value $q = 1$). Notice how, as soon as $\alpha \gtrsim 1$, the temperature dependence of q is effectively lost (it is $\sim e^{-c\beta/(2-\alpha)^2}$).

sampling which exploits the method of images. We modified the free particle kinetic term of the Hamiltonian ($m\omega_n^2/2$), and, instead of sampling the probability $P(r_0, 0 \mid r_0, \beta)$ of the free particle, we used $P(r_0, 0 \mid r_0, \beta) - P(\mathrm{Im}(r_0), 0 \mid r_0, \beta)$ where $\mathrm{Im}(r_0) = -r_0 - 2h$ is the image of r_0 when the wall is in $-h$. Another expedient we adopted is to add a move which translates rigidly the time chain $r(t_s)$, i.e. $r(t_s) \to r(t_s) + \delta$ with δ independent of t_s.

The presence of the convolution $\gamma_q \star \bullet(h)$ in the definition of Σ_n (Eq. (4.19)) implies the evaluation of $\langle \bullet \rangle_v$ for many positions $-h$ of the wall. We approximate this Gaussian integral with the Gauss-Hermite quadrature, always with, at least, 10 sample points. This first step of the iterative method stops when G_n is converged for every n within a fixed tolerance (we fixed the relative difference between G_n^{old} and G_n^{new} to be $< 0.1\%$).

The second step is to check if the converged G_n verifies the identity in Eq. (4.17). If it does so, we can go to the third step; otherwise, μ is changed via the bisection method and the first step is performed again.

The third step consists in computing the right-hand side of Eq. (4.18) with the converged G_n and μ and check if the identity in Eq. (4.18) is verified. If it is so, we have found the parameters which solve the self-consistency equations; if not, q is changed and one has to repeat the procedure from the first step.

4.4. Numerical results

As a first result, we present the behavior of the order parameter q as a function of α for various β; it is plotted in Fig. 4.4 against the classical counterpart $q_{\mathrm{cl}}(\alpha)$, obtained at $\hbar =$

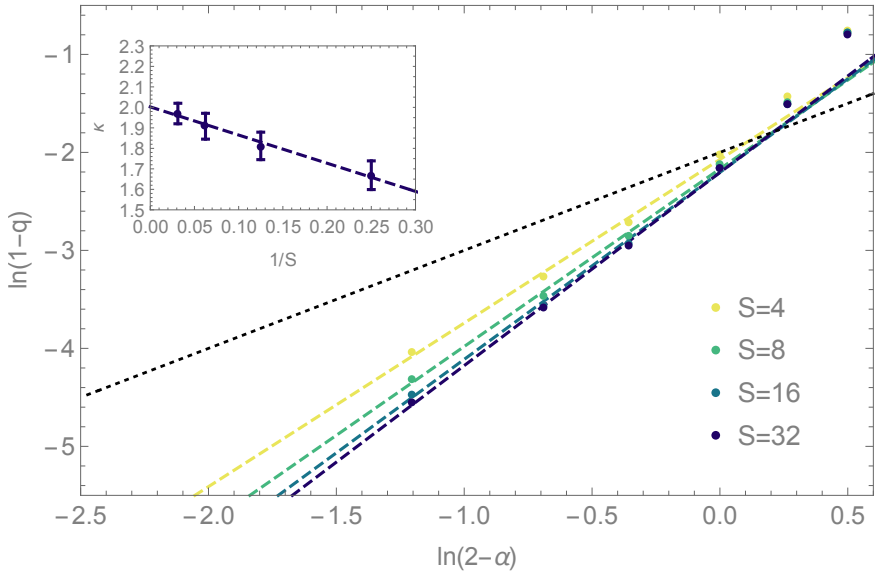

Figure 4.5.: Edwards-Anderson order parameter close to the critical point $\alpha = 2$. From top to bottom, increasing the number of Trotter slices $S = 4, 8, 16, 32$ for sufficiently large β, the slope increases. For reference, the classical value of the slope (from $(1 - q) \sim (2 - \alpha)$) is shown as the diagonal dotted black line. In the inset are shown the values of the slope with their errors, and its extrapolation to $S \to \infty$ to the value $\kappa = 2.0 \pm 0.1$, quoted in the text.

0 [147]. Unlike the quantum case, $q_{\rm cl}(\alpha)$ is independent of the temperature and goes to 1, for $\alpha \to \alpha_c = 2$, with the critical exponent $\kappa_{\rm cl} = 1$ (valid for $\sigma \geq 0$, while for $\sigma < 0$ one has $\kappa_{\rm cl} = 1.41574...$ [147]). It is known [147] that $(1 - q_{\rm cl}(\alpha)) \simeq \frac{1}{4}(2 - \alpha)$.

We find that the value of q for $\hbar > 0$ is always larger than the classical one. This can be easily understood from the following argument: the ground state of a quantum particle in a billiard is more concentrated than a flat distribution on the billiard table, because of the Dirichlet boundary conditions on the walls. Moreover, it becomes more concentrated the larger the aspect ratio of the billiard, namely if one of the sides is larger than the others. Quantitatively, one finds $q > q_{\rm cl}$ already at lowest order in α. Indeed, from the self-consistency equations (4.14)-(4.20), $q = \alpha \langle r_0 \rangle^2_{v(h=0)} + O(\alpha^2)$ where the average $\langle \bullet \rangle_{v(h=0)}$, when $\beta \to \infty$, indicates the expectation value over the ground state of a harmonic oscillator with a wall in the origin. This problem is easily solved and one finds $q = \frac{8}{\pi}\alpha + O(\alpha^2)$, to be compared with $q_{\rm cl} = \frac{2}{\pi}\alpha + O(\alpha^2)$.

Fig. 4.4 shows that the quantum order parameter q depends on the temperature $T = 1/\beta$ for $\alpha \lesssim 1$, and then, increasing α, becomes independent of T through a crossover. This can be easily understood considering that, from the classical calculation, we expect the typical linear size of the allowed region for the particle on the sphere to vanish as $\ell \sim \sqrt{1 - q_{\rm cl}} \sim \sqrt{2 - \alpha}$ for $\alpha \to 2$. Thus, as soon as the energy gap to the first excited state becomes larger than the temperature, i.e. roughly when $\frac{\hbar^2}{m(1-q_{\rm cl})} \sim \frac{\hbar^2}{m(2-\alpha)} \gtrsim T$, the quantum dynamics is *effectively at zero temperature* and the order parameter q becomes independent of T. Moreover, in the following we will show that the gap, deep in the quantum regime, grows even faster than $(2 - \alpha)^{-1}$ when $\alpha \to 2$. Since the quantum dynamics recovers the classical dynamics only when the de Broglie wavelength $\lambda_T \sim \hbar/\sqrt{mT} \ll \ell$, on approaching jamming quantum mechanics dominates. Hence, for any $T, \hbar, m$, as $\alpha \to 2$ one eventually enters a quantum

critical regime, where quantum mechanics controls the dynamics and defines, among other things, novel critical exponents. The classical result is recovered only by taking the limit $T \to \infty$ before $\alpha \to 2$.

The value of the critical exponent κ regulating the relation $(1-q) \sim (2-\alpha)^{\kappa}$ in the quantum regime can be extracted by looking at the low-temperature, large-α data. As usual, a sufficiently large number of Trotter slices S must be taken, and it increases as $\alpha \to 2$, making the numerical simulations more demanding. However, fortunately, the asymptotic region is reached already at $\alpha \gtrsim 1$. The data in Fig. 4.5 clearly show that the critical exponent of the quantum theory is not the classical one, $\kappa_{\text{cl}} = 1$, and it departs more and more from it as the number of Trotter slices is increased. We have performed a log-log fit to extract such critical exponent, in a region of $\alpha \in [1, 1.7]$. Extrapolating $S \to \infty$, we find $\kappa = 2.0 \pm 0.1$ (Fig. 4.5).

That $\kappa > 1$ in the quantum case can be understood also from a simple variational calculation, discussed in Appendix A.1. Here we just mention that, using in the scaling region $\alpha \to 2$ the (uncontrolled) approximation $G_n^{-1} = \beta m(\omega_n^2 + \hbar^2/4m^2)/(1-q)$, we are able to solve explicitly the self-consistency equations for $\beta \to \infty$, finding $\kappa = 3/2$. The value $\kappa \simeq 2$ from the Monte Carlo simulations presumably comes once the true behavior of $\Sigma(\omega)$ is considered.

One can also study the (regularized) internal energy per degree of freedom, which is

$$u = \frac{1}{2\beta} \sum_{n \in \mathbb{Z}} \frac{\mu + \Sigma_n}{m\omega_n^2 + \mu + \Sigma_n}, \tag{4.21}$$

as derived in Ref. [113]. We find that u is independent of β, like q, already at $\alpha \gtrsim 1$, but it strongly depends on the number of Trotter slices S. Extrapolating the data for $S \to \infty$ we obtain the result in Fig. 4.6, which shows a divergence of the energy as $\alpha \to 2$. This can be again interpreted in terms of reduced volume and uncertainty principle. In particular, we observe that $u \sim \frac{\hbar^2}{m(2-\alpha)^2}$ with good accuracy for $\alpha \to 2$, in a region where the dependence on β is lost. This confirms the result $\kappa \simeq 2$, obtained from the behavior of q in Fig. 4.5.

Summarizing, we have just shown that, at fixed temperature, in the quantum regime the critical properties of the system are determined by the ground state, and the gap to the first excited state grows as $\Delta \sim \frac{\hbar^2}{m(1-q)}$ for $\alpha \to 2$. This implies that, if we focus on frequencies $\omega \ll \Delta/\hbar$, or times $t \gg \hbar/\Delta$, there is no dynamics. In order to see some dynamical behavior, one should consider $G(\omega \gtrsim \Delta/\hbar)$. As shown in Fig. 4.7, at these large frequencies the form of the self-energy $\Sigma(\omega)$ changes significantly. Indeed, at any $\alpha < 2$, the self-energy is an analytic function of ω^2 in a neighborhood of the origin $\omega = 0$ (inset of Fig. 4.7). As $\alpha \to 2$, this behavior becomes extended to increasing values of ω. At larger frequencies, however, $\Sigma(\omega)$ develops a linear behavior. Moreover, for any $\alpha < 2$, $\lim_{\omega \to \infty} \Sigma(\omega) = 0$, as can be seen from its definition in Eq. (4.19). Performing a log-log fit, we find that the constant contribution to the autocorrelation function scales as $\beta\mu \sim (1-q)^{\delta}$ where $\delta \simeq -0.9$. From a quadratic fit of $\Sigma(\omega)$ at small ω, the coefficient of the quadratic term results instead almost independent of $(1-q)$.

The behavior of $\Sigma(\omega)$ defines the effective dynamics of the theory, and its analytical properties around the origin determine the low-temperature behavior of thermodynamical observables. Both the analyticity of $\Sigma(\omega)$ around $\omega = 0$ and the independence of β of all the observables, including the internal energy u, show that the specific heat is non-analytic in T when $\alpha \to 2$. More precisely, our findings show that $C_V(T \sim 0) \sim e^{-\Delta/T}$, due to the presence of the gap. However, since at not-so-small ω it holds $\Sigma(\omega) \sim |\omega|$, the specific heat presents a power-law behavior at high enough temperatures, i.e. $C_V(T > T_{\text{cutoff}}) \sim T^{\gamma}$. Since $\Delta \to \infty$ as $\alpha \to 2$, $T_{\text{cutoff}} \to \infty$ too.

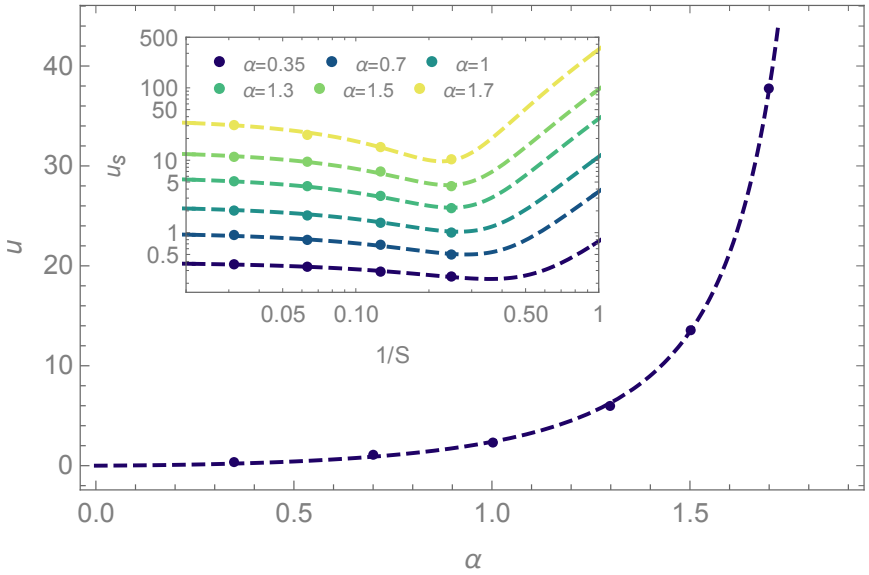

Figure 4.6.: Internal energy u as a function of the density of constraints α. The dashed line is a fit of the form $u = A(2-\alpha)^{-\kappa}(1+B(2-\alpha)+C(2-\alpha)^2)$ with $\kappa = 2.0$ obtained from the behavior of order parameter q. This confirms $u \sim (1-q)^{-1} \sim (2-\alpha)^{-2}$ as discussed in the text. In the inset one can see, from bottom to top for $\alpha = 0.35, 0.5, 0.7, 1, 1.3, 1.5, 1.7$, the extrapolation of the values of $u_S = u + a/S + b/S^2$ as a function of the number of Trotter slices S (in log-log scale).

The linear dispersion $\Sigma(\omega) \sim |\omega|$, observed in the critical regime, reminds us of the result of Ref. [113], where the authors perform a semiclassical analysis to investigate the UNSAT phase with soft potentials. In Ref. [113], they sent $\hbar \to 0$ with $\hbar/T$ kept fixed, while in our study $\hbar$ is kept finite. They found the linear dispersion $\Sigma(\omega) \sim |\omega|$ in a neighborhood of the origin $\omega = 0$, implying a power-law behavior of $C_V(T)$ at small T near the jamming point. The similarities between the two results are surprising since the regimes considered are different, and suggest that the linear dispersion $\Sigma(\omega) \sim |\omega|$ might be a universal feature of quantum models near jamming.

4.5. Conclusions and outlook

This Chapter contained the investigation of the jamming transition of the quantum perceptron model with hard-wall potentials, which can be considered a mean-field model for quantum hard spheres. Starting from the replicated, quenched free energy in the replica-symmetric approximation, one finds a quantum critical point corresponding to the classical jamming point at $\alpha_c = 2$ for $\sigma = 0$. While usually quantum critical points are confined and influence the physics around $T = 0$ [177], the quantum jamming critical point exists *for any temperature*: the classical results are recovered only by taking $T \to \infty$ before $\alpha \to \alpha_c$; therefore, it is the classical critical point to be confined at $T = \infty$. The robustness with temperature of the quantum critical point can be grasped through the following argument. Since the energy gap between the ground and the first excited state increases as the jamming point is approached ($\alpha \to \alpha_c$), for any fixed temperature T^*, there is a threshold value α^*, such that for $\alpha > \alpha^*$ the system cannot by excited anymore, and it remains effectively at zero temperature.

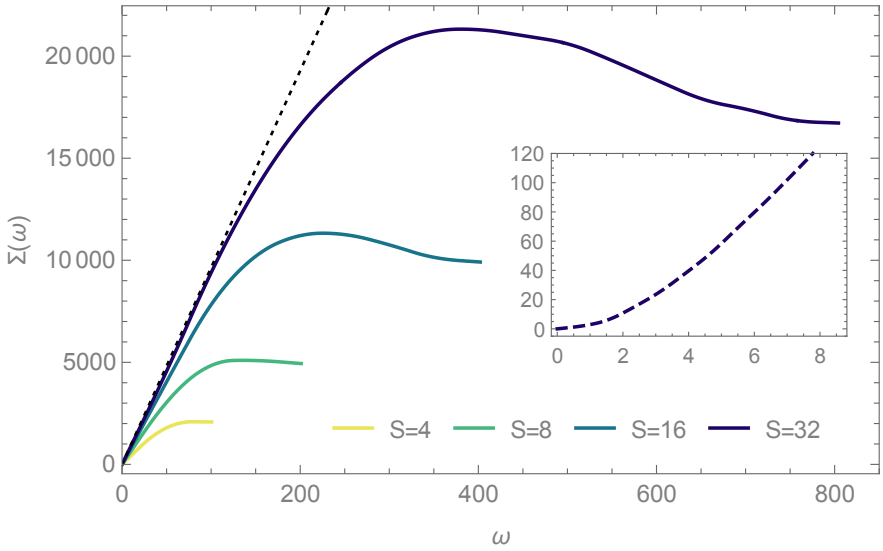

Figure 4.7.: Self-energy $\Sigma(\omega)$ at $\alpha = 1.7$, $\beta = 1/2^3$ as a function of the Matsubara frequency ω, for increasing number of Trotter slices (accessing higher and higher frequencies). We see that $\Sigma(\omega)$ develops a linear ω behavior (black, dotted line) for intermediate ω's, while retaining its analyticity in terms of ω^2 around the origin for any $q < 1$ (inset). In the inset, it is shown $\Sigma(\omega)$ at small ω's for $\alpha = 1.5$, $\beta = 8$.

We find quantum critical exponents different from the classical ones, and an exponentially small $C_V(T)$ at small T. The dispersion relation $G(\omega)^{-1} \sim |\omega|$ for frequencies higher than the gap, but not asymptotically large, implies a power-law specific-heat for $T > T_{\text{cutoff}}$, where T_{cutoff} diverges at the critical point. This shows a surprising connection with the findings of the semiclassical analysis in Ref. [113], where a different region of parameters was considered, that deserves to be further investigated.

An appealing extension of this research would be to consider soft potentials, having a finite[2] $v' \equiv \partial v/\partial r|_{r=0}$, as in the case of structural glasses. Employing soft potentials, it is possible to access the UNSAT phase deep in the quantum regime. We do expect that the quantum jamming transition will turn into a crossover (like the classical one does) but the same phenomenology outlined in Section 4.4 should be observed as far as the change in the potential on length scales $O((1-q)^{1/2})$ is large with respect to the gap $\Delta \sim (1-q)^{-1}$. This means that for $(1-q) \gtrsim (v')^{-2/3}$, or $\alpha \lesssim 2 - c(v')^{-1/3}$, the physics is dominated by the hard-wall quantum jamming critical point. The robustness with temperature of the quantum critical point, shown in our results, implies that the quantum character of the system even with soft potentials cannot be neglected. Therefore, it suggests that the standard approaches used to study glassy systems at ultra-low temperatures, which add quantum effects on top of the classical landscape [38, 178, 179], might be inadequate.

Another interesting development of this study would be to move to the regions with $\sigma \neq 0$. The case $\sigma > 0$ is studied in learning protocols. Here, the same methods adopted in our study can be implemented, and one can directly investigate the effects of quantum dynamics. In the region $\sigma < 0$, instead, it is also necessary to solve the self-consistency equations in the replica symmetry breaking framework. As the allowed volume becomes clustered, quantum effects may play a double role: for low disorder, tunneling may help the particle to explore

[2] To be more precise, a similar reasoning applies also for the case $v' = 0$ but $\partial^k v/\partial r^k|_{r=0} \neq 0$ with $k > 1$.

many disconnected flat regions, and speed up the search of solutions (as it happens in the quantum random energy model [164, 168, 169]); for high disorder, Anderson localization may take place, breaking ergodicity and changing significantly the classical phase diagram. The interplay of these behaviors, hard to be guessed, deserves a complete investigation.

Part II.

Quantum dynamics

5. Introduction to Part II

Many-body localization is a novel, non-ergodic state of matter that exists only in the quantum realm. Many-body localized (MBL) systems can elude going to thermal equilibrium even at infinite time. In this sense, they clearly resemble classical glasses, which remain trapped in metastable states for all experimentally accessible time scales. This Chapter is meant as a brief, utterly inexhaustive introduction to the main theoretical notions and phenomenological properties of MBL systems. Such background will be exploited in Part II to show the presence of previously unknown points of contact between the physics of glasses and MBL systems.

In 1958, P. W. Anderson began the study of localization in quantum systems, investigating the problem of a single quantum particle moving in a disordered crystal in d dimensions [180]. The behavior of such particle can be modeled by a tight-binding Hamiltonian, of the form:

$$H_{\text{Anderson}} = J \sum_{\langle ij \rangle} c_i^\dagger c_j + \sum_i \mu_i c_i^\dagger c_i, \tag{5.1}$$

where $c_i^\dagger, c_i$ are the creation/annihilation operators of site i, J is the hopping amplitude between nearest-neighbor sites, and μ_i is a random chemical potential with zero mean and variance W^2. After Anderson's paper, many authors have focused on the single-particle localization problem. It has been found that, in $d = 1, 2$ and for random uncorrelated disorder, all states are localized for arbitrarily weak disorder ($W > 0$) , while in $d \geq 3$ the system is localized only if disorder is sufficiently large ($W > W_c > 0$) [181]. P. W. Anderson in his seminal work proposed also that localization might survive in a weakly interacting many-particle system. However, exploring the effects of introducing a finite density of particles and a generic two-body interaction in the Hamiltonian (5.1), when the single-particle states are all localized, is a hard task, and this fundamental question remained unanswered for many years. The existence of *many-body localization* has been established only recently when Refs. [182, 183] have analytically shown that localization is stable to short-range and sufficiently weak interactions.

Recent years have witnessed several advances in our understanding of the dynamics of quantum many-body systems. On the one hand, the mechanism by which thermal equilibrium appears in isolated quantum systems has been explained via the eigenstate thermalization hypothesis (ETH) [184–187], and its connection to the classic von Neumann ergodic theorem has been made clear [188]. The ETH states that, in ergodic systems, the individual excited eigenstates, $|E_n\rangle$, locally reproduce the thermodynamic ensembles. In other words, it states that the expectation value of a local observable O on an eigenstate, $\langle E_n|O|E_n\rangle$, coincides with the microcanonical expectation value at energy $E \approx E_n$; thus, it depends smoothly on the energy of the eigenstate. Assuming in addition that the off-diagonal matrix elements, $\langle E_n|O|E_m\rangle$, decay exponentially with the system size, the ETH guarantees that out-of-equilibrium initial states relax to states that are locally thermal. On the other hand, many-body localization has been recognized as a generic mechanism by which quantum systems can *avoid* going to thermal equilibrium [162, 165, 189–195]. Many-body localized

(MBL) eigenstates do not follow the ETH requirements: the expectation value of a local observable does equilibrate in time, although to a highly non-thermal value that carries information about the initial state and strongly fluctuates between eigenstates that have similar energies.

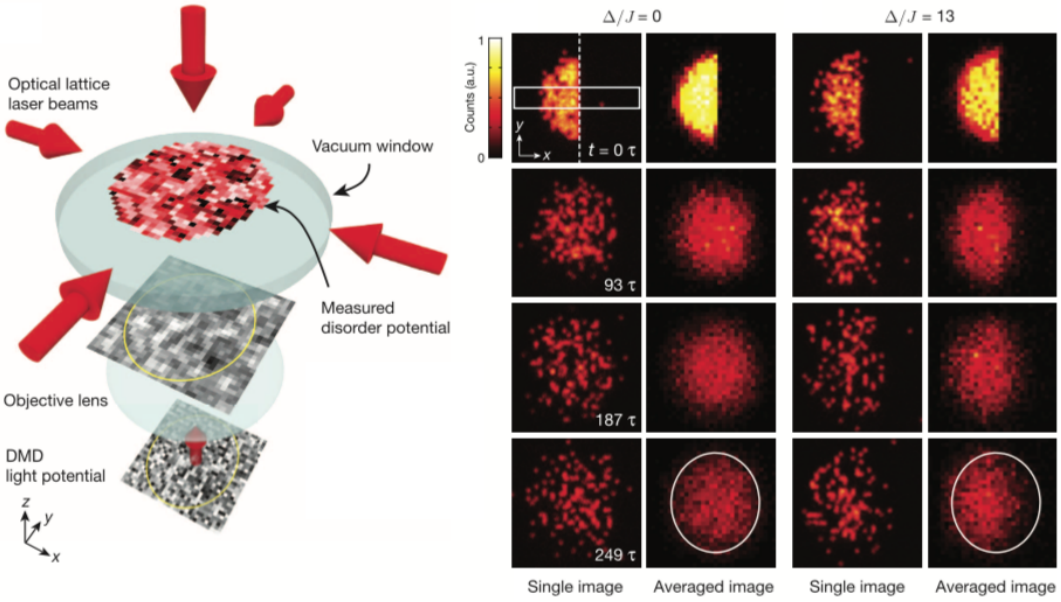

(a) (b) (c)

Figure 5.1.: Probing many-body localization in a two-dimensional system of interacting ultracold bosons. The probing consists in tracking the quantum evolution of an initial state which has a high-energy density and is far from equilibrium. (a) A two-dimensional, almost random disorder potential is imaged onto a single atomic plane in an optical lattice. (b) Raw fluorescence image showing the evolution of an initial domain wall of a bosonic Mott insulator (first row). The left column shows single images, while the right column shows the density distribution averaged over 50 disorder realizations. We see that the density step is smeared out after few tens of tunneling time, τ. (c) In the presence of sufficiently strong disorder, even for long evolution times, $t \simeq 250\,\tau$, the signatures of the initial state are visible: the system does not relax. Figure adapted from [196].

The existence of the non-ergodic, many-body localized phase of matter has been confirmed numerically in a vast set of microscopic models [130, 189, 191, 198–202], and observed in ultracold atoms experiments [196, 203–206]. Fig. 5.1 depicts one of the first experimental observations of a localized phase in a disordered two-dimensional[1] optical lattice of bosons. However, except for a few exploratory experiments [216–218], the observation of the MBL phase in real materials is still in its infancy, mainly due to the difficulty in finding real material whose degrees of freedom are weakly coupled to thermal baths, e.g. phonons.

[1] While the existence of an MBL stable phase is well established for one-dimensional systems at large disorder, in higher dimensions the situation is still not completely clear, partly due to the lack of efficient numerical methods to investigate large system sizes. Even if recent experiments on two-dimensional optical glasses claimed to have observed a transition to an MBL phase [196, 207, 208], the question on whether this phase can be stable in $d \geq 2$ is currently under debate [209–215]. The proposed mechanism for thermalization is based on the presence of rare resonating regions whose effect, however, manifests on long time scales (of the order of the system size) [209]. Therefore, the localized picture can be considered accurate at least at short and intermediate time scales.

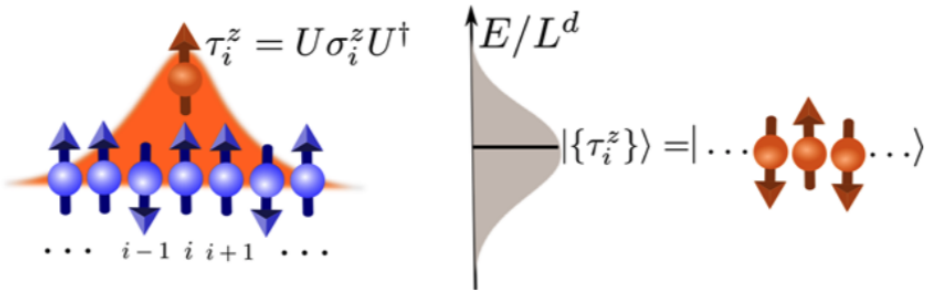

Figure 5.2.: In the MBL phase, there exists an extensive number of quasi-local integrals of motion (LIOMs), namely τ_i^z. Each τ_i^z is a Pauli operator, obtained through a quasi-local unitary transformation U from the physical spins: $\tau_i^z = US_i^zU^\dagger$ (left panel). The support of τ_i^z decays exponentially with distance from site i (right panel). The τ_i^z's commute with the system Hamiltonian and among each other. Thus, the eigenstates are completely specified by the full set of quantum numbers associated with the τ_i^z. Picture extracted from [197].

The lack of ergodicity in the deep MBL phase has been linked to the existence of an extensive number of local integrals of motion (LIOMs) [166, 167, 190, 219–224]. A physical interpretation of the LIOMs can be easily kept considering the XXZ model:

$$H_{\mathrm{XXZ}} = \sum_{i=1}^{L-1}\left[\frac{J}{2}(S_i^+S_{i+1}^- + \mathrm{h.c.}) + VS_i^zS_{i+1}^z\right] + \sum_{i=1}^{L}\Delta_i S_i^z. \tag{5.2}$$

When $J = 0$, the system is "classical" and trivially localized, i.e. the spin operators S_i^z are conserved quantities, $[S_i^z, H] = 0$, and the eigenstates are simply product states of the form: $|E_\alpha^0\rangle = |\uparrow\uparrow\downarrow \ldots\rangle$. Therefore, the onsite operators S_i^z constitute a complete set of mutually commuting, strictly local integrals of motion. Turning on a small hopping amplitude $J > 0$, we expect the "classical" eigenstates to be weakly perturbed. In particular, the new eigenstate $|E_\alpha\rangle$ should be related to $|E_\alpha^0\rangle$ by a quasi-local unitary transformation U which creates spin flips only between nearby spins. This quasi-local unitary transformation has been explicitly constructed [193, 220]. It has been found that it defines a new set of integrals of motion:

$$\tau_i^z = US_i^zU^\dagger, \tag{5.3}$$

verifying $[\tau_i^z, H] = [\tau_i^z, \tau_j^z] = 0$. Notice that, in principle, the operators τ_i^z can be constructed for any quantum system. However, in MBL systems, τ_i^z are *quasi-local* operators, as their support decays exponentially with distance from site i. A pictorial representation of them is illustrated in Fig. 5.2. The decay length of the τ_i^z is typically indicated as ξ. Interestingly, in recent years it has become clear that MBL systems are characterized by many and diverse length scales, besides ξ (see Refs. [223, 224]). By the LIOMs, one can construct a phenomenological model for MBL systems known as the l-bit model, given by:

$$H_{l\text{-bit}}^{\mathrm{full}} = \sum_{i=1}^{L} h_i\tau_i^z + \sum_{i,j=1}^{L} J_{ij}\tau_i^z\tau_j^z + \sum_{n=1}^{\infty} K_{i\{k\}j}^{(n)}\tau_i^z\tau_{k_1}^z\ldots\tau_{k_n}^z\tau_j^z \tag{5.4}$$

The interactions J_{ij}, $K_{i\{k\}j}^{(n)}$ can be equivalently positive or negative; their absolute value fall off exponentially with distance, as do their probabilities of being large.

One of the fingerprints of the MBL phase is the absence of DC spin transport and energy transport in the system, similarly to single-particle localization. The absence of diffusive

transport is however not an exclusive feature of the MBL phase: sub-diffusive transport properties have been observed in the delocalized phase as well [225–229]. Other fingerprints of the MBL phase are the slow spreading of the entanglement after a quantum quench, the slow decay of correlation functions, and the area-law entanglement for eigenstates [190, 198, 230–235]. All these features are captured by the l-bit model. For instance, the slow, and logarithmic growth in time of the entanglement can be easily understood in terms of dephasing processes among the LIOMs, which are pictorially illustrated in Fig. 5.3.

The presence of interactions in MBL systems causes the spreading of entanglement, which is indeed absent in single-particle localized systems. From Eq. (5.4), we see that two l-bits i, j get entangled only by their direct interaction and not through a mutual interaction with a third l-bit k. The interaction of i with j depends only on the value of τ_j^z, which is a constant of motion and is not affected by any other l-bit. The effective interaction between i, j is given by $J_{ij}^{\text{eff}} = J_{ij} + \sum_{n=1}^{\infty} K_{i\{k\}j}^{(n)} \tau_{k_1}^z \tau_{k_n}^z$, which is expected to fall off exponentially with the distance L between i and j: $J^{\text{eff}} \sim J_0\, e^{-L/\kappa}$. Therefore, assuming that i, j are non-interacting at initial time $t = 0$, they will be entangled for times such that $J^{\text{eff}} t \geq 1$. Thus, after a time t, all l-bits within a distance $L \sim \kappa \ln(J_0 t)$ will be entangled. Since the entanglement entropy is proportional to the number of entangled degrees of freedom, this explains the observed logarithmic growth. Similar reasoning implies that the expectation value of local operators with finite support decays as a power-law in time [233], and that through standard spin-echo protocols one can recover the state of a given l-bit τ_i^z [236]. This phenomenology is in stark contrast with thermalizing systems, where the presence of the spin flips in the Hamiltonian determines the possibility for two spins to interact indirectly through a third spin, making the entanglement spreading ballistic in time [237].

In the following Chapters, we will also focus on the time and space behavior of the concurrence [238–241], which has been used to characterize entanglement in MBL systems before [242], and which can be measured experimentally [243, 244]. The concurrence quantifies the distance of the two-site reduced density matrix ρ_{ij} from the manifold of mixed, separable states whose reduced density matrix can be written as $\rho = \sum_a p_a \rho_a^{sep}$, where ρ_a^{sep} are separable, $p_a \geq 0$, and $\sum_a p_a = 1$. This implies that, if $C_{ij} > 0$, there is no mixture of separable states that can account for the correlations between sites i and j. For two spins $1/2$, it can be shown [241] that

$$C_{ij} = \max\{0,\, \lambda_1 - \lambda_2 - \lambda_3 - \lambda_4\}, \tag{5.5}$$

where λ_a^2 are the eigenvalues of the matrix $R_{ij} = \rho_{ij}(\sigma_y \otimes \sigma_y)\rho_{ij}^*(\sigma_y \otimes \sigma_y)$ sorted in descending order, and the complex conjugation is done in the standard computational basis. Its particular definition allows the concurrence to discriminate between quantum entanglement and thermal entropy. Thus, it spots quantum entanglement between two spins even if they are thermal, i.e. also entangled with a heat bath. For this reason, we will employ the concurrence as a well-defined entanglement measure in Chapter 6, where we study the quantum dynamics of two-level systems in the presence of dissipation. It is known that the mean value of the concurrence decays in time as a power law in MBL systems, while in Anderson localized systems it tends to a plateau, and in ergodic systems it vanishes exponentially [242]. Thus, the concurrence appears to be a promising quantity to perform a first direct experimental observation of many-body dephasing processes in the MBL phase. In Chapter 8, we will also show that the concurrence can be employed to explore the spatio-temporal heterogeneities of entanglement deep in the MBL phase.

MBL systems are the prototypical example of quantum systems that avoid going to thermal equilibrium. Nevertheless, analogous phenomena have been observed in driven periodic sys-

Figure 5.3.: During the time evolution, the z component of the l-bits is conserved. However, the l-bits precess about the z-axis with a rate determined by all the other spins. Picture extracted from [162].

tems (time crystals) [245–248], and in systems without disorder [202, 249–256]. It is now clear that disorder and frustration are not necessary for the presence of localization and the breakdown of ergodicity in quantum systems. Indeed, many-body localization is a fully quantum phenomenon, and it relies on the discreteness of the energy spectrum and interference effects [197]. The key ingredient for the existence of the MBL phase is that the transition rate between two many-body configurations close in energy is much smaller than their energy gap; this results in the absence of resonances between the two. This situation might be favored by disorder, whose presence is however not needed. Recently, a growing body of literature has investigated the impact of dissipation and dephasing on MBL systems [257–265]. The research question underlying these works concerns how the imperfect isolation from the environment enters the experimental measurements on MBL systems. The presence of an arbitrarily weak coupling to a thermal bath unavoidably leads to thermalization. Indeed, it spoils interference effects and leads to delocalization. However, it has been found that at intermediate and long time scales the relaxation dynamics of MBL systems coupled to heat baths shows clear signatures of the localized phase and differs from that of ergodic systems.

The impossibility of having an infinitely long-lived many-body localized phase in the presence of a heat bath is in stark contrast with the nature of the glassy phase. As already emphasized in Chapter 1, the common denominator of glassy systems is the presence of a rugged energy landscape, which is due to the presence of disorder and frustration. Such landscape is present in both classical and quantum glasses. As far as the temperature of the heat bath is not sufficient to cross the energy barriers of the landscape, the glassy phase cannot be spoiled. Moreover, it is the very coupling to the thermal bath and the thermal fluctuations that allow classical glasses to exhibit their peculiar dynamical features, such as the two-step relaxation and aging effects. Therefore, the glass and the many-body localization transitions in quantum systems are two separate phenomena [201]. Nonetheless, this second Part of the thesis will show the presence of a deep connection between glasses and MBL systems.

6. Two-level systems in glasses: The Gorini-Kossakowski-Sudarshan-Lindblad master equation

In this Chapter, we discuss the quantum dynamics of an ensemble of two-level systems (TLSs) weakly coupled to phonons. We define the TLS model in Section 6.1. In Section 6.2, we introduce the Gorini-Kossakowski-Sudarshan-Lindblad master equation for the TLS density matrix and present the explicit form of the TLS–TLS interactions and dissipation terms, sketching the dynamical phase diagram of the model. Section 6.3 contains the numerical results on the real-time evolution of the TLSs. In particular, in Section 6.3.3 we consider the system as artificially isolated, and we analyze the signatures of localization on the entanglement quantifiers. In Section 6.3.4, we reintroduce the dissipative terms and show how they affect the results. The reference article for this Chapter is Ref. [266].

As discussed in Chapter 1, a series of classic experiments [31, 43] has made manifest that the properties of glasses at temperatures of 1 K and below show a surprising degree of universality and deviate significantly from Debye theory. Several theoretical ideas aimed at explaining these results, mostly on the lines of two seminal works [34, 35]. There, the authors introduced the idea of bi-stable tunneling systems (or two-level systems, TLSs), whose parameters (energy difference and tunneling amplitude) are very broadly distributed. With an appropriate choice of such distributions, one can reproduce quantitatively the values of several equilibrium quantities, including specific heat, thermal conductivity, and sound attenuation. The range of TLS models has been expanded considerably beyond the original works to account for various experimental facts [33, 48], and even criticized as a glorified curve-fitting procedure [36, 53–55].

In a glass, TLSs interact with phonons and, if they have an electric dipole moment, also with photons. The consequence of the interaction between TLSs and the phonon (or photon) bath is twofold: it generates TLS–TLS interactions, which have been observed in several experiments [37, 56, 67, 69, 71, 72], and it is responsible for the equilibration of the TLSs at the bath temperature. The purpose of this Chapter is to present the first direct investigation of the quantum dynamics of TLSs coupled to phonons and to discuss in particular how, and on which time scales they reach thermal equilibrium. We idealize the system TLSs + phonons as an isolated system, and we analytically derive the Gorini-Kossakowski-Sudarshan-Lindblad (GKSL) master equation for the reduced density matrix of the TLSs, tracing out the phonons. We find that the TLS unitary evolution (the so-called Liouvillian) is governed by a Hamiltonian with an extensive number of local conserved quantities, resembling the effective Hamiltonian of many-body localized (MBL) systems; the dissipative term (the so-called Lindbladian) destroys localization and drives the system to a thermal state. We show that, considering the typical values of the TLS disorder parameters, dissipation is much slower than any other time scale of the problem, and the TLS relaxation dynamics shows the fingerprint of localization for a long time window, even in the presence of dissipation. This is in line with recent

findings on the effects of dissipative baths on many-body localized systems: in the presence of a bath, the system dynamics can keep showing the signatures of localization at short and intermediate time scales, before reaching a thermal state [257–265] (see also Chapter 5).

We focus in particular on the creation and spreading of entanglement as measured by the concurrence (see Chapter 5), and the entanglement entropy. The former measures the amount of entanglement between two TLSs; starting the time evolution from a product state, it grows to a maximum, and then decays and vanishes. The latter instead increases monotonically with time to reach a thermodynamic value. We simulate both the artificially isolated TLS system, i.e. we set the dissipation strength to zero, and the open system. For the artificially isolated system, we can confidently investigate the thermodynamic limit, since our numerics goes up to $N = 60$ TLSs. We observe that, for long time scales, the concurrence decays as a power law $C \sim t^{-\beta_i}$, down to a plateau value which is exponentially small in the number of TLSs. This slow power-law decay is the signature of localization and contrasts with the exponentially fast decay one would observe for an ergodic system. In the open system, we find that the concurrence always vanishes, never reaching the plateau observed in the unitary case. This is not surprising, since the phonon (or photon) bath to which TLSs are coupled is effectively infinite, and entanglement can spread indefinitely. For not too large dissipation, we find that the concurrence decays as a power law $C \sim t^{-\beta_o}$, as in the artificially isolated system, indicating that the signatures of TLS localization are observable even in this case for long time windows. The exponents $\beta_{i,o}$ in the two scenarios are of the same order of magnitude. Their comparison shows that, within the statistical errors and finite-size corrections, β increases in the presence of dissipation.

The results presented in this Chapter point out that assuming ergodicity when discussing the TLS physics might not be justified for all kinds of experiments on ultra-low temperature glasses. The signatures of many-body localization might be experimentally accessible in real glassy samples at ultra-low temperatures, for instance using ultra-fast laser probes, or techniques similar to the ones employed in Ref. [267]. The observed quantum dynamics should be robust from material to material, and against the uncertainty in the characterization of the disorder distributions. Therefore, glasses might be a privileged platform to investigate many-body localization in real materials.

6.1. Definition of the TLS model

We define the total Hamiltonian of the TLSs system and the thermal bath as [41, 48, 73, 74]

$$H = H_{TLS} + H_{ph} + H_{int}. \tag{6.1}$$

The TLS Hamiltonian, discussed in Chapter 1, is given by

$$H_{TLS} = \sum_i (\varepsilon_i \sigma_i^z + \Delta_i \sigma_i^x). \tag{6.2}$$

We employ Pauli spins to represent the two states of a TLS; ε_i is the asymmetry energy and Δ_i the tunnelling amplitude in the i-th double well. According to the original works [34, 35], we consider ε as drawn from a uniform distribution of width $W \approx 0.1$ eV:

$$p_\varepsilon(\varepsilon) = \frac{1}{W}\Theta(W - \varepsilon)\Theta(\varepsilon) \tag{6.3}$$

(Θ is the Heaviside step function). In [34, 35] it is also argued that the tunnelling amplitudes Δ_i are broadly distributed, and that the most reasonable distribution, from a simplicity standpoint, is log-uniform:

$$p_\Delta(\Delta) = \frac{\Theta(\Delta - \Delta_{min})\Theta(\Delta_{max} - \Delta)}{\log(\Delta_{max}/\Delta_{min})\Delta} \tag{6.4}$$

where

$$\Delta_{min} = \overline{\Delta} \cdot 10^{-n_\Delta/2}, \qquad \Delta_{max} = \overline{\Delta} \cdot 10^{n_\Delta/2}. \tag{6.5}$$

The parameter n_Δ defines the span of the distribution: $\Delta_{max}/\Delta_{min} = 10^{n_\Delta}$. Since $\langle \log \Delta \rangle = \log \overline{\Delta}$, we note that $\overline{\Delta}$ is the typical value. Usually in the literature, $n_\Delta \simeq 8$ and $\overline{\Delta}/W \approx 10^{-5}$, making $p_\Delta(\Delta)$ very wide. That Δ should have such a wide distribution can be grasped at a semiclassical level: by the WKB approximation $\Delta \sim \exp(-\sqrt{2mV}\delta x/\hbar)$ [33], where m,V and δx are respectively the mass, potential barrier and displacement in some generalized coordinate, parametrizing the potential well that defines a TLS. Thus, even small fluctuations of m, V_0 or δx are strongly amplified at the level of Δ.

The phonon bath is described by

$$H_{ph} = \sum_k \hbar\omega_k b_k^\dagger b_k \tag{6.6}$$

b_k (resp. $b_k^\dagger$) being the annihilation (resp. creation) operator of a phonon with wavevector and polarization $k = (\mathbf{q}, s)$. The dispersion relation in amorphous solids is, to a good approximation at low temperatures [268], $\omega_{\mathbf{q}s} \simeq v_s q$. Typically $v_L \simeq 1.6\, v_T$ (see Table 6.1). However, since their difference is not crucial for the quantities of interest (see Appendix B.1), it is convenient to define the average velocity v as $\frac{1}{v^3} := \frac{1}{3}\sum_s \frac{1}{v_s^3}$.

The interaction Hamiltonian of the localized degrees of freedom with the strain field is, to lowest order [41, 73, 74],

$$H_{int} = \sum_{ik} \sigma_i^z \left(\xi_{ik} b_k + \text{h.c.}\right), \tag{6.7}$$

with

$$\xi_{ik} = -i\sqrt{\frac{\hbar}{2V\rho\,\omega_k}}\gamma_i D_i^{ab} e_k^{ab} e^{i\mathbf{q}\cdot\mathbf{r}_i}. \tag{6.8}$$

Above, ρ is the material density, V the volume, $\gamma_i D_i^{ab}$ the elastic dipole tensor of the i-th TLS (the strength γ_i has the dimension of an energy and D_i^{ab} is dimensionless), and $e_k^{ab} := \frac{1}{2}\left(q^a \hat{e}^b_{\mathbf{q}s} + q^b \hat{e}^a_{\mathbf{q}s}\right)$ ($\mathbf{q}$ is the wavevector and $\hat{\mathbf{e}}_{\mathbf{q}s}$ the unit $(\mathbf{q}, s)$-polarization vector). γ_i and D_i^{ab} are random variables; their probability distributions are induced by the distributions of the shapes and directions of the TLSs in space. In the literature [33, 48], it is argued that γ_i should be of the same order of magnitude of W, since the former is related to the energy shift induced in a TLS by a phonon, and it must be comparable with the energy imbalance of the two minima in the double well. Therefore, for simplicity, we set $\gamma_i \equiv W$ and absorb in the dipole entries D_i^{ab} all the disorder fluctuations: we consider D_i^{ab} to be random variables of order 1. We will not specify the full distribution of their entries, since in Sec. 6.2.3 we will show that only some combinations are needed. We refer to those Sections for more details.

In Table 6.1, we report the experimental values of the TLS model parameters for three well-known structural glasses.

	SiO_2	BK7	PMMA
W [meV]	130	70	30
Δ_{max} [meV]	13	7	3
$\overline{\Delta}$ [meV]	10^{-3}	10^{-3}	10^{-4}
Δ_{min} [meV]	10^{-7}	10^{-7}	10^{-8}
γ [eV]	0.8	0.7	0.3
v_L [km/s]	5.8	6.2	3.2
v_T [km/s]	3.8	3.8	1.6
ρ [g/cm^3]	2.2	2.5	1.2
$k_B T_D$ [meV]	30	30	10
ρ_{TLS} [nm^{-3}]	0.3	0.2	0.05
$\hbar\tau^{-1}$ [meV]	1.8	1.7	0.45

Table 6.1.: Summary of the TLS model parameters for fused quartz (SiO_2), borosilicate glass (BK7), and plexiglass (PMMA). The parameters v_L, v_T, ρ and the Debye temperature T_D are independent; their values are derived from experimental measurements [41, 269]. The (average) TLS-phonon coupling γ is experimentally accessible too [269]. One can reasonably assume $W \approx k_B T_{glass}$: indeed the TLSs are formed at the glass transition [33]. As a consequence, one should also set $\Delta_{max} \approx 10^{-1} W$ in order to have a density of states that goes to zero above W [34], and $\Delta_{min} \approx 10^{-9} W$ to reproduce instead a flat DOS at low temperatures [270]. The precise value of Δ_{max} and Δ_{min} is not crucial, since they enter only logarithmically in the quantities of interest. One can obtain the numerical density of the TLSs, ρ_{TLS}, from the experimentally measurable parameter $\bar{P} = \rho_{TLS}/W \log(\Delta_{max}/\Delta_{min})$ [33, 269].

6.2. The GKSL master equation

To study the dynamics of the TLSs, we need to integrate out the phonons. In this Chapter, we will work in the GKSL framework [271, 272]. The GKSL master equation aims at describing the dynamics of open quantum systems which cannot, in general, be represented in terms of unitary time evolution. The GKSL master equation is often indicated in the literature as the Lindblad master equation. However, this is fairly not accurate, since this equation has been introduced, independently, by V. Gorini, A. Kossakowski, and G. Sudarshan in an article published in May 1976 [273], and by G. Lindblad in an article published in June 1976 [274]. Both papers can be considered among the most influential in theoretical physics. Indeed, the attention to open quantum systems has seen a great rise in recent years with the advent of the quantum era, since fields as quantum information and quantum technologies have become crucial for the applications of quantum mechanics. An interesting discussion on the history of the GKSL master can be found in Ref. [275].

6.2.1. The GKSL master equation for TLSs

The GKSL master equation relies on some approximations [271, 272]. First, one assumes weak coupling between TLSs and phonons. This assumption is usually taken in the literature [33]; its validity has to be checked a posteriori, verifying that the energy scales of decoherence and dissipation induced by phonons are smaller than the TLS energy set by W. The GKSL framework consists of three further approximations: the Born, the Markov, and the

rotating-wave approximation. In the Born approximation, one assumes that at all times the influence of the TLSs on the phonon thermal population is negligible. This is a consequence of weak coupling, and of the TLSs being a dilute system in the (amorphous) lattice. Therefore, we expect the Born approximation to be valid to a good extent for TLS systems. The Markov approximation instead entails that all the bath excitations decay on very fast time scales with respect to those of the TLSs. This is not guaranteed when working at ultra-low temperatures, but it is still a good starting point. Finally, the rotating-wave approximation assumes that, when considering two TLSs, the *resonant* processes are dominant, or equivalently that the relaxation time of TLSs in the open-system, τ_R, is long with respect to the time scale of the intrinsic evolution of the system [271]; in formulas: $\tau_R \gg |\nu_i - \nu_j|^{-1}$. We will validate a posteriori this assumption in Sec. 6.2.4.

The GKSL master equation for the (reduced) density matrix of the TLSs ρ reads:

$$\partial_t \rho(t) = -\frac{i}{\hbar}[H_{TLS} + H_{LS}, \rho(t)] + \sum_\kappa \mathcal{L}_\kappa \rho(t). \tag{6.9}$$

The first term on the right-hand side (r.h.s.) describes the unitary evolution of the system, and it is called the Liouvillian. It is governed by H_{TLS}, which is the TLS Hamiltonian of Eq. (6.2), and H_{LS}, which is the Lamb-Stark shift Hamiltonian (it will be specified below in Eq. (6.16)). We will see that, within the GKSL assumptions, the TLS–TLS interactions in H_{LS} commute with the isolated TLS Hamiltonian: $[H_{TLS}, H_{LS}] = 0$, ultimately leading to the MBL character of the unitary dynamics. The second term on the r.h.s., the so-called Lindbladian, describes instead dissipation and decoherence. $\mathcal{L}_\kappa$ are the Lindblad super-operators; in general, the label κ can assume $O(N^2)$ values but, as we will show in the following, in our system the dominant terms are on-site, reducing $\kappa \equiv i = 1, 2, \ldots, N$.

In Chapter 7, we will go beyond the GKSL master equation; in particular, we will assume that TLSs and phonons are strongly coupled. We will see, however, that this second route finally leads to the same physical results as the present one, strengthening further the present findings.

6.2.2. The free TLS eigenoperators

To compute the Lamb-Stark shift Hamiltonian H_{LS} and the Lindblad super-operators $\mathcal{L}_\kappa$ appearing in Eq. 6.9, it is convenient to diagonalize the free TLS Hamiltonian H_{TLS} [271, 272]. We look for single-site operators S_i such that

$$[H_{TLS}, S_i] = -\hbar\nu S_i. \tag{6.10}$$

This linear problem can be easily solved, finding the eigenvalues

$$\hbar\nu_{i,0} = 0, \qquad \hbar\nu_{i,\pm} = \pm\hbar\nu_i = \pm 2\sqrt{\varepsilon_i^2 + \Delta_i^2}, \tag{6.11}$$

with corresponding eigenoperators

$$S_i^z = \vec{v}_{i,0} \cdot \vec{\sigma}_i, \qquad S_i^\pm = \vec{v}_{i,\pm} \cdot \vec{\sigma}_i, \tag{6.12}$$

where

$$\vec{v}_{i,0} = -\frac{2}{\hbar\nu_i}(\Delta_i, 0, \varepsilon_i), \quad \vec{v}_{i,\pm} = \frac{2}{\hbar\nu_i}(-\varepsilon_i, \pm i\hbar\nu_i/2, \Delta_i). \tag{6.13}$$

Notice that, since typically $\Delta_i \ll \varepsilon_i \sim W$, $\hbar\nu_i$ will be of order W. Also, defining $S_i^x = (S_i^+ + S_i^-)/2$ and $S_i^y = (S_i^+ - S_i^-)/2i$, the operators S_i^x, S_i^y, S_i^z form a Pauli basis.

At this point, it is easy to verify that the TLS Hamiltonian reads

$$H_{TLS} = -\frac{1}{2}\sum_i \hbar\nu_i S_i^z. \tag{6.14}$$

6.2.3. Coupling to phonons

The coupling with phonons induces both dissipation and TLS–TLS interactions. Under the assumptions discussed in Sec. 6.2.1, they can be modeled via the GKSL master equation, whose final form is

$$\begin{aligned}\partial_t\rho(t) = -\frac{i}{\hbar}\Bigg[-\frac{1}{2}\sum_i \hbar\nu_i S_i^z + \sum_{ij} J_{ij} S_i^z S_j^z, \rho(t)\Bigg] \\ + \sum_i Y_i f_T(\hbar\nu_i)\Big(S_i^+\rho(t)S_i^- + S_i^-\rho(t)S_i^+ - 4\rho(t)\Big) \\ + \sum_i Y_i\Big(S_i^+\rho(t)S_i^- + \{\rho(t), S_i^z\} - 2\rho(t)\Big).\end{aligned} \tag{6.15}$$

In the previous equation, the first term on the r.h.s. corresponds to the commutator $-\frac{i}{\hbar}[H_{TLS}+H_{LS},\rho(t)]$ in Eq. (6.9), where

$$H_{LS} = \sum_{ij} J_{ij} S_i^z S_j^z \tag{6.16}$$

is the Lamb-Stark shift Hamiltonian. The second term on the r.h.s. contains the dissipative terms; it is written separating explicitly the temperature dependent and independent contributions: $f_T(\epsilon) := (e^{\epsilon/k_B T} - 1)^{-1}$ is the Bose-Einstein distribution function at temperature T. Considering that $\hbar\nu_i \sim W \approx 0.1$ eV, at ultra-low temperature ($T \sim 1$ K and below) $f_T \simeq 0$, and our system is effectively at *zero temperature*. Thus, in the following we will keep only the temperature-independent contributions.

Before introducing the analytical expressions for Y_i and J_{ij}, a few comments are in order. As depicted in Fig. 6.1, in general interactions can take place either in the S^z–S^z channel (panel (a)), or by flipping two spins with the emission and absorption of a virtual phonon (panel (b)). This latter case, for our system, can be neglected: since ν_i and ν_j are random variables, the matching condition $\omega = \nu_i = \nu_j$ (ω is the phonon frequency), entailed by the rotating-wave approximation, is a rare event. Even accounting for those rare interactions, e.g. in the S^x–S^x channel, the picture is not modified. Indeed, terms of the form $K_{ij}S_i^xS_j^x$ will still decay with the distance r_{ij}: the probability of having a resonant ij couple that is *also close in real space* is vanishingly small. Therefore, the MBL-breaking effect of $S_i^xS_j^x$ terms [276–278] is negligible in comparison to the Lindblad dissipator, and the Lamb-Stark shifts can be safely considered diagonal in S^z. Moreover, the Lindblad superoperators of Eq. (6.9) correspond only to the decay processes in Fig. 6.1d, since purely dephasing processes (panel (c)) are absent. This is simply because there is no density of states of the phonons at zero frequency.

Having understood what are the physical processes behind the GKSL evolution, we can compute explicitly the dissipation rates Y_i and the interaction strengths J_{ij}. As stated above,

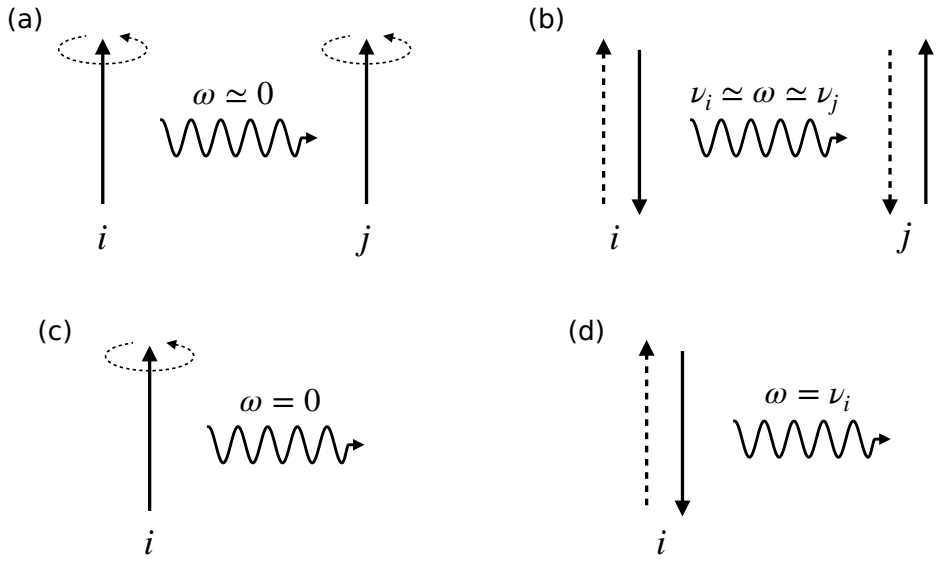

Figure 6.1.: Virtual (a,b) and real (c,d) phonon processes that lead to TLS–TLS interactions and dissipation, respectively. (a) Interactions in the S^z–S^z channel are mediated by phonons of vanishing frequency ω, and take place among each couple ij, yielding H_{LS} of Eq. (6.16). (b) Flip-flop interactions can take place only if the two TLSs resonate: this is a very rare event because the ν_i's are widely distributed random variables. We disregard this possibility altogether throughout this study. (c) Dephasing of a single TLS under the action of the phonon bath. This process is negligible because there are no real phonons at $\omega = 0$. (d) Decay of a TLS into a phonon. Considering that resonating TLSs are very rare and the phonon density of states vanishes at $\omega = 0$, as noted above, it is easy to see that non-unitary processes involving two TLSs can be neglected.

they both come from phonon processes; therefore, one can treat them in a unified way. We start by rewriting the interaction Hamiltonian, Eq. (6.7), as

$$H_{int} = \sum_{ik} \sigma_i^z \left(\xi_{ik}\psi_k + \text{h.}c.\right) =: \sum_i \sigma_i^z E_i : \tag{6.17}$$

E_i are the environment operators that need to be traced out. Then, following [271, 272], we define

$$\Gamma_{ij}^{\omega} := \frac{1}{\hbar^2}\int_0^{\infty} ds\, e^{i\omega s}\, \text{Tr}_B\left[\rho_B^T\, \hat{E}_i^{\dagger}(t)\, \hat{E}_j(t-s)\right] \tag{6.18}$$

with the hat on $\hat{E}_i(t)$ indicating the interaction picture. It then holds

$$Y_i = \left(\frac{\Delta_i}{\hbar\nu_i}\right)^2 \left[\Gamma_{ii}^{\nu_i} + \left(\Gamma_{ii}^{\nu_i}\right)^*\right]\Big|_{T=0}, \tag{6.19}$$

$$J_{ij} = \frac{2\varepsilon_i}{\hbar\nu_i}\frac{2\varepsilon_j}{\hbar\nu_j}\frac{\hbar}{2i}\left[\Gamma_{ij}^0 - \left(\Gamma_{ji}^0\right)^*\right]. \tag{6.20}$$

The prefactors $\Delta_i/\hbar\nu_i$ and $2\varepsilon_i/\hbar\nu_i$ come from the basis rotation in Eq. (6.12).

We leave to Appendix B.1 all the details of the computation of Γ_{ij}^{ω}, which is rather straight-

forward, while we present here the results obtained:

$$Y_i = \frac{\Delta_i^2 \gamma_i^2 \nu_i \mathrm{Tr}(D_i^2)}{12\pi\rho\hbar^3 v^5}, \tag{6.21}$$

$$J_{ij} = \frac{\gamma_i \varepsilon_i}{\hbar\nu_i} \frac{\gamma_j \varepsilon_j}{\hbar\nu_j} \frac{\mathbb{D}_{ij}}{4\pi\rho v^2 r_{ij}^3}. \tag{6.22}$$

Above, $\mathrm{Tr}(D_i^2) = \sum_{ab} D_i^{ab} D_i^{ba}$, and $\mathbb{D}_{ij}$ is a specific contraction of the dipoles D_i^{ab} and D_j^{cd}, defined in Eq. (B.27).

At this point, we can check a posteriori whether the weak coupling and the rotating-wave approximations are valid. Plugging in Eqs. (6.21) and (6.22) the typical values of the parameters, we find $\hbar Y_i/W \approx 10^{-8}$ and $J_{ij}/W \approx 10^{-3}$. Therefore, even if the coupling constant is comparable or even larger than the on-site energies $\gamma \sim W$, we see that assuming weak coupling is perfectly justified a posteriori. Moreover, as anticipated at the beginning of this Section, the rotating-wave approximation is amply valid too. Indeed, the relaxation time in the open system is much longer than the intrinsic time scale of TLSs: $Y_i^{-1} \gg |\nu_i - \nu_j|^{-1} \sim \hbar W^{-1}$.

6.2.4. Dynamical phase diagram within the GKSL master equation

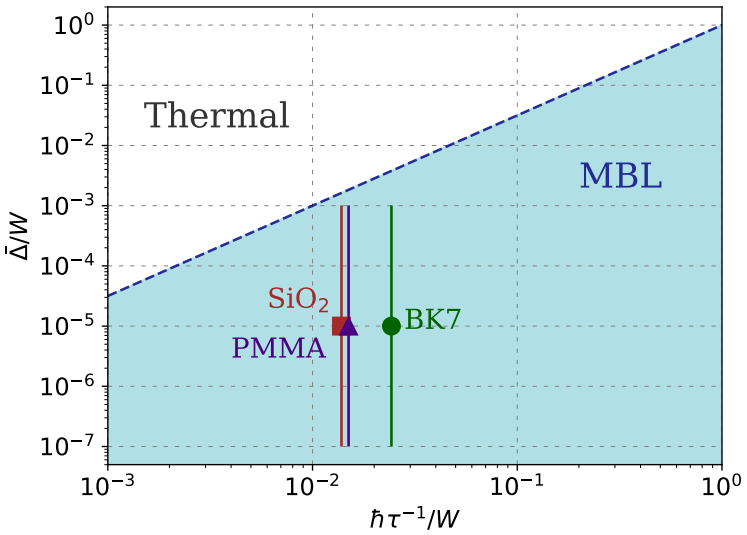

Figure 6.2.: Sketch of the expected phase diagram for TLSs in glasses. From Eq. (6.24) we see that an MBL transient regime can be observed before thermalization takes place if the typical time scales of interaction are short with respect to the dissipation time scales (blue-shaded area). The three glassy materials reported in Table 6.1 lie well within the MBL region, even accounting for the large uncertainties in the parameter $\overline{\Delta}$ (the standard deviation of $\log(\Delta_i)$ is plotted as an errorbar). Thus, the localized regime should be experimentally observable.

The GKSL equation (6.9) constitutes the starting point for exploring the quantum dynamics of the TLSs. As a first thing, we notice that in the absence of dissipation the evolution would be unitary, governed by the Hamiltonian

$$H_{TLS} + H_{LS} = -\frac{1}{2}\sum_i \hbar\nu_i S_i^z + \sum_{ij} J_{ij} S_i^z S_j^z. \tag{6.23}$$

$H_{TLS}+H_{LS}$ is completely expressed in terms of the extensive set of local conserved quantities S_i^z. This is the same property of the effective Hamiltonian of MBL systems, known as the l-bit Hamiltonian, discussed in Chapter 5. Borrowing the terminology from MBL systems, we can refer to the S_i^z's as the l-bits, or local integrals of motion (LIOMs); indeed, they are on-site operators whose values are conserved during the time evolution. Notice that $H_{TLS} + H_{LS}$ presents two main differences with respect to the l-bit Hamiltonian of standard MBL systems (see Chapter 5). First, in the TLS Hamiltonian, the l-bits are formed by *single* spins, not exponentially localized groups of them. Second, the interaction between the TLS decays with distance as a power law, $J_{ij} \propto r_{ij}^{-3}$, rather than exponentially. The effects of this particular form of the interactions on the TLS unitary dynamics are examined in Section 6.3.3.

The diagonal interactions in H_{LS} are responsible for the dephasing of the spins. That is to say, if one artificially turns off the jump operators, i.e. if one sets the dissipation rates $Y_i \equiv 0$, diffusive transport is suppressed but the entanglement spreading persists. The numerical results on this artificially isolated system are presented in Section 6.3.3, and show that the entanglement entropy grows slowly, but indefinitely in time, while the concurrence decays as a power law.

The picture described above is broken by the introduction of the jump operators: dissipative terms in the GKSL equation kill long-time coherence and drive the system to a thermal state. Nevertheless, one can observe an MBL transient regime in the relaxation dynamics, if the time scales of dissipation are appreciably longer than those of interactions. Such competition is quantified by the dimensionless ratio

$$\frac{\hbar Y_i}{J_{ij}} \sim \left(\frac{\overline{\Delta}}{W}\right)^2 \left(\frac{W}{\hbar\tau^{-1}}\right)^3, \tag{6.24}$$

where $\tau = r/v$, r being the typical distance between TLSs and v the speed of sound in the glass. If this ratio is sensibly smaller than 1, the signatures of the localized phase should be observed in the dynamics of the system, and in particular in the spreading of entanglement. In Fig. 6.2, we show a tentative dynamical phase diagram for the TLS system. Recalling that in experiments $\overline{\Delta} \approx 10^{-5}\, W$ while $W \approx 0.1$ eV and, considering $v \approx 5$ km/s and $r \approx 10$ nm, we have $\hbar\tau^{-1} \approx 1$ meV. Thus, the ratio is approximately $\hbar Y/J \approx 10^{-5} \div 10^{-4}$, making dissipation much slower than the interaction part of the unitary dynamics. Even if one allows $\overline{\Delta}$ — the most difficult parameter to infer from experiments — to vary few orders of magnitude, the system will still present an observable MBL transient regime. The dynamical phase diagram of Fig. 6.2 anticipates the features we will observe in the numerical simulations of the real-time dynamics of TLSs, presented in the next Sections: TLS dynamics present a long, albeit transient, localized regime. This result is of primary importance from the experimental viewpoint: glasses at ultra-low temperatures should present the signatures of a localized regime at short and intermediate time scales.

6.3. Numerical results

This Section is devoted to the results of the numerical simulations on the real-time evolution of the TLSs. The analysis will be divided into two parts. In Section 6.3.3, the artificially isolated system (i.e. the one evolving only under the unitary dynamics given by the Liouvillian of the GKSL) governed by the Hamiltonian in Eq. (6.23) is considered. In Section 6.3.4, the dissipative terms in the Lindbladian are re-introduced and the full TLS evolution governed by the GKSL master equation Eq. (6.15) is taken into account.

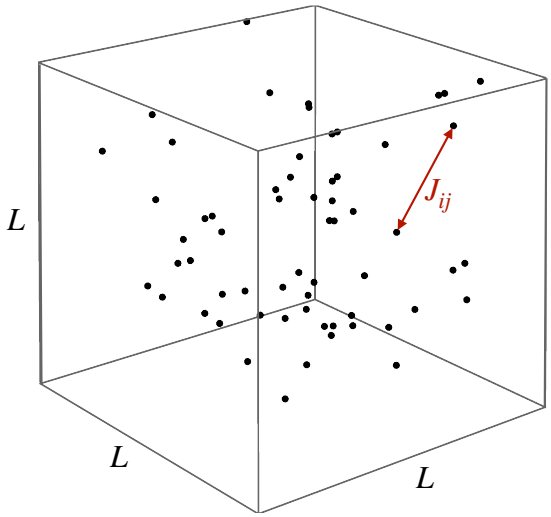

Figure 6.3.: The TLSs are uniformly distributed in a cube of size L, at constant density. The pairwise interactions J_{ij} in Eq. (6.22) are mediated by phonons. These are also responsible for the dissipation in Eq. (6.21). We employ periodic boundary conditions to minimize finite-size effects.

Before going through that, in the next Sections 6.3.1–6.3.2 we briefly discuss the assumptions involved in the numerical simulations and define the dynamical observables we are interested in.

6.3.1. Disorder distributions of the parameters

As we have seen in Chapter 1 and Section 6.1, in the literature the parameters defining the TLS model are drawn from wide probability distributions (see p_ε and p_Δ in Eq. (6.3) and (6.4), respectively). It follows that the competing time scales in the GKSL master equation (namely ν_i^{-1}, $\hbar/J_{ij}$, and Y_i^{-1}) are distributed across several orders of magnitude and, even though their typical values are very different, they overlap one with another. In our numerical simulations, we employ simplified and less broad distributions, arguing that this choice, if properly taken, does not qualitatively alter the physical content and predictions of the model.

We fix $W \equiv 1$, thus setting the (dimensionless) energy scale; $\overline{\Delta}/W = 10^{-1}$, unless otherwise specified, and $n_\Delta = 2$. We also set $\gamma_i \equiv W$, the material density $\rho = 2$ g/cm^3, and the speed of sound $v_{L,T} = 5$ km/s, irrespective of polarization. We consider $\mathrm{Tr}(D_i^2)$ to be the square of a Gaussian random variable of zero average and variance 1, since it must be positive, and $\mathbb{D}_{ij}$ to be a Gaussian random variable of zero average and standard deviation 1, since it can take both signs (see also Appendix B.1). Finally, we consider the TLSs as uniformly distributed in a cube with side L, and compute their distances r_{ij} using periodic boundary conditions. The cube side depends on the number of TLSs as $L = L_0 N^{1/3}$, with $L_0 \simeq \rho_{TLS}^{-1/3}$, so that we keep fixed the TLS number density ρ_{TLS}. For numerical purposes, we fix $L_0 = 1$ nm. See Table 6.1 for a comparison with the experimental values, and Fig. 6.3 for a sketch of the system.

In order to explore the phase diagram obtained in the GKSL framework, and shown in Fig. 6.2, we introduce two further artificial parameters to tune interaction and dissipation

strengths:

$$J_{ij} \to \eta J_{ij}, \qquad Y_i \to \epsilon Y_i. \tag{6.25}$$

In Sec. 6.3.3 we study the artificially isolated system, setting $\eta = 10^5$ and $\epsilon = 0$. In Sec. 6.3.4 we re-introduce the dissipator in the GKSL master equation, and we set $\eta = 10^5$ and $\epsilon = 10^{-6}, 10^{-4}, 1$.

With these choices of the parameters, the on-site frequencies ν_i, the TLS–TLS interactions $\eta J_{ij}/\hbar$ (with $\eta = 10^5$), and the dissipation rates ϵY_i (for $\epsilon = 1$) are of comparable orders of magnitude and are much less widely distributed than originally. The latter feature is particularly useful for numerical purposes, since one can access only small system sizes and, hence, cannot sample well broad distributions. Our results will be discussed in view of these choices.

6.3.2. Initial state and dynamical observables

The initial state of the dynamics is taken as a product state, in which each TLS is represented by a random vector on the Bloch sphere:

$$|\psi(0)\rangle = \bigotimes_{i=1}^{N} \big(\cos(\theta_i/2)|\uparrow\rangle_i + e^{i\phi_i}\sin(\theta_i/2)|\downarrow\rangle_i\big), \tag{6.26}$$

where $\theta_i \in [0, \pi]$ and $\phi_i \in [0, 2\pi)$. Thus, the system is initially at infinite temperature, and we can track precisely the entanglement growth and spreading.

The choice of the appropriate entanglement measure is not obvious: since we are dealing with an open quantum system, we wish to discriminate between quantum entanglement and thermal entropy. A reliable measure of (pairwise) quantum entanglement in open systems is the concurrence C_{ij}, which quantifies the pairwise entanglement between TLSs i and j (see Chapter 5, Eq. (5.5) for the definition of C_{ij}). Here, we consider the average concurrence, defined as

$$C(t) := \frac{1}{N} \sum_{1 \le i < j \le N} C_{ij}(t). \tag{6.27}$$

The normalization factor $1/N$ (instead of the seemingly natural $1/N^2$) is due to the *monogamy of entanglement*: each TLS can be highly entangled only with another TLS, so among the $N(N-1)/2$ terms in the sum, only $O(N)$ will be non-negligible. The concurrence spots entanglement between two spins irrespective of their interplay with other degrees of freedom. For this reason, we employ the concurrence as a well-defined entanglement measure both in the absence (Sec. 6.3.3) and in the presence (Sec. 6.3.4) of dissipation.

It is interesting to compare the time behavior of the concurrence with the half-system entanglement entropy (HSEE)

$$S_E(t) = -\mathrm{Tr}(\rho_A \log \rho_A), \tag{6.28}$$

where ρ_A is the reduced density matrix of the half system A in the bipartition $A|B$. Since the system is three-dimensional, and the TLSs do not fall on a regular lattice, we bipartite the system in the following way. For each TLS, a bubble is constructed around it so that $N/2$ TLSs fall inside and $N/2$ outside the bubble. The entanglement entropy relative to the bipartition is computed as in Eq. (6.28), and then averaged over all such bipartitions. We measure $S_E(t)$ both with and without the dissipator (see Sec. 6.3.3 and 6.3.4, respectively).

6.3.3. Unitary evolution of the TLSs

This Section is entirely devoted to the study of the unitary time evolution of a system of N TLSs governed by the Hamiltonian $H_{TLS} + H_{LS}$ of Eq. (6.23), that we reproduce here for clarity:

$$H_{TLS} + H_{LS} = -\frac{1}{2}\sum_i \hbar\nu_i S_i^z + \sum_{ij} J_{ij} S_i^z S_j^z.$$

As discussed in Section 6.2.4, this Hamiltonian is diagonal in the operators S_i^z, i.e. the values assumed by S_i^z are conserved quantities; therefore, adopting the terminology of MBL systems, we say that $H_{TLS} + H_{LS}$ is in the l-bit form, and S_i^z are LIOMs.

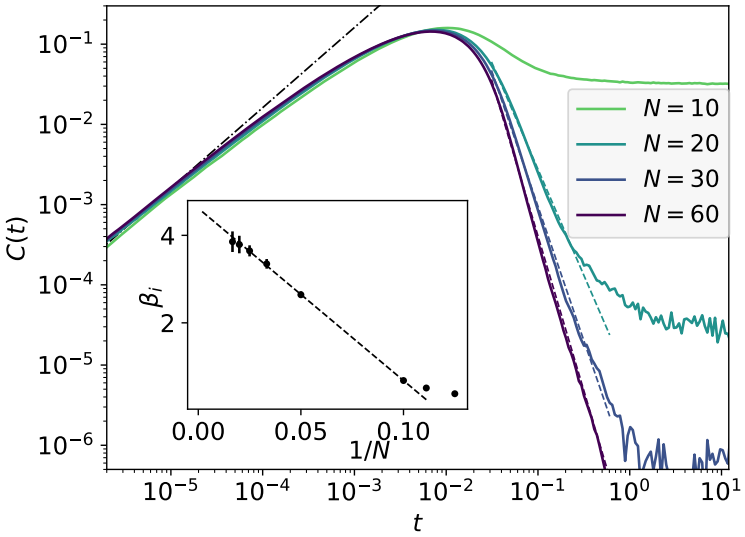

Figure 6.4.: Average concurrence within the unitary dynamics, $\epsilon = 0$ (solid lines). After a linear raise $C \sim t$ (black dashed-dotted line), the average concurrence decays with a power law $C \sim t^{-\beta_i}$ (dashed lines), down to a value which is exponentially small in N. We set $\overline{\Delta} = 0.1$, $\eta = 10^5$; the results are averaged over 5000 disorder realizations. *Inset:* The exponent β_i depends on N and reaches a finite value in the thermodynamic limit. The errors are computed by using the statistical uncertainties of the concurrence values. Not all datasets were shown in the main figure to improve readability.

Studying the dynamics induced only by the Hamiltonian term of the GKSL equation (6.15) is equivalent to set $\epsilon = 0$ (see Eq. (6.25)), i.e. to assume that the time scales of dissipation are much longer than those of interactions: $1/Y_i \gg \hbar/J_{ij}$. In this limit, it is clear that a coherent many-body dynamics can take place before thermal equilibrium is reached. This situation corresponds to the bulk of the MBL phase depicted in the phase diagram of Fig. 6.2. Thanks to the diagonal nature of the Hamiltonian (6.23) and the choice of initial product states, few-sites observables are efficient to compute, as was recognized in previous studies [233, 235, 242]. We refer the interested reader to Appendix B.2 for more details on the computation. Here, we just mention that to compute the concurrence, which is a two-site observable, within the diagonal Hamiltonian (6.23) it is not necessary to perform the time evolution of the whole $2^N \times 2^N$ density matrix, but only to carry out $O(N)$ operations. Therefore, we could easily simulate systems of $N = 60$ TLSs.

The results of the simulations for the unitary evolution are shown in Figs. 6.4, 6.5, and

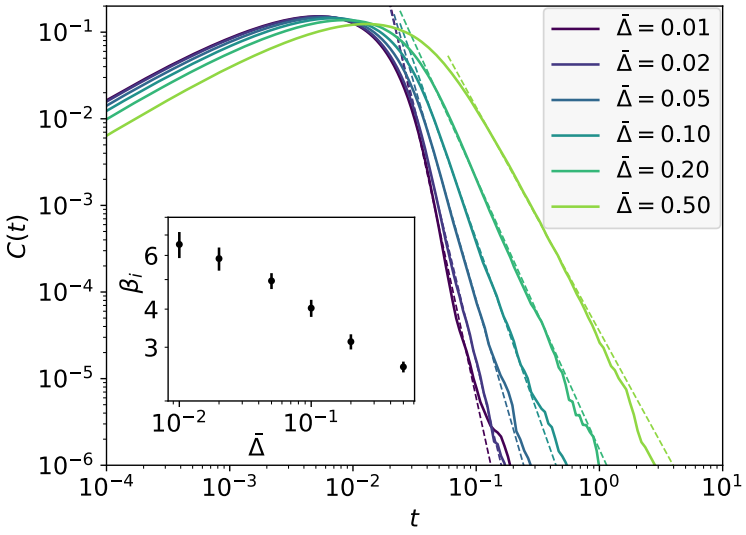

Figure 6.5.: Dependence of the average concurrence decay exponent β_i on $\overline{\Delta}$ in the case of unitary evolution ($\epsilon = 0$). We set $N = 50$, $\eta = 10^5$ and averaged over 5000 disorder realization. We see that the smaller $\overline{\Delta}$, the faster the decay, which remains however compatible with a power law $C(t) \sim t^{-\beta_i}$ (dashed lines).

6.6. One can see that the concurrence $C(t)$, defined in Eq. (6.27), raises linearly from the initial value 0 (the initial state is factorized) to a value independent of N (Fig. 6.4), but slightly dependent on $\overline{\Delta}$ (Fig. 6.5). It then falls off to a plateau via a power-law decay, whose exponent β_i remains finite in the thermodynamic limit (inset of Fig. 6.4), and depends on $\overline{\Delta}$ (inset of Fig. 6.5). Fig. 6.6a shows that the concurrence plateau decays exponentially with the system size: $C(\infty) \propto e^{-\alpha N}$. Finally, from Fig. 6.6b we see that the concurrence reaches its maximum on time scales of order $\hbar/J_{ij}$. In conclusion, the concurrence time behavior can be schematized as

$$C(t) \sim \begin{cases} t & \text{if } t < t_1 \\ t^{-\beta_i} & \text{if } t_1 < t < t_2 \\ e^{-\alpha N} & \text{if } t > t_2, \end{cases} \tag{6.29}$$

where t_1 does not depend significantly on $N, \overline{\Delta}$ but depends parametrically on $\hbar/J_{ij}$, while t_2 grows with N and diverges in the thermodynamic limit.

The decay of the concurrence from its maximum is due to the fact that the interactions J_{ij} make the entanglement spread among many TLSs, as illustrated in Fig. 6.7, while each TLS cannot be highly entangled with more than one other TLS because of the monogamy of the entanglement. The power-law decay of the concurrence from its maximum is in contrast to the behavior of ergodic systems, in which the concurrence vanishes exponentially fast [242]. The slowness of such decay is the fingerprint of the lack of thermalization and of the presence of many-body localization in the artificially isolated TLS system. Slow decays of correlation functions are known [233] to be a feature of MBL dynamics, and the concurrence (albeit not an operator nor a correlation function) follows the same behavior.

We stress again that $H_{TLS} + H_{LS}$, although completely expressed in terms of local integrals of motion, is different from the effective l-bit Hamiltonian of MBL systems, as already pointed out in Section 6.2.4. In particular, the TLS interactions in H_{LS} scale as a power law with distance. Following general arguments [233, 279], one would expect that for long-range

interactions the correlation functions decay in time as stretched exponentials. We cannot exclude that a stretched-exponential behavior would be observed in TLSs if one pushes the dynamics at larger times. In the present study, however, we are only interested in the TLS relaxation dynamics at intermediate time scales since, at long times, dissipation would always bring the system to a thermal state.

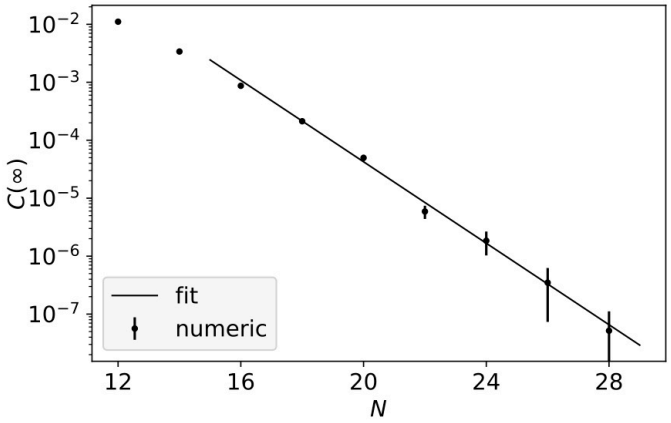

(a)

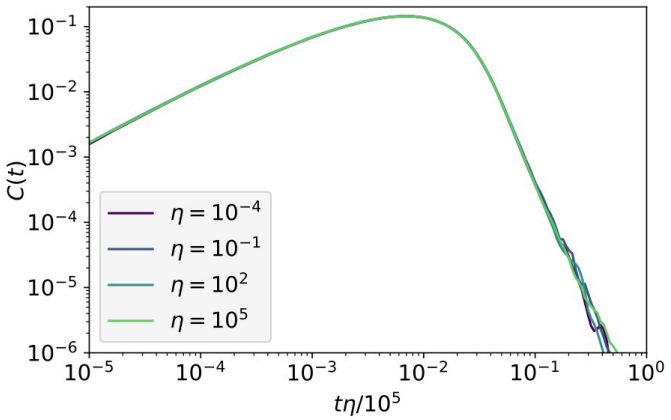

(b)

Figure 6.6.: Results for the unitary dynamics, $\epsilon = 0$. (a) Plateau value of the average concurrence at long times (dots), with errors coming from statistical fluctuations. From a fit (solid line) we find that $C(\infty) \propto e^{-\alpha N}$ with $\alpha \approx 0.8$. This is considerably larger than the value given by the ETH prediction, i.e. a random state, which obeys $C \propto e^{-a2^N}$ with $a \approx 0.127$ (see Appendix B.3). Here $\eta = 10^5$, $\overline{\Delta} = 0.1$, and an average over 10000 disorder realizations was performed. (b) Average concurrence for different interaction strengths η. Rescaling the time as $t \to t\eta/10^5$ (we normalize to $\eta = 10^5$ to compare to the other plots) the curves collapse, showing that the value of η only shifts the timescale but does not modify the shape of the curve $C(t)$. Here $N = 50$, $\overline{\Delta} = 0.1$, and an average over 1000 disorder realizations was performed.

The results on the half-system entanglement entropy (HSEE) are shown in Fig. 6.7, compared with the behavior of $C(t)$. This comparison confirms, as anticipated, that the concurrence starts to decrease when the entanglement spreads and, thus, $S_E(t)$ starts to increase. In addition, Fig. 6.7 shows that $S_E(t)$ grows slowly for a large time window. This slowness is known [230] to be the signature of localization, and shows that TLSs remain coherent

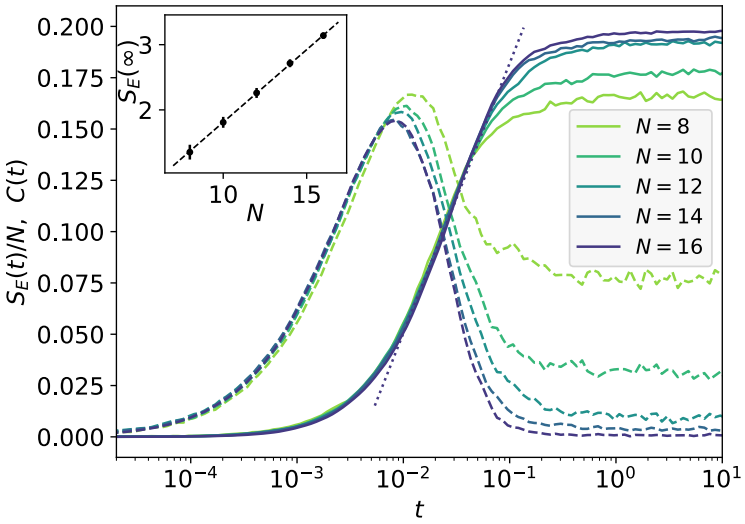

Figure 6.7.: Unitary evolution: half-system entanglement entropy per unit volume $S_E(t)/N$, as defined in Eq. (6.28), for various system sizes (solid lines). We set $\overline{\Delta} = 0.1$, $\eta = 10^5$, and averaged over 1000 disorder realization. The average concurrences $C(t)$ (Eq. (6.27)) are shown as dashed lines for comparison. We see that the concurrence reaches a maximum at short times, as nearby TLSs start to evolve coherently. Then, it starts to decay because the entanglement becomes many-body, as shown by the increase in the HSEE. In this regime, the growth of the HSEE is compatible both with a small power law $S_E(t) \sim t^\alpha$ with $\alpha \sim 1$, as well as $\log(t)$; the dotted line shows $\log(t)$ as a guide for the eye. *Inset:* The HSEE saturates to a volume law, as expected for an MBL system: the phase of each spin depends on all the others. The error bars are computed from the statistical fluctuations of the plateau values.

and non-ergodic during the time-evolution. According to the arguments in [190, 231, 279], we expect that for a long-range, $3d$ system as the TLS one entanglement would grow algebraically in time, $S_E(t) \sim t^\alpha$ with $\alpha \sim 1$. From our data, the entanglement growth is compatible with both a power law with small exponent (~ 1), and a logarithmic growth. In the inset of Fig. 6.7, we see that the asymptotic value of HSEE, $S_E(\infty)$, is proportional to N, indicating a volume law.

6.3.4. Full evolution of the TLSs

This Section is entirely devoted to the study of the time evolution of the TLSs governed by the GKSL master equation (6.15), that we reproduce here for clarity:

$$\partial_t \rho(t) = -\frac{i}{\hbar}\Big[-\frac{1}{2}\sum_i \hbar\nu_i S_i^z + \sum_{ij} J_{ij} S_i^z S_j^z, \rho(t)\Big] + \sum_i Y_i f_T(\hbar\nu_i)\Big(S_i^+\rho(t)S_i^- + S_i^-\rho(t)S_i^+ - 4\rho(t)\Big) + \sum_i Y_i\Big(S_i^+\rho(t)S_i^- + \{\rho(t), S_i^z\} - 2\rho(t)\Big).$$

We set $T = 0$, but $\epsilon \neq 0$ (see Eq. (6.25)), i.e. the system is in the presence of dissipation and decoherence. Increasing ϵ, we increase the typical dissipation rate. For our particular choice of parameters (Sec. 6.3.1), when $\epsilon = 1$, dissipation ultimately becomes comparable with the timescale of the interactions J_{ij}.

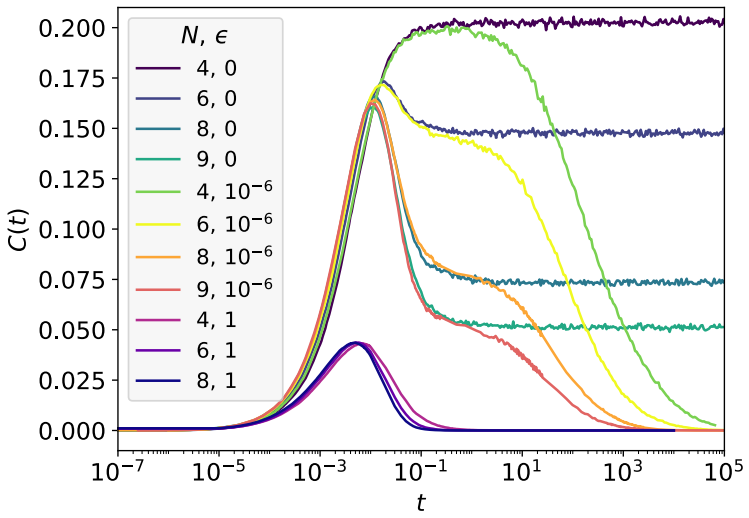

Figure 6.8.: $C(t)$, as defined in Eq. (6.27), for $\epsilon = 0, 10^{-6}, 1$, and different values of N. We see that the presence of dissipation in the GKSL master equation (6.15) decreases the concurrence maximum and moves it at earlier times. We set $\overline{\Delta} = 0.1$, $\eta = 10^5$, and averaged over at least 1000 disorder realizations.

To investigate the time evolution of the system, one has to integrate numerically the GKSL master equation for the TLS density matrix (see Appendix B.4 for more details). Because of the doubling of the Hilbert space dimension, we are forced to small system sizes, up to $N = 9$. In the following analysis, we varied both N (to perform a finite-size scaling) and ϵ. As can be seen from Fig. 6.8, when ϵ is small enough the concurrence $C(t)$ reaches its maximum at the same time as with unitary dynamics ($\epsilon = 0$). Then, it decays from such peak and stabilizes around a finite value dependent on N (cf. Sec. 6.3.3), following the same behavior as in the case $\epsilon = 0$. Ultimately, the dissipation forces $C(t)$ to vanish; $C(t)$ departs from the $\epsilon = 0$ plateau, $C(\infty; \epsilon = 0)$, with a stretched-exponential functional form (Fig. 6.9). We can ascribe this feature to the interaction between TLSs and phonons: when $\epsilon \neq 0$, thanks to the dissipative terms in the GKSL equation (6.15), entanglement can spread among infinitely many phonons, preventing the concurrence from stabilizing around the plateau value.

Furthermore, Fig. 6.8 shows that, increasing the dissipation strength ($\epsilon = 1$), the concurrence maximum becomes smaller and is reached at earlier times. However, the decay from the maximum follows a power-law behavior as in the unitary case, albeit with a different exponent β_o, as reported in Fig. 6.10a. This feature is very important since it shows that the signatures of localization are visible also in the presence of dissipation, if the latter is not too large. The reason at its origin might be linked to the specific (in particular, on-site) form of the dissipation operators in the GKSL equation [258]. The power-law exponent β_o depends on ϵ and N, as shown in Fig. 6.10b, and remains finite in the thermodynamic limit. Due to the small sizes accessible when integrating the full GKSL equation, we expect the extrapolated thermodynamic value of β_o to be underestimated (see Fig. 6.10b, and the results on the unitary case $\epsilon = 0$). Notice that the behavior of the concurrence is determined only by the ratio $\hbar Y_i / J_{ij}$. Remember that, in the unitary case, where the dissipation is absent, changing

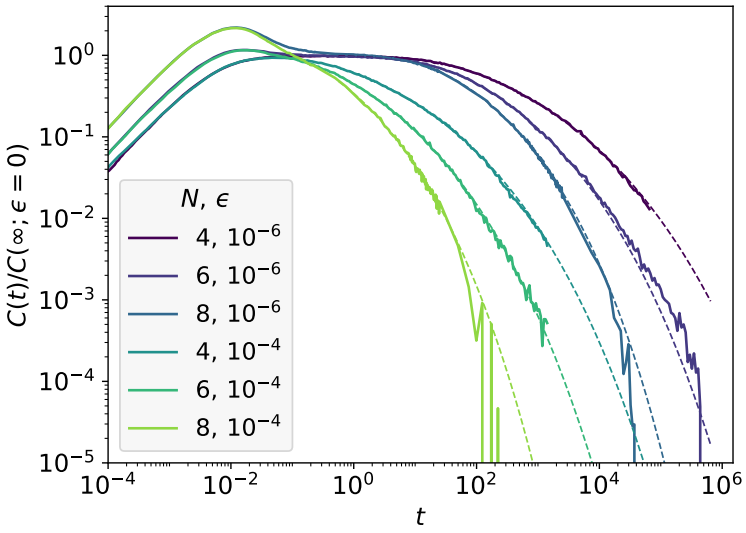

Figure 6.9.: Stretched-exponential fit of the concurrence for $\epsilon = 10^{-6}, 10^{-4}$, normalized to the plateau reached at $\epsilon = 0$: $C(t;\epsilon)/C(\infty;\epsilon = 0)$. Using as fitting function $\alpha \exp\{-(\frac{t+t_0}{\tau})^{\delta}\}$, we obtained $\delta \simeq 0.2$ and $\tau = O(1)$. The plot shows the results for $\overline{\Delta} = 0.1$, $\eta = 10^5$, averaged over at least 1000 disorder realizations.

the typical strength of J_{ij} through the parameter η only shifts the timescale of $C(t)$, without modifying the shape of the curve (see Sec. 6.3.3, Fig. 6.6b). Hence, in this Section, we employ the artificial parameter ϵ to investigate the behavior of pairwise entanglement in the different regions of the phase diagram (Fig. 6.2) by (effectively) changing the ratio $\hbar Y_i/J_{ij}$.

Complementary to the concurrence is the half-system entanglement entropy (HSEE), $S_E(t)$, as defined in Section 6.3.2. Its behavior for various N and ϵ is shown in Fig. 6.11. As in the unitary case, HSEE starts to increase roughly when $C(t)$ reaches its maximum, i.e. when the TLSs start to evolve coherently. It keeps increasing at larger times when entanglement spreads inside the system. From the data at $\epsilon = 10^{-6}$, it can be seen that the entanglement spreading takes place in two steps: first, the TLSs become entangled one with another, and $S_E(t)$ reaches the plateau found with unitary dynamics ($\epsilon = 0$); then, the HSEE increases further due to the dissipative terms in the Lindbladian (6.15). Indeed, for $\epsilon \neq 0$ the TLSs entangle also with the thermal bath.

6.4. Conclusions and outlook

In this Chapter, we investigated the well-known two-level system (TLS) model for glasses at ultra-low temperatures. We studied the quantum dynamics of tunneling TLSs coupled to phonons. Within the framework of the Gorini-Kossakowski-Sudarshan-Lindblad master equation, and by means of a weak-coupling approximation, we computed explicitly the phonon-mediated interactions among TLSs and the dissipation rates.

We found that, as a consequence of disorder, the Hamiltonian responsible for the unitary part of the TLS dynamics, and accounting for TLS–TLS interactions, is completely expressed in terms of local integrals of motion and is thus many-body localized (MBL). Even though it differs from the effective l-bit Hamiltonian of standard MBL systems (see Chapter 5), in

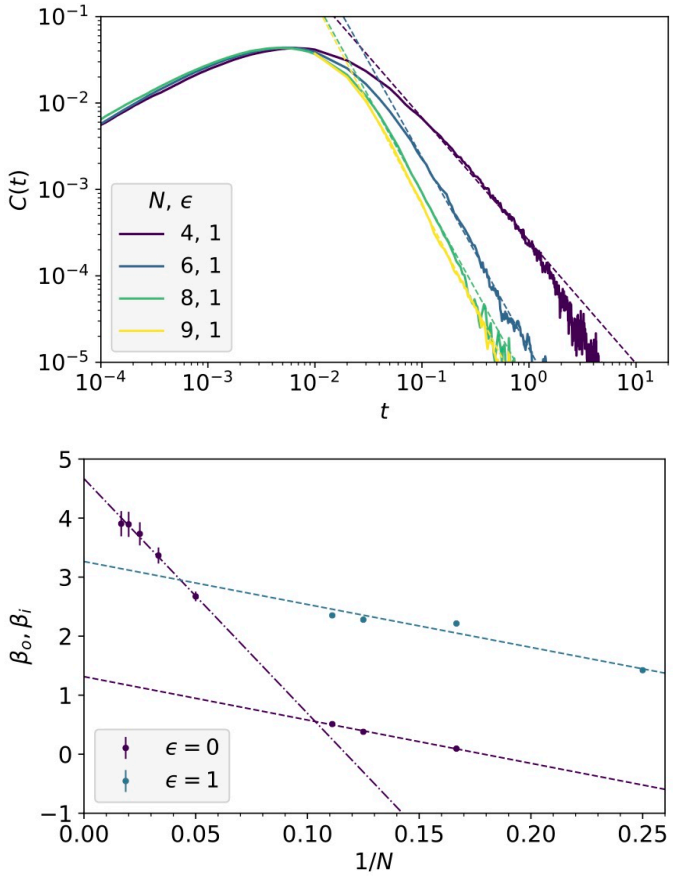

(b)

Figure 6.10.: (a) Power-law fit of $C(t)$ at large times for $\epsilon = 1$. (b) Power-law exponents β_i ($\epsilon = 0$; data from Fig. 6.4) and β_o ($\epsilon = 1$) as a function of $1/N$. We see that the concurrence decays faster as ϵ increases (dashed lines). However, our data can capture the behavior of $C(t)$ in the presence of dissipation only at small N, i.e. in the pre-asymptotic region. We expect the large N behavior to give a larger exponent β_o, as it happens for β_i (dashed-dotted line). We set $\overline{\Delta} = 0.1$, $\eta = 10^5$, and averaged over at least 5000 disorder realizations. The errors are computed by using the statistical uncertainties of the concurrence values.

particular, the TLS–TLS interactions decay as a power law with distance, the TLS relaxation dynamics presents clear signatures of quantum many-body localization. Indeed, simulating the artificially isolated system with unitary dynamics governed by the Liouvillian, we found that the concurrence decays slowly in time as a power law, rather than exponentially fast as it would for an ergodic system. We also observed that the entanglement entropy grows slowly, as in standard MBL systems.

This picture is broken by the presence of dissipation, induced by real processes between TLSs and phonons, which destroy localization and ultimately drive the system to a thermal state. In the open system, for not too large dissipation strength, we find that the concurrence decays as a power law, as in the artificially isolated system, indicating that the signatures of TLS localization are observable even in this case at short and intermediate time scales.

The competition between TLS–TLS interactions and dissipation terms determines the presence of two distinct regions in the dynamical phase diagram of the model: when interactions

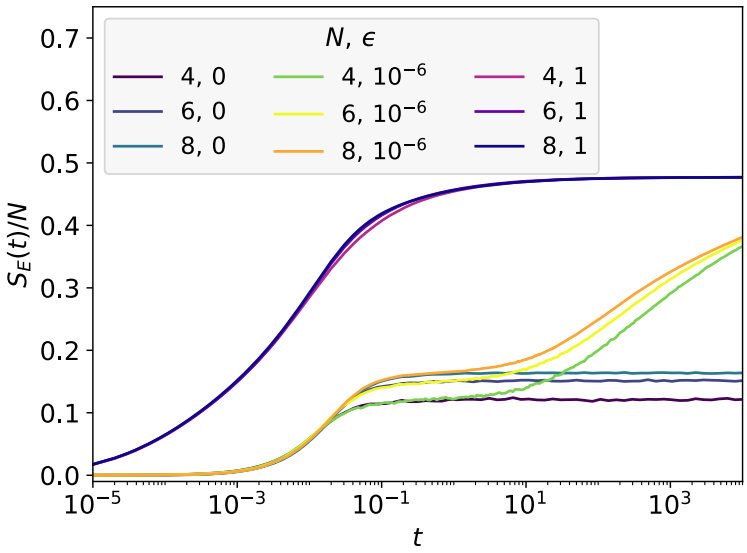

Figure 6.11.: Half-system entanglement entropy $S_E(t)$, as defined in Section 6.3.2, per number of TLSs for various N and ϵ. The plot shows the results for $\overline{\Delta} = 0.1$ and $\eta = 10^5$, averaged over at least 1000 disorder realizations. For $\epsilon = 10^{-6}$, we see that the entanglement spreading takes place in two steps: first, the TLSs become entangled with other TLSs and $S_E(t)/N$ reaches the plateau found in the case of unitary dynamics ($\epsilon = 0$); then, HSEE grows further due to the spread of the entanglement among TLSs and phonons. For $\epsilon = 1$, $S_E(t)/N$ is almost independent of N, indicating a volume law.

are comparable or stronger than dissipation, the system dynamics presents the transient MBL regime; in the opposite case, the system quickly thermalizes. Considering the typical values of the disorder distribution parameters encompassed in the literature, real glassy materials sit in the bulk of the transient MBL region of the phase diagram. These results suggest that the signatures of many-body localization might be experimentally accessible in real glassy samples at ultra-low temperatures, for instance using ultra-fast laser probes. Therefore, our work opens up promising research directions. On the one hand, glasses promise to be a unique platform for probing many-body localization on real materials. On the other hand, the presence of a localized regime in glass dynamics might be at the origin of interesting ultra-low temperature behaviors, which deserve a deep investigation.

7. Two-level systems in glasses: The strong coupling limit

In this Chapter, we explore the quantum dynamics of two-level systems (TLSs) strongly coupled with phonons. Section 7.1 is devoted to a brief discussion on the strong-coupling approximation. In Sections 7.2–7.2.1, we apply a unitary transformation to the full Hamiltonian (TLSs + phonons), and we show how the tunneling amplitudes of the TLSs become exponentially suppressed by the polaron effect. In Section 7.3, by means of perturbation theory, we compute analytically the dissipation rates of the TLSs. We find that their typical value corresponds to the smallest time scale in the problem. Finally, in Section 7.4, we show the presence of a long, localized transient in the TLS dynamics, resembling the weak-coupling result. The reference article for this Chapter is Ref. [280].

This Chapter can be regarded as an extension of Chapter 6, where we discussed the quantum dynamics of two-level systems (TLSs) weakly coupled to a phonon bath. Here, instead, we assume that TLSs are strongly coupled to phonons. While the weak-coupling approximation is usually performed in the literature, and it is known to be a posteriori valid, the strong-coupling approximation has been carried out only in a few previous studies [41, 74]. However, from the experimentally measured values of the TLS disorder parameters, one might be led to consider the strong-coupling approximation more accurate. Indeed, the typical value of the TLS–phonon coupling measured in experiments is of the order of $\gamma \simeq 1$ eV, while the asymmetry energy between the wells is $W \simeq 0.1$ eV, and the tunnelling amplitude is $\overline{\Delta} \simeq 10^{-6}$ eV (see Table 6.1).

In this Chapter, we start by considering the microscopic parameters of the TLS model as *bare* quantities. Performing a simple unitary transformation on the full Hamiltonian of the system TLSs + phonons, we find that the strong coupling between TLSs and phonons induces a polaron effect, i.e. a TLS "brings along" a cloud of phonons which renormalizes its tunneling amplitude. This constitutes a microscopic explanation for the wideness and smallness of the tunneling amplitude distribution encompassed in the literature. Moreover, such suppression of the tunneling amplitudes permits to work out a perturbation theory to compute the relaxation rates of the TLSs, employing for instance the Fermi's golden rule, which shows that the dissipation rates are the smallest time scale in the problem. Thus, one is able to derive the effective dynamics of the TLSs at low temperatures and finds that their quantum dynamics presents a transient localized regime that should be experimentally accessible.

7.1. Observations on the TLS model

As seen in Chapter 6, the full Hamiltonian encompassing the TLSs and the phonon bath is given by

$$H = H_{TLS} + H_{ph} + H_{int}. \tag{7.1}$$

H_{TLS} is the Hamiltonian of free TLSs, which are parametrized with Pauli matrices:

$$H_{TLS} = \sum_i \left(\varepsilon_i \sigma_i^z + \Delta_i \sigma_i^x\right), \tag{7.2}$$

where ε_i is the asymmetry energy between the two states, and Δ_i is the tunnelling amplitude. Both ε_i and Δ_i are random variables. We have already discussed in Chapter 6 the probability distributions of ε_i (Eq. (6.3)) and Δ_i (Eq. (6.4)) usually encompassed in the literature. Those distributions are inferred from simple physical reasoning [33], while they have never been fully justified by experiments. It is worth having in mind that the distributions in Eqs. (6.3)–(6.4) refer to the *renormalized* parameters ε_i and Δ_i. Instead, the Hamiltonian (7.1) encompasses the *bare* quantities, which are in principle not experimentally accessible. Therefore, in this Chapter we proceed without assuming any distribution for the bare ε_i and Δ_i in Eq. (7.1). We will carry out the renormalization procedure in Secs. 7.2–7.2.1, and then we will comment on the renormalized parameter's distributions.

Analogously to Eq. (6.6), we define the phonon bath Hamiltonian as

$$H_{ph} = \sum_{\mathbf{q}s} \hbar\omega_{\mathbf{q}s} b^\dagger_{\mathbf{q}s} b_{\mathbf{q}s}, \tag{7.3}$$

$\omega_{\mathbf{q}s}$ being the phonon frequency, and $b^\dagger_{\mathbf{q}s}$, $b_{\mathbf{q}s}$ the creation/annihilation operators for a phonon with wavevector $\mathbf{q}$ and polarization s. As usual, their commutator reads $[b_{\mathbf{q}s}, b^\dagger_{\mathbf{q}'s'}] = \delta_{s,s'}\delta_{\mathbf{q},\mathbf{q}'}$. As in Chapter 6, we consider a linear dispersion relation: $\omega_{\mathbf{q}s} = v_s|\mathbf{q}|$. Notice that the transverse (T) and longitudinal (L) velocities verify $v_L/v_T \approx 1.6$ (see Table 6.1); however, since their difference is not crucial for the quantities of interest, it is convenient to define thr average velocity $\frac{1}{v^3} := \frac{1}{3}\sum_s \frac{1}{v_s^3}$, as in the weak-coupling limit (see also Appendix B.1). We refer to Table 6.1 for the experimental values of the TLS model parameters.

For later convenience, we also introduce the position and momentum operators of the phonon field:

$$x_{\mathbf{q}s} = \sqrt{\frac{\hbar}{2\omega_{\mathbf{q}s}}}\left(b_{\mathbf{q}s} + b^\dagger_{-\mathbf{q}s}\right), \qquad p_{\mathbf{q}s} = i\sqrt{\frac{\hbar\omega_{\mathbf{q}s}}{2}}\left(b^\dagger_{\mathbf{q}s} - b_{-\mathbf{q}s}\right), \tag{7.4}$$

with commutator $[x_{\mathbf{q}s}, p_{\mathbf{q}'s'}] = i\hbar\delta_{s,s'}\delta_{\mathbf{q},-\mathbf{q}'}$. In these operators, the phonon Hamiltonian reads

$$H_{ph} = \frac{1}{2}\sum_{\mathbf{q}s}\left(p_{\mathbf{q}s}p_{-\mathbf{q}s} + \omega^2_{\mathbf{q}s}x_{\mathbf{q}s}x_{-\mathbf{q}s}\right), \tag{7.5}$$

having dropped a zero-point constant.

Finally, the interaction Hamiltonian that couples phonons to TLSs corresponds to the one defined in Eqs. (6.7)–(6.8). Here, we rewrite it as

$$H_{int} = \sum_{i\mathbf{q}s} \gamma_i\, \sigma_i^z\, \Xi_{i\mathbf{q}s}\, x_{\mathbf{q}s}, \tag{7.6}$$

where γ_i is the coupling strength of site i, with the dimension of an energy, and $\Xi_{i\mathbf{q}s}$ parametrizes the spatial and angular form of the interaction:

$$\Xi_{i\mathbf{q}s} = \frac{-i}{\sqrt{\rho V}} D_i^{ab} e_{\mathbf{q}s}^{ab} e^{i\mathbf{q}\cdot\mathbf{r}_i}. \tag{7.7}$$

In the above expressions, V is the volume of the sample, ρ the material density, $\mathbf{r}_i$ is the position of the i-th TLS, D_i^{ab} is the dimensionless, random elastic dipole tensor, and $e_{\mathbf{q}s}^{ab} := \frac{1}{2}\left(q^a \hat{e}_{\mathbf{q}s}^b + q^b \hat{e}_{\mathbf{q}s}^a\right)$ is a projector, with $\hat{\mathbf{e}}_{\mathbf{q}s}$ being the polarization versors. Notice that in our convention $\hat{\mathbf{e}}_{\mathbf{q}s}^* = \hat{\mathbf{e}}_{-\mathbf{q}s}$; thus, $\Xi_{i\mathbf{q}s}^* = \Xi_{i-\mathbf{q}s}$, and the interaction Hamiltonian is Hermitian, as it should be.

We set $\gamma_i \equiv \gamma$ for each site, and absorb in D_i^{ab} all the randomness. The "experimentally correct" form of D_i^{ab} is inaccessible. However, as we will see in Section 7.2.1, in the strong-coupling approximation the dipole tensor enters the Debye-Waller factor, which suppresses exponentially the tunneling amplitude of the TLS. Therefore, in the strong-coupling limit having an accurate estimate of its numerical value is of primary importance. For this reason, in this Chapter, we will follow Ref. [41] in which this issue has been already discussed. We consider D_i^{ab} as the *difference* of two random tensors, one for each well of the TLS, and we fix the magnitude of its entries from self-consistent criteria for the stability of the amorphous lattice. With these choices, we find $D_i^{ab} \sim O(10)$ (for more details, see Appendix C.1).

7.2. The polaron transformation

According to Table 6.1, $W \lesssim \gamma$: TLSs and phonons are strongly coupled. Therefore, in this Section we perform a *polaron transformation* that takes into account the strong-coupling effects, generating new renormalized parameters which, in turn, can be treated perturbatively [41, 74]. An easy way to derive the correct form of the transformation is the following. Noting that the interaction Hamiltonian in Eq. (7.6) is linear in the phonon position operator $x_{\mathbf{q}s}$, we can "complete the square" in Eq. (7.5) by shifting the origin of the $x_{\mathbf{q}s}$ fields. By inspection, this is accomplished by the unitary transformation

$$U = \exp\left[-\frac{i}{\hbar}\sum_{i\mathbf{q}s} \frac{\gamma}{\omega_{\mathbf{q}s}^2}\sigma_i^z\, \Xi_{i\mathbf{q}s}\, p_{\mathbf{q}s}\right]. \tag{7.8}$$

Thus,

$$U(H_{ph} + H_{int})U^\dagger = H_{ph} - \sum_{ij}\sum_{\mathbf{q}s} \frac{\gamma^2}{2\omega_{\mathbf{q}s}^2}\sigma_i^z\sigma_j^z \Xi_{i\mathbf{q}s}\Xi_{j\mathbf{q}s}^*; \tag{7.9}$$

We see that the interactions generated are in the σ^z-σ^z channel, with couplings

$$J_{ij} := \sum_{\mathbf{q}s} \frac{\gamma^2}{2\omega_{\mathbf{q}s}^2}\Xi_{i\mathbf{q}s}\Xi_{j\mathbf{q}s}^*. \tag{7.10}$$

It is easy to verify that $J_{ij} = 2\hbar\,\Pi_{ij}$, for Π_{ij} defined in Eqs. (B.14). Therefore, following the same computation performed in Appendix B.1.2 for the weak-coupling limit, one arrives at

$$J_{ij} = \frac{\gamma^2 \mathbb{D}_{ij}}{4\pi\rho v^2 r_{ij}^3}, \tag{7.11}$$

where $\mathbb{D}_{ij}$ is the contraction of the dipole moments D_i^{ab} already found in the weak-coupling approximation (cf. Eqs. (B.27) and (C.6)). Considering the experimental values reported in Table 6.1, one finds that the typical value[1] of the interactions is

$$\begin{aligned} \mathrm{SiO_2} &: J_{ij} \approx 3 \times 10^{-5}\ \mathrm{eV} \approx 5 \times 10^{10}\ \mathrm{Hz}; \\ \mathrm{BK7} &: J_{ij} \approx 3 \times 10^{-5}\ \mathrm{eV} \approx 4 \times 10^{10}\ \mathrm{Hz}; \\ \mathrm{PMMA} &: J_{ij} \approx 7 \times 10^{-6}\ \mathrm{eV} \approx 1 \times 10^{10}\ \mathrm{Hz}. \end{aligned} \tag{7.12}$$

Now, we apply the polaron transformation to the TLS Hamiltonian, which involves only Pauli matrices. Defining the phonon operators P_i as

$$U = \exp\left[-i \sum_i P_i \frac{\sigma_i^z}{2}\right] \quad \Longrightarrow \quad P_i = \sum_{\mathbf{q}s} \frac{2\gamma}{\hbar \omega_{\mathbf{q}s}^2} \Xi_{i\mathbf{q}s}\, p_{\mathbf{q}s}, \tag{7.13}$$

we find

$$UH_{TLS}U^\dagger = \sum_i \left[\varepsilon_i \sigma_i^z + \Delta_i \sigma_i^x \cos(P_i) + \Delta_i \sigma_i^y \sin(P_i)\right]. \tag{7.14}$$

Hence, we obtain an equivalent Hamiltonian for the TLSs in an elastic medium, that reads

$$H' = UHU^\dagger = H_{ph} + \sum_i \left[\varepsilon_i \sigma_i^z + \Delta_i \sigma_i^x \cos(P_i) + \Delta_i \sigma_i^y \sin(P_i)\right] + \sum_{ij} J_{ij} \sigma_i^z \sigma_j^z \tag{7.15}$$

$$= H_{ph} + \sum_i \left[\varepsilon_i \sigma_i^z + \Delta_i \sigma_i^+ e^{-iP_i} + \Delta_i \sigma_i^- e^{iP_i}\right] + \sum_{ij} J_{ij} \sigma_i^z \sigma_j^z \tag{7.16}$$

with $\sigma^\pm := \frac{1}{2}(\sigma^x \pm i\sigma^y)$. Notice that H' is *exactly* equivalent to H, since we have just performed a unitary transformation.

Summarizing, from Eqs. (7.15)–(7.16), we see that the polaron transformation has generated a direct coupling between TLSs, and a new TLS–phonon coupling via $\sigma_i^x \cos(P_i)$ and $\sigma_i^y \sin(P_i)$ or, equivalently, $\sigma_i^+ e^{-iP_i}$ and $\sigma_i^- e^{iP_i}$. The latter phonon operators are clearly complicated. In the next Section 7.2.1, we will show how to rewrite them in a easier form to deal with. Eq. (7.16) gives a clear physical interpretation of the whole transformation: the operators $e^{\pm iP_i}$ shift the "position" x of the phonon field as a TLS jumps between up and down states.

7.2.1. Normal ordering

To begin with, let us consider the following average on a thermal state:

$$\langle e^{iP_i} \rangle_T = \exp\left\{-\sum_{\mathbf{q}s} \frac{\gamma^2}{\hbar \omega_{\mathbf{q}s}^3} \Xi_{i\mathbf{q}s} \Xi_{i\mathbf{q}s}^* \coth\left(\frac{\beta \hbar \omega_{\mathbf{q}s}}{2}\right)\right\} =: e^{-\Gamma_i^2(T)/2}. \tag{7.17}$$

$\Gamma_i^2(T)$ is known as the *Debye-Waller factor*. We will denote $\Gamma_{i,0}^2 := \Gamma_i^2(0)$. We compute it explicitly in Appendix C.2, finding that, at $T \gg T_D/2$,

$$\frac{\Gamma_i^2}{2} = \frac{\gamma^2 k_B^2 T_D^2 \mathrm{Tr}(D_i^2)}{12\pi^2 \rho \hbar^3 v^5} + O\left(e^{-T_D/2T}\right); \tag{7.18}$$

[1] We define the typical value of a random variable X with probability distribution $P(X)$ as $X_{\mathrm{typ}} := \exp\left(\int dX\, P(X) \log(X)\right)$.

hence, the Debye-Waller factor increases exponentially slowly in temperature. We can rewrite it as

$$\frac{\Gamma_i^2}{2} = \frac{E_D^2}{4E_i^2} + O\big(e^{-T_D/2T}\big), \tag{7.19}$$

where $E_D := k_B T_D$ is the Debye energy, and E_i is defined as:

$$E_i := \sqrt{\frac{3\pi^2\hbar^3\rho v^5}{\gamma^2 \mathrm{Tr}(D_i^2)}}. \tag{7.20}$$

For the materials in Table 6.1, the minimum value E_i is:

$$\mathrm{SiO_2}: \; E_{i,min} \simeq 2.8 \text{ meV}; \quad \mathrm{BK7}: \; E_{i,min} \simeq 2.6 \text{ meV}; \quad \mathrm{PMMA}: \; E_{i,min} \simeq 0.79 \text{ meV}. \tag{7.21}$$

Therefore, from Eq. (7.19) we find at zero temperature

$$\mathrm{SiO_2}: \; 0 \leq \frac{\Gamma_{i,0}^2}{2} \leq 28; \quad \mathrm{BK7}: \; 0 \leq \frac{\Gamma_{i,0}^2}{2} \leq 33; \quad \mathrm{PMMA}: \; 0 \leq \frac{\Gamma_{i,0}^2}{2} \leq 32. \tag{7.22}$$

These ranges of values are very close to the ones found in Ref. [41] (parameter α, pag. 3). We stress again that $\Gamma_{i,0}^2$, while being at zero temperature, does fluctuate since the TLSs are coupled via a random dipole tensor D_i to the phonons. Reintroducing the temperature, one finds that $\Gamma_i^2(T_D) \simeq 4\Gamma_{i,0}^2$ (see Appendix C.2).

We wish to find a more manageable expression for the operators $e^{\pm iP_i}$ in Eq. (7.16). First, without making any approximation, $e^{\pm iP_i}$ can be normal ordered. We use the Baker-Campbell-Hausdorff formula which, applied to creation and annihilation operators, gives

$$e^{c_i b_i + c_j^* b_j^\dagger} = e^{c_j^* b_j^\dagger} e^{c_i b_i} e^{\frac{1}{2} c_i c_j^* \delta_{ij}}. \tag{7.23}$$

We find

$$e^{iP_i} = e^{i\Gamma_{i,0}\tilde{b}_i^\dagger} e^{-i\Gamma_{i,0}\tilde{b}_i} e^{-\Gamma_{i,0}^2/2}, \tag{7.24}$$

having defined

$$\tilde{b}_i := \frac{\gamma}{\Gamma_{i,0}} \sum_{\mathbf{q}s} \sqrt{\frac{2}{\hbar\omega_{\mathbf{q}s}^3}} \Xi_{i\mathbf{q}s}^* b_{\mathbf{q}s}, \qquad \tilde{b}_i^\dagger := \frac{\gamma}{\Gamma_{i,0}} \sum_{\mathbf{q}s} \sqrt{\frac{2}{\hbar\omega_{\mathbf{q}s}^3}} \Xi_{i\mathbf{q}s} b_{\mathbf{q}s}^\dagger. \tag{7.25}$$

Eq. (7.23) shows that the normal ordering procedure generates the Debye-Waller factor on the vacuum state, i.e. at zero temperature. Notice that, thanks to the pre-factor $(\Gamma_{i,0})^{-1}$, the operators $\tilde{b}$ and $\tilde{b}^\dagger$ can be considered of order 1.

At this point, the Hamiltonian in (7.16) can be rewritten exactly as

$$H' = H_{ph} + \sum_i \left[\varepsilon_i \sigma_i^z + \overline{\Delta}_i \sigma_i^+ e^{-i\Gamma_{i,0}\tilde{b}_i^\dagger} e^{i\Gamma_{i,0}\tilde{b}_i} + \overline{\Delta}_i \sigma_i^- e^{i\Gamma_{i,0}\tilde{b}_i^\dagger} e^{-i\Gamma_{i,0}\tilde{b}_i} \right] + \sum_{ij} J_{ij} \sigma_i^z \sigma_j^z \tag{7.26}$$

with the renormalized tunneling amplitudes

$$\overline{\Delta}_i := e^{-\Gamma_{i,0}^2/2} \Delta_i. \tag{7.27}$$

The physical interpretation is the following: the tunneling amplitude of a TLS is exponentially suppressed by the Debye-Waller factor since the TLS has to "bring along" a cloud of phonons,

namely the polaron [74]. In other words, when a TLS tunnels in one well, the neighboring atoms rearrange to accommodate it. Hence, they make it harder for the TLS to tunnel back.

It is clear that the presence of the Debye-Waller factor, which is a random variable dependent on the TLS–phonon interaction, produces a wide distribution of tunneling amplitudes $\overline{\Delta}_i$; in particular, large values of the Debye-Waller factor favor small $\overline{\Delta}_i$. As highlighted in Refs. [41, 86], the distributions of the TLS parameters $p_\varepsilon(\varepsilon)$ and $p_\Delta(\Delta)$, employed in the standard TLS model (see Eqs. (6.3)–(6.4)), derive just from simplicity standpoints, while they have not been confirmed by experimental or numerical observations. Hence, following C. C. Yu and H. M. Carruzzo in Ref. [41], following the strong-coupling derivation, one can legitimate define

$$\overline{\Delta}_i := \Delta_{max}\, e^{-\Gamma_{i,0}^2/2}, \tag{7.28}$$

where $\Delta_{max} \approx 10$ meV as reported in Table 6.1. The definition (7.28) enhances the presence of very small tunneling amplitudes, which however are likely not observable in standard measurements, e.g. in internal friction experiments. Indeed, only the TLSs that can tunnel fast enough to respond within the experimental time can be observed in experimental measurements. Because of the strong-coupling effects, in this Chapter we will apply Eq. (7.28).

7.3. Perturbation theory for the relaxation of the TLSs

To get a grasp of the physics of the Hamiltonian in Eq. (7.26), we can proceed perturbatively. Indeed, by means of the polaron transformation, we have already taken into account the strong-coupling effects, generating new "small" renormalized parameters. Since our ultimate goal is to focus on the reduced system composed of TLSs only, we can proceed considering the phonons as a thermal bath.

The Hamiltonian in Eq. (7.26) presents three competing energy scales. For SiO_2, their typical values are[2]:

$$\varepsilon_i \approx 10^{15}\ \text{Hz}; \qquad \overline{\Delta}_i \approx 10^{5}\ \text{Hz}; \qquad J_{ij} \approx 10^{11}\ \text{Hz}\,. \tag{7.29}$$

Since $\varepsilon_i \gg \overline{\Delta}_i, J_{ij}$, we can proceed further assuming that the TLSs are *non-interacting*. Indeed, since the level spacing is of the order of ε_i, as a first step one can neglect the interactions J_{ij}. We will come back to the effects of the interactions at the end of this Section.

At infinite temperature, the "up" and "down" states of the TLSs would be equally populated. We wish to consider the decay of an "up" TLS into phonons. However, before proceeding some considerations are in order. The physical "up" and "down" states for the TLSs are the ones of the Hamiltonian (7.26), or in other words the TLS states *after* having applied the polaron transformation. Since the interactions J_{ij} are smaller than the onsite energy ε_i, we can safely consider the TLSs one by one when they decay. Moreover, since the phonons are a thermodynamically large system, we can assume that they are not influenced by the flipping of one TLS. For these reasons, we can safely assume that the phonon ground state is left unchanged in the asymptotically far regions, even if the operators $\overline{\Delta}_i \sigma_i^{\mp} e^{\pm i\Gamma_{i,0}\tilde{b}_i^\dagger} e^{\mp i\Gamma_{i,0}\tilde{b}_i}$ not only flip the TLS, but also shift locally the phonon ground state.

Within the above assumptions, we can use the Fermi's golden rule applied to only one TLS:

$$Y_i = \sum_f \frac{2\pi}{\hbar} \left| \langle f, \downarrow | \, \overline{\Delta}_i \sigma_i^- e^{i\Gamma_{i,0}\tilde{b}_i^\dagger} e^{-i\Gamma_{i,0}\tilde{b}_i} \, |0, \uparrow\rangle \right|^2 \rho_f(2\varepsilon_i) \tag{7.30}$$

[2] For the other materials in Table 6.1 the ratio between the energy scales is similar.

where $\rho_f(E)$ is the density of states of the final state of the phonons at energy E. In particular, the final state can be thought as made of phonons of the *unperturbed* Hamiltonian H_{ph}. The explicit computation of the decay rates is performed in Appendix C.3; the result is

$$Y_i = \frac{\pi \overline{\Delta}_i^2 \varepsilon_i}{\hbar E_i^2} e^{-2\varepsilon_i/E_D} \, {}_pF_q\left(;\frac{3}{2},2;\frac{\varepsilon_i^2}{4E_i^2}\right), \tag{7.31}$$

where ${}_pF_q$ is a generalized hypergeometric function (see Eq. (C.27) for its definition and Eq. (C.28) for its asymptotics), E_D is the Debye energy and E_i is defined in Eq. (7.20).

The decay rate in Eq. (7.31) is correct to order $O(\overline{\Delta}_i^2)$, and to all orders in $\tilde{b}_i^\dagger$, $\tilde{b}_i$. Therefore, we expect it to give a pretty accurate result. Considering the materials in Table 6.1, the typical values of the TLS dissipation rates are

$$\begin{aligned} \mathrm{SiO_2} &: Y_i \approx 5 \times 10^{-16} \text{ eV} \approx 8 \times 10^{-1} \text{ Hz}; \\ \mathrm{BK7} &: Y_i \approx 4 \times 10^{-19} \text{ eV} \approx 5 \times 10^{-4} \text{ Hz}; \\ \mathrm{PMMA} &: Y_i \approx 8 \times 10^{-19} \text{ eV} \approx 1 \times 10^{-3} \text{ Hz}. \end{aligned} \tag{7.32}$$

Due to the wideness of the distribution of Y_i, which covers many orders of magnitude, such typical values are considerably small.

Since $J_{ij} \gg \hbar Y_i$, at least at the level of typical values, we expect the coherent dynamics of the TLSs to be observable for a large time window before thermalization ultimately takes place. However, the thermalization rates Y_i in Eq. (7.32) should be taken with a grain of salt. As in the weak-coupling limit of Chapter 6, the probability distribution of Y_i is very wide, spanning many orders of magnitude. In Eq. (7.32), instead, we are considering only the typical values of the dissipation rates, which are defined as $Y_{\text{typ}} := \exp\left(\int dY\, P(Y) \log(Y)\right)$. The surprisingly small typical values that we find are due to the polaron effect considered in Eq. (7.28) according to Ref. [41]. It is worth noticing, however, that the dissipation rates dominating an experiment are not a priori obvious. One should evaluate them case by case. This issue should be further investigated in collaboration also with experimental physicists.

Let us now consider the effects of the interactions. We argue that the rates in Eq. (7.31) are almost unchanged if perturbation theory is performed with respect to the interacting Hamiltonian $\sum_i \varepsilon_i \sigma_i^z + \sum_{ij} J_{ij} \sigma_i^z \sigma_j^z$. Indeed, even though a phonon-mediated process might speed up the decay of a *configuration* of "up" TLSs, favoring the energy matching condition for the decay, more TLSs in the configuration need to be flipped, and this happens at higher orders in $\overline{\Delta}_i$. Therefore, the perturbation theory that we have developed should capture the essential features of the relaxation dynamics of the TLSs and should be numerically accurate to a fair degree.

7.4. Effective dynamics of the TLSs at low temperatures

Given the normal ordered Hamiltonian in Eq. (7.26), we can set up a Gorini-Kossakowski-Sudarshan-Lindblad (GKSL) equation for the dynamics of the TLSs in the presence of a phononic thermal bath. We recall that the GKSL equation (Eq. (6.9)) for the reduced density matrix of the TLSs, ρ, reads

$$\partial_t \rho(t) = -\frac{i}{\hbar}[H_{TLS} + H_{LS}, \rho(t)] + \sum_\kappa \mathcal{L}_\kappa \rho(t). \tag{7.33}$$

where $H_{TLS} = \sum_i \varepsilon_i \sigma_i^z + \sum_{ij} J_{ij} \sigma_i^z \sigma_j^z$ is the unperturbed TLS Hamiltonian, H_{LS} encompasses the Lamb and Stark shifts, and $\mathcal{L}_\kappa$ are Lindblad superoperators acting on the TLS density matrix ρ. In principle, the index κ can take $O(N^2)$ values, however, following the arguments in the previous Section 7.3, in the case of TLSs we can reasonably assume that κ reduces to the site index i, in agreement with the weak-coupling approximation in Chapter 6.

We consider the phonons *at zero temperature*. This approximation is exponentially good in $T_D/2T$, as seen for the Debye-Waller factor in Section 7.2.1. Hence, we find at leading order in $\overline{\Delta}_i$

$$\partial_t \rho(t) = -\frac{i}{\hbar}\left[\sum_i \varepsilon_i \sigma_i^z + \sum_{ij} J_{ij}\sigma_i^z\sigma_j^z,\ \rho(t)\right] + \sum_i Y_i\Big(\sigma_i^+ \rho(t) \sigma_i^- + \{\sigma_i^z, \rho(t)\} - 2\rho(t)\Big) \quad (7.34)$$

with J_{ij} given in Eq. (7.11), and Y_i in Eq. (7.31). In the above equation, we neglected the Lamb-Stark shift terms which are of the second order in $\overline{\Delta}_i$, while the interactions J_{ij} are of zeroth order.

7.5. Conclusions and outlook

In this Chapter, we investigated the quantum dynamics of the two-level system (TLS) model for glasses at ultra-low temperatures. We considered an ensemble of TLSs strongly coupled to phonons. While the weak-coupling approximation is often taken in the standard literature on the TLS model and it turns out to be completely justified a posteriori, as shown in Section 6.2.3, the experimental values of the TLS model parameters suggest that, in principle, the strong-coupling approximation might be more accurate.

Starting from this observation and employing a simple unitary transformation, we wrote the Hamiltonian of the full system (TLSs + phonons) in a more suitable form. In this way, we found that the tunneling amplitudes of the TLSs become renormalized by the Debye-Waller factor: they are exponentially suppressed because of the polaron effect on the TLSs. Such renormalization provides an explanation for the wide distribution and the small typical value attributed to the TLS tunneling amplitude in the literature. By means of a perturbation theory in the tunneling amplitude, we computed analytically the dissipation rates of the TLSs. Such rates are smaller than those found within the weak-coupling approximation. Moreover, within the strong-coupling approximation, we derived a phenomenological master equation in the Gorini-Kossakowski-Sudarshan-Lindblad (GKSL) form, finding the presence of a localized transient regime in the TLS dynamics. This result is in agreement with the one obtained within the weak-coupling approximation in Chapter 6. Therefore, it supports the possibility that a many-body localized regime might be observed in experiments on ultra-low temperature glasses.

8. Spatio-temporal heterogeneities of entanglement in the many-body localized phase

In this Chapter, we propose a spatio-temporal characterization of the entanglement dynamics in many-body localized systems. Specifically, we find that the relaxation times of local entanglement, as measured by the concurrence, are spatially correlated, giving rise to a dynamical correlation length for quantum entanglement. Remarkably, our findings resemble dynamical heterogeneities of classical glasses. After characterizing the model and the methods in Sections 8.1–8.2, we present the numerical results in Section 8.3. In Section 8.4, we discuss the future research directions that these findings open up. The reference article for this Chapter is Ref. [281].

The assumption of local equilibrium is at the core of statistical mechanics: even if isolated from the rest of the universe, a generic many-body system is expected to act as a thermal bath for itself, quickly driving the statistics of local observables to the Gibbs ensemble, by means of classical [282–284] or quantum [187, 285] chaos. The situations in which ergodization fails and the system persists in non-thermal states for all relevant time scales, are therefore of paramount interest, both at the classical and the quantum level [184, 185, 187]. Glasses are a prototypical example of classical systems that remain trapped in metastable states for all experimentally accessible time scales (see Chapter 1). In the quantum realm, after the seminal works [182, 183], it has become clear that isolated, disordered many-body systems can elude thermal equilibrium even at *infinite* time. This non-ergodic phase of matter has been coined many-body localization. We discussed it in Chapter 5, highlighting its common aspects and dissimilarities with respect to both classical and quantum glasses. We illustrated that the lack of ergodicity in the many-body localized (MBL) phase can be linked to the existence of an extensive number of local integrals of motion (LIOMs), by which one can construct a phenomenological model known as the l-bit model.

While in the case of two qubits entanglement can be completely characterized [238, 239, 286], in the case of many-body systems it has been proved difficult to quantify it in a definitive way, and only a handful of general properties are known. Several different measures of the entanglement have been proposed [241, 287, 288], which capture only specific properties of the quantity. The numerous studies on the entanglement growth in the MBL phase [198, 230, 231, 289, 290] are mainly focused on global properties, employing measures such as entanglement entropy, purity, quantum Fisher information [205, 212], or total correlations [286, 291].

In this Chapter, we wish to go beyond those approaches, focusing on a quantity that can measure local properties of entanglement, thus characterizing its spreading in a more detailed way. We focus on the time and space behavior of the concurrence, which has been defined in Chapter 5 and already employed in Chapter 6. We quantitatively study the distribution of

relaxation times of the onsite concurrence in the l-bit model and describe its properties in a wide range of parameters and initial-state energies. We show that the relaxation times of the onsite concurrence are spatially correlated and that they present a long-tailed, power-law-like distribution. Both the spatial correlation and the width of the distribution grow as the disorder increases or the energy of the initial state decreases.

These properties provide a clear connection with dynamical heterogeneities, i.e. spatio-temporal fluctuations, observed in classical amorphous materials and spin glasses (see Chapter 1). Hence, our findings add one more point of contact between the physics of glasses and MBL systems [197, 249] (see also Chapters 4, 6, and 7). It has already been argued that such heterogeneities have a quantum counterpart and, at ultra-low temperatures, can be induced by quantum fluctuations [170, 264, 292, 293]. Previous studies, however, were focused on quantum glass systems modeled on a classical counterpart. For the first time, we focus on the MBL phase, which is a novel, non-ergodic state of matter, that only exists in the quantum realm. Moreover, we study the entanglement, which is a genuine quantum object with no classical analog: the observed similarity to the classical case is even more remarkable.

8.1. Definition of the model

We aim at studying general principles of the spatio-temporal entanglement dynamics of MBL systems. For that purpose, we focus on an effective description in terms of LIOMs, which allows us to access the nonequilibrium real-time dynamics of MBL systems for long times and large system sizes. Deep in the MBL phase, Hamiltonians of short-range interacting quantum spin-1/2 degrees of freedom can be diagonalized through a quasi-local unitary transformation U, yielding a representation of the model in so-called l-bit form (Chapter 5, Eq (5.4)). In this Chapter, we neglect the terms in the l-bit Hamiltonian comprising n-body interactions with $n \geq 3$, which is a controlled approximation for weakly interacting spins in the original microscopic model. Thus, we employ the Hamiltonian

$$H_{l\text{-bit}} = \sum_{i=1}^{L} h_i \tau_i^z + \sum_{i,j=1}^{L} J_{ij} \tau_i^z \tau_j^z, \tag{8.1}$$

where $\{\tau_i^x, \tau_i^y, \tau_i^z\}$ are the localized spin-1/2 operators associated with the LIOMs. The interactions J_{ij} are known to be exponentially suppressed with the distance r_{ij} between localization centers. In order to achieve a model-independent effective description, here we will take one step further by parametrizing the l-bit model as follows. First, we assume that the h_i are independent identically distributed random fields, with a uniform distribution over $[-h, h]$, and that the J_{ij} are uncorrelated Gaussian variables of zero average and standard deviation $J_0 e^{-r_{ij}/\kappa}$. For numerical purposes we set both $h = J_0 = 1$.

The particular advantage of the l-bit model in Eq. (8.1) is that it not only allows us to perform analytical estimates of few-body observables but also to efficiently compute them numerically reaching system sizes up to $L = 140$ spins for long times [231, 233, 235, 266]. It is worth stressing that the l-bits become more and more similar to the physical spins as the disorder strength is increased, ultimately coinciding asymptotically at infinite disorder [223, 224]. Thus, at small values of κ (i.e., large disorder strength), one can safely consider the l-bits as uniformly spaced on a chain, and compute the distances between them as $r_{ij} = |i - j|$, $i, j = 1, 2, \ldots, L$. Our numerical results are obtained exactly in this strongly localized regime, deep in the MBL phase. It is important to note that the effective model also provides

us handles to tune: i) the interaction decay length κ (equivalent to varying the disorder strength); and ii) the initial condition and therefore the energy density at which we probe the system's properties. Concerning the latter case, we choose as initial state of the dynamics a product state in the *effective* spin basis:

$$|\psi_0\rangle = \bigotimes_{i=1}^{L} \left(A_i|\Uparrow\rangle_i + B_i|\Downarrow\rangle_i\right), \tag{8.2}$$

where $|\Uparrow\rangle_i$,$|\Downarrow\rangle_i$ are the eigenstates of σ_i^z, and $|A_i|^2 + |B_i|^2 = 1$. In employing Eq. (8.2), the system is initially prepared in a superposition of eigenstates, as it would be the case when deriving the l-bit model from a microscopic Hamiltonian. Moreover, the above parametrization of the initial condition provides us with the flexibility to tune the coefficients A_i and B_i such that we can vary its energy E: $\langle\psi_0|H_{l\text{-bit}}|\psi_0\rangle = E$. This can be easily achieved employing a classical simulated annealing algorithm (see Appendix D.1 for more details), and allows us to effectively explore different regions of the energy spectrum. We will measure E in units of the standard deviations of h_i and $\sum_j J_{ij}$ (see Eq. (8.1)), defining the dimensionless energy density $\varepsilon := (E/N)/\sqrt{h^2/3 + 2J_0^2/(e^{2/\kappa} - 1)}$. Notice that $\varepsilon = 0$ corresponds to the center of the spectrum, while $\varepsilon \approx -1$ to the ground state [294] (see also Appendix D.1). We also recall that the localization properties of MBL systems depend on the energy of the state considered, and are stronger near the edges of the spectrum [295].

8.2. Definition of the spatio-temporal quantifiers of the entanglement

For the purpose of exploring dynamic entanglement heterogeneities in MBL systems, in the following, we will concentrate on the two-site concurrence, which quantifies the pairwise entanglement. In MBL systems the mean value of the concurrence decays in time as a power law, as opposed to the exponential decay observed in ergodic systems [242] (see also Chapter 5). It will be the key goal of our work to establish a more detailed spatio-temporal analysis of the concurrence beyond its mean value. For that purpose, we define a local concurrence via

$$C_i(t) := \sum_j C_{ij}(t)\,, \tag{8.3}$$

quantifying the total amount of entanglement of i with all the other lattice sites. We find that (for large systems and for a single disorder realization) this local concurrence typically decays on a certain time scale, which motivates us to define a local relaxation time as

$$\tau_i := t_0\, e^{\langle \ln(t/t_0)\rangle_C} = t_0 \exp \frac{\int_0^{t_{\text{fin}}} \ln(t/t_0)\, C_i(t) dt}{\int_0^{t_{\text{fin}}} C_i(t) dt}, \tag{8.4}$$

where $t_0 = J_0^{-1}$. Notice that $C_i \geq 0$, i.e. the averages above are well-defined and independent of t_0 (in the thermodynamic limit). The definition (8.4) employs the logarithm $\ln(t/t_0)$ to ensure that τ_i is a good estimator of the *typical* time scale of the decay time of the concurrence, even if $C_i(t)$ decays very slowly [1]. For *finite* systems, typically $C_i(\infty) \simeq O(2^{-L})$ (cf. Chapter 6 and Appendix B.3). Thus, the function $C_i(t)$ might be interpreted as a probability distribution

[1] We verified that, upon changing the definition of τ_i, e.g. with $\tau_i := \langle t\rangle_C = \int_0^{t_{\text{fin}}} t\, C_i(t) dt / \int_0^{t_{\text{fin}}} C_i(t) dt$ or $\tau_i := \max\{t | C_i(t) > 0\}$, our findings do not qualitatively change.

in $\mathbb{R}$ only in the thermodynamic limit. Therefore, when considering below the distribution functions of τ_i, the thermodynamic limit can be approached by fixing the maximum simulation time of the dynamics t_{fin} upon increasing L until convergence is reached. We find from our numerics that this typically happens for $L \gtrsim 30$ (see Appendix D.3), which is achievable in the l-bit but not for microscopic Hamiltonians by means of exact diagonalization. This represents a key argument for the use of the effective l-bit model.

While the τ_i's provide us with temporal information of the entanglement dynamics, we are further interested in the spatial component. For that purpose we quantify the spatial correlations of the local relaxation time via [20]

$$G_\tau(r) := \overline{\left[\frac{\langle \tau_i \tau_j \rangle_{\text{is}} - \langle \tau_i \rangle_{\text{is}} \langle \tau_j \rangle_{\text{is}}}{\langle \tau_i^2 \rangle_{\text{is}} - \langle \tau_i \rangle_{\text{is}}^2}\right]_{|i-j|=r}}, \tag{8.5}$$

where $\langle \bullet \rangle_{\text{is}}$ denotes the average over different initial states, $[\bullet]_{|i-j|=r}$ the average over all sites i, j separated by a distance r, and $\overline{[\bullet]}$ the average over different disorder realizations[2]. In Appendix D.3, we show that $G_\tau(r)$ as defined in Eq. (8.5) is very robust to finite-size effects and disorder fluctuations: it is a self-averaging quantity. From our numerical simulations, we find that $G_\tau(r)$ experiences, in general, a stretched exponential decay as a function of r. This allows us to define a length scale η_τ by performing a fit of the form $\log G_\tau(r) \sim a + (r/\eta_\tau)^b$ for some suitable a and b. The length η_τ quantifies the distance over which the local entanglement relaxation is spatially correlated, i.e. it gives the size of the typical clusters of fast or slow entangling spins.

For small system sizes, we will also compare the results of the effective model with a full microscopic calculation for the spin-1/2 XXZ chain with random fields, defined in Eq. (5.2) and that we report here for completeness:

$$H_{\text{XXZ}} = \sum_{i=1}^{L-1} \left[\frac{J}{2}(S_i^+ S_{i+1}^- + \text{h.c.}) + V S_i^z S_{i+1}^z\right] + \sum_{i=1}^{L} \Delta_i S_i^z, \tag{8.6}$$

where $J = V = 1$ and Δ_i are random variables uniformly distributed over $[-\frac{W}{2}, \frac{W}{2}]$. For $W_c \simeq 7 \pm 2$ this model exhibits a many-body localization transition [199]. More details on the relation between W and the effective model parameters h, κ and J_0 can be found in Refs. [223, 224]. In order to probe the centre of the spectrum we initialize the system in a Néel state $|\psi_0\rangle = |\uparrow\downarrow\uparrow\downarrow \ldots\rangle$ and we average the results over different disorder realizations. We find that $C_{ij} = 0$ for $|i-j| > 1$ so that we restrict ourselves for the local concurrence according to $C_i(t) = \sum_j C_{ij}(t) \to C_{ii+1}(t)$.

8.3. Numerical results

We start by showing in Fig. 8.1 the probability distribution function (pdf) of $\log_{10} \tau_i$, obtained within both the XXZ and the l-bit model. We see that within the XXZ model (Fig. 8.1a), the pdf's show a peak at the largest relaxation time, corresponding to the final simulation time of the dynamics t_{fin}. In Appendix D.3, we argue that this feature is due to the (typical) asymptotic value $C_i(\infty) \simeq O(2^{-L})$; see also the discussion below Eq. (8.4). If the time spent in such asymptotic region is too large, the decay time is heavily influenced by the final time of the dynamics. This is a finite-size effect, and it does disappear upon considering larger

[2] Notice that the averages have to be taken in the proper order: first $\langle \bullet \rangle_{\text{is}}$, second $[\bullet]_{|i-j|=r}$, finally $\overline{[\bullet]}$.

system sizes, as we show for the l-bit model in Appendix D.3 (larger system sizes for the XXZ model cannot be presently considered).

The pdf's obtained considering the l-bit model for $L = 80$, and for different values of κ and ε, are shown in Figs. 8.1b–8.1c. Thanks to the large system size, these plots do not present any peak at large times, and clearly show that the pdf of $\log_{10} \tau_i$ has a power-law tail: thus, in turn, also τ_i is power-law distributed. We see that the pdf's become wider as the disorder is increased (both in the XXZ and the l-bit model), or the energy is lowered (in the l-bit model).

We define the typical value of τ_i as $\mathrm{typ}[\tau_i] := t_0 \exp\langle \ln(\tau_i/t_0)\rangle_{\tau_i}$, where $\langle \bullet \rangle_{\tau_i}$ is the average over the pdf of τ_i. In Fig. 8.2a, we show the behavior of $\mathrm{typ}[\tau_i]$ as a function of the parameters κ and ε. Following usual arguments for the l-bit model [231, 233], in Appendix D.2 we derive the rough estimate: $\ln(\mathrm{typ}[\tau_i]/t_0) \approx (2\kappa \ln 2 - 1)^{-1}$. Fig. 8.2a depicts the fits of $\mathrm{typ}[\tau_i]$ with this functional relation with respect to κ, showing that our numerical results are in good agreement with this prediction. In Fig. 8.2b we plot the power-law exponents β obtained from the fit of $P(\log_{10} \tau_i) \sim (\log_{10} \tau_i)^{-\beta}$, that are shown in Fig 8.1b. We see that β has a roughly linear dependence on κ.

The spatial correlations between the τ_i's are plotted in Fig. 8.3. Considered the presence of too strong finite-size effects for the XXZ model, we restrict ourselves to the l-bit model. In Fig. 8.3a we show the spatial distribution of the τ_i's for a disorder realization. As κ decreases, i.e. the disorder increases, the relaxation times of the local entanglement become spatially correlated on longer distances. The correlation function $G_\tau(r)$, defined in Eq. (8.5), is shown in Fig. 8.3b–8.3c: $G_\tau(r)$ decays more slowly upon decreasing κ and ε, confirming the pattern observed in Fig. 8.3a. The same result is also supported by the (qualitative) behavior of the dynamical correlation length η_τ as a function of κ. We see in the inset of Fig. 8.3c that η_τ decreases when κ increases, i.e. when disorder increases.

The implications are twofold. The local entanglement spreading slows down when κ decreases, i.e. the disorder increases, or the energy decreases (Fig. 8.1), and increasingly larger clusters of spins emerge, in which the entanglement relaxation is correlated (Fig. 8.3). As disorder increases, the distribution of relaxation times becomes wider, implying that more clusters are likely to assume an extreme value of the relaxation time in the slow, as well as in the fast tail. These findings might seem surprising in the quantum case, as a more localized structure might be expected when disorder increases. However, they are in agreement with the behavior of classical amorphous materials and spin glasses. In particular, they resemble the results in Ref. [20] in the case of the classical Ising spin glass in $d = 2, 3$, where the authors found that heterogeneities amplify when the temperature of the bath is lowered, and the glass transition is approached.

8.4. Conclusions and outlook

We studied the spreading of entanglement in many-body localized (MBL) systems by monitoring the onsite concurrence. We showed that in the MBL phase the relaxation times of the onsite concurrence increase upon increasing the disorder, or upon lowering the energy of the initial states. Specifically, the local relaxation times become more spatially correlated, and their distribution broadens. Thus, as disorder increases or energy decreases, entanglement heterogeneities arise: we observe the formation of increasingly larger dynamically correlated clusters, in which the entanglement relaxation times are likely to assume an extremely small or large value. Remarkably, the presence of such heterogeneities spotlights the connection

between the local behavior of quantum entanglement in MBL systems and the dynamical properties of classical glasses.

Our analysis applies to the deep, many-body localized phase, where the l-bits are close to the physical spins. Entanglement heterogeneities are expected in all systems that present a long, localized transient before they reach a thermal state. Such systems include MBL systems coupled to a bath, MBL systems in $d \geq 2$, and two-level systems in structural glasses (see Chapters 6–7).

Our findings open up future research directions towards the characterization of spatio-temporal entanglement properties. A crucial step in the future would be to explore the spatial correlation of local relaxation times by means of observables less affected by finite-size effects and disorder fluctuations. It would be desirable to define suitable *macroscopic* observables, in the way the four-point susceptibility $\chi_4(t)$ is for classical glasses [1, 11, 23, 24]. In the MBL case, such observables need to detect only local entanglement fluctuations and be, possibly, experimentally measurable. A further interesting extension of our contribution could be to consider entanglement heterogeneities for two subsystems consisting of more than one spin, which could provide additional information on the multipartite spatio-temporal structure of quantum entanglement.

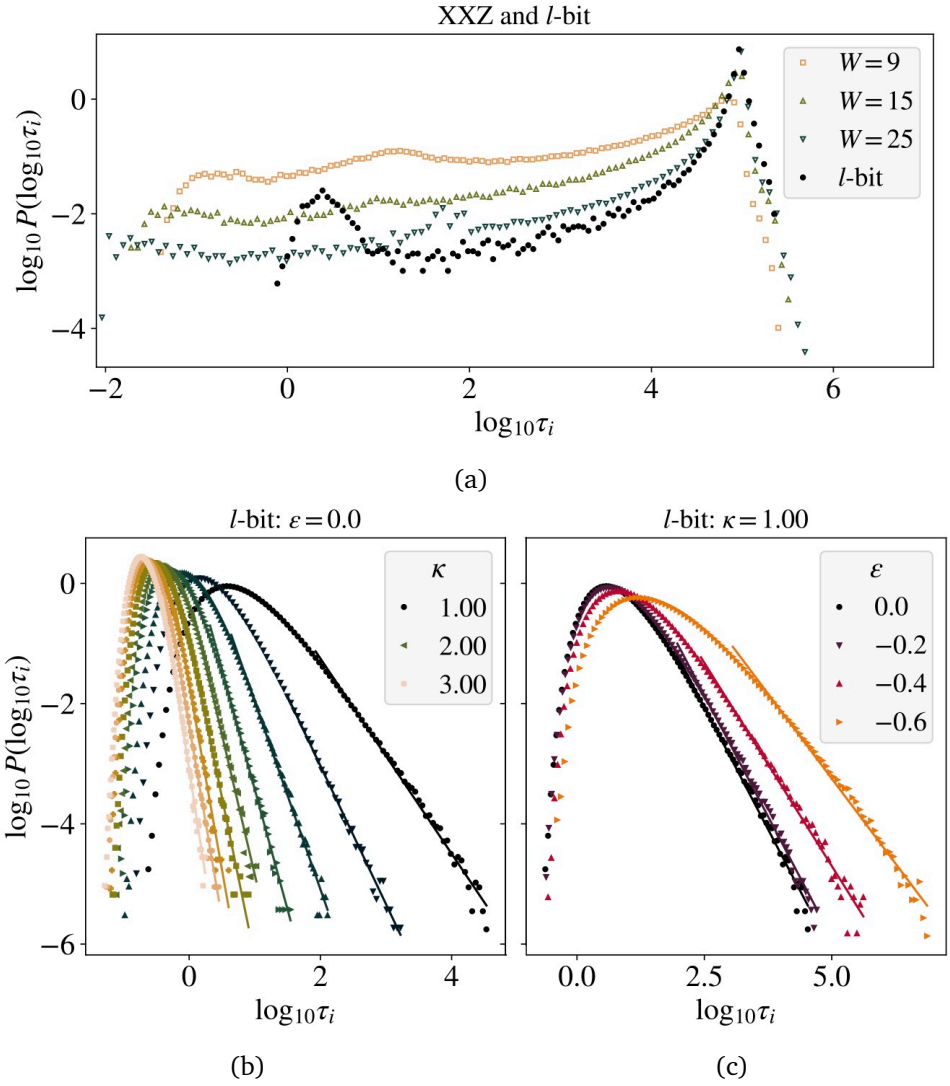

Figure 8.1.: Probability distribution functions of $\log_{10}(\tau_i)$. (a) Results for the XXZ model in Eq. (8.6), for $L = 16$, $t_{\text{fin}} = 10^3$, and various W. We performed the XXZ unitary dynamics using the Krylov technique [296], with dimension of the $M = 40$, and collected data from at least 8000 disorder realizations. For comparison, the l-bit model at $L = 10$, $\kappa = 1$, $\varepsilon = 0$ is shown as well, with empty squares (300 disorder realizations). J_0 has been fixed to make the pdf's maximum coincide with the XXZ ones. More about the XXZ-l-bit correspondence in Appendix D.3. (b)-(c) Results for the l-bit model in Eq. (8.1) at $L = 80$, for various κ and ε. We collected data from at least 4000 disorder realizations, and 20 initial states for each of them. As W increases or, equivalently, κ decreases, the distributions broaden; the same happens when ε decreases. This resembles the phenomenology of dynamical heterogeneities in classical amorphous materials upon approaching the glass transition. We performed power-law fits on the tails of the pdf's for the l-bit model, obtaining the exponents β, whose behavior is shown in Fig. 8.2b.

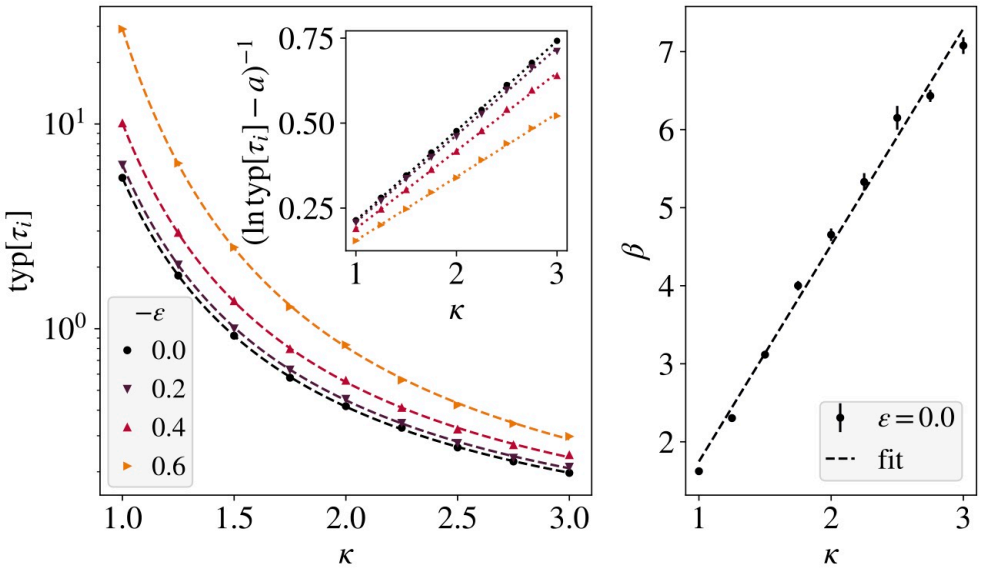

(a) (b)

Figure 8.2.: (a) The typical value of τ_i, defined in the main text, is shown as a function of κ for different ε (dots). The dashed lines are fits with the function $\exp[a + (b\kappa + c)^{-1}]$. From a, we performed the linear fits depicted in the inset: $\ln(\text{typ}[\tau_i] - a)^{-1}$ as a function of κ is found to be linear, as expected (see Appendix D.2). (b) Slope β as a function of κ, obtained from the linear fits of the tails of $\log_{10}(P(\log_{10} \tau_i))$ in Fig. 8.1b. $\beta(\kappa)$ is consistent with a linear behavior; with a linear fit we obtain: $\beta = 2.8(5)\kappa - 1.(2)$.

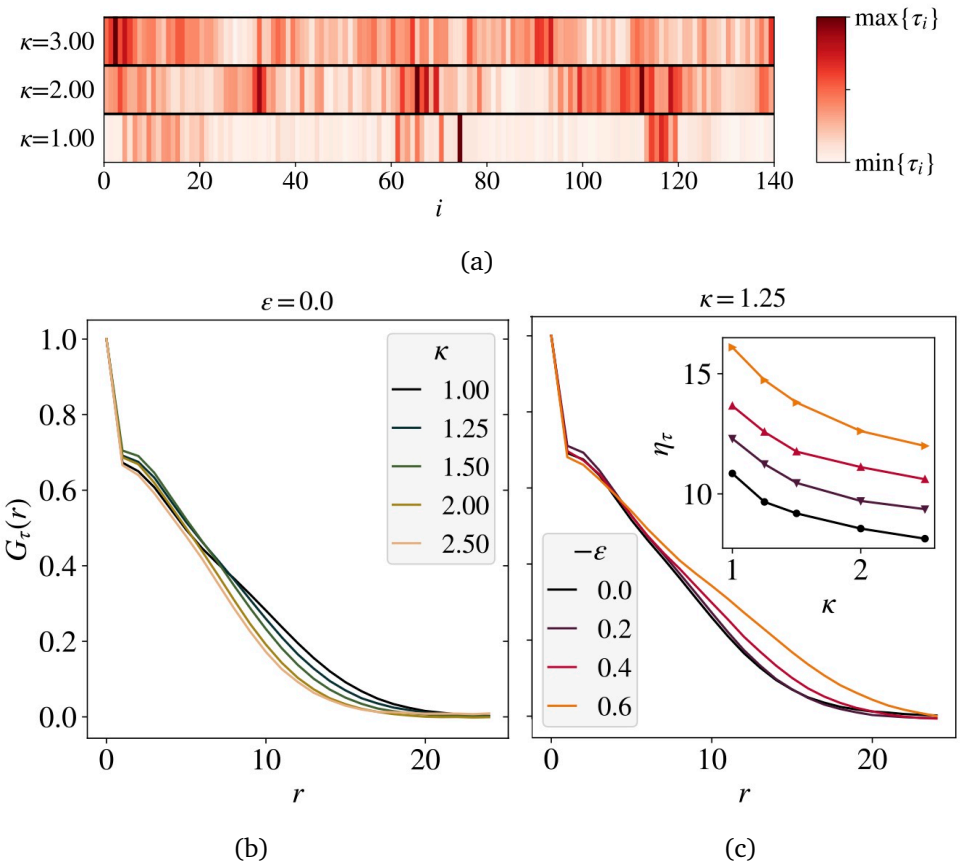

Figure 8.3.: Spatial correlation of the τ_i's in the l-bit model. (a) Snapshot of the spatial distribution of the τ_i's at three different values of κ (in one realization of disorder), showing the emergence of dynamically correlated clusters as the disorder increases. (b)–(c) The correlation function $G_\tau(r)$, defined in Eq. (8.5), for $L = 140$, and various κ and ε. We see that the spatial correlation among τ_i's increases for decreasing κ and ε. $G_\tau(r)$ has been averaged over at least 1000 disorder realizations, and 20 initial states. (Inset of (c)) The dynamical correlation length η_τ, from stretched exponential fits of $G_\tau(r)$, as a function of κ. η_τ decreases as κ increases, indicating that, when disorder augments, increasingly larger clusters of dynamically correlated spins emerge.

9. Concluding remarks

In this thesis, we tackled the long-standing problem of ultra-low temperature anomalies in glasses focusing in particular on the effects of quantum mechanics.

In the first Part of the thesis, we followed a research line that takes its root in mean-field models for glasses. We exploited hard spheres, constraint satisfaction problems, and their jamming transition. We showed that the landscape structure of three-dimensional classical hard spheres at jamming is compatible with the one predicted by the exact solution in the mean-field case, indicating that the jamming critical properties might be universal and independent of the dimension of the system. We also found that the jamming transition in the quantum perceptron model, a simple mean-field model for quantum hard spheres and learning protocols, is sensibly affected by quantum mechanics: the quantum jamming point has critical exponents different from the classical ones. Moreover, it is not confined to the zero-temperature axis: it "dominates" the classical regime, which is recovered only at $T = \infty$. These findings suggest that quantum mechanics might strongly influence also the physics of structural glasses at ultra-low temperatures. This perspective has never been fully considered in the literature before, partly due to the analytical and numerical challenges it posits. However, we expect it to have far-reaching implications.

In the second Part of the thesis, we showed the presence of deep connections between glasses and many-body localized systems. We investigated the quantum dynamics of the two-level system model in glasses. Considering an ensemble of two-level systems coupled with phonons both in the weak- and strong-coupling approximations, we found that their dynamics presents clear signatures of many-body localization physics at short and intermediate time scales. The effects of localization should be experimentally accessible in glassy materials at ultra-low temperatures, using for instance ultra-fast laser probes. The implication of these results is twofold. On the one hand, localization might provide important clues to understand the ultra-low temperature behavior of glasses, and to design new experiments to probe their properties. On the other hand, these findings open up future research directions towards probing many-body localization in real materials. Indeed, the experimental characterization of the many-body localized phase in real materials is still in its infancy, mainly due to the difficulty in finding systems whose microscopic constituents are weakly coupled to thermal baths. In Part II, we also characterized the spatio-temporal properties of entanglement in quantum many-body localized systems. We found that the temporal behavior of local entanglement shows a striking resemblance with dynamical heterogeneities in structural glasses, providing a yet unrecognized connection between the behavior of classical glasses and the genuine quantum dynamics of many-body localized systems. This study suggests that methods and ideas from the theory of glasses might be a useful tool to deepen our knowledge of quantum localization phenomena.

We hope that in the future the results presented here will constitute a useful piece to unveil the complex, intriguing, and fascinating phenomena involving glasses at ultra-low temperatures.

Appendices

A. Appendix to Chapter 4

A.1. A simple variational calculation

In this Section, we sketch a simple variational calculation showing that the presence of quantum mechanics inevitably changes the critical exponents of the jamming transition, in particular the exponent κ regulating the relation $(1-q) \sim (2-\alpha)^{\kappa}$.

Setting $G_n^{-1} = \beta m(\omega_n^2 + \hbar^2/4m^2)/(1-q)$, the spherical constraint (Eq. (4.17)) is automatically satisfied up to exponentially small corrections, and the values of m and q can be fixed by Eqs. (4.16) and (4.18). Notice that there is an equation of the form (4.16) for every $n \in \mathbb{Z}$, yielding a deeply overcomplete set of constraints for our ansatz; however, we restrict only to the case $n = 0$ case.

Setting $x \equiv r/\sqrt{1-q}$ and $H \equiv h/\sqrt{1-q}$, Eq. (4.18) becomes

$$\frac{q}{(1-q)^{3/2}} = \alpha \int \frac{dH}{\sqrt{2\pi q}} e^{-\frac{(1-q)H^2}{2q}} \langle \psi_0^{(H)} | x | \psi_0^{(H)} \rangle^2 , \tag{A.1}$$

and the reduced Schrödinger problem to solve is

$$-\frac{1}{2}\frac{d\psi_k^{(H)}}{dx^2} + \frac{1}{8}x^2 \psi_k^{(H)} = E_k^{(H)} \psi_k^{(H)}, \quad \psi_k^{(H)}(H) = 0. \tag{A.2}$$

Self-consistently, we will show that only the ground-state contribution matters (i.e. $k = 0$). With this in mind, we have employ the one-parameter variational wavefunction

$$\psi^{(H)}(x; L) = \frac{1}{\sqrt{Z}}(x - H)\theta(x - H)e^{-x^2/4L^2}, \tag{A.3}$$

with an appropriate normalization Z, for which the energy reads

$$E^{(H)}(L) = \frac{1 + L^4}{8L^2} \frac{\phi(H/\sqrt{2}L)(H^2 + 3L^2) - 2HL}{\phi(H/\sqrt{2}L)(H^2 + L^2) - 2HL} \tag{A.4}$$

where $\phi(y) \equiv \sqrt{2\pi} e^{y^2} \mathrm{Erfc}(y)$, Erfc being the complementary error function. The equation $dE^{(H)}/dL = 0$ can be solved separately in the regions $H \gg L$, $|H/L| \ll 1$ and $H \ll L$ by using suitable expansions. Remembering that $q \to 1$ (and therefore that the range of $H \sim \sqrt{q/(1-q)} \to \infty$), we see that the important region is $H \gg L$, and self-consistently we obtain $H/L \gg 1$. We find $\langle \psi_0^{(H)} | x | \psi_0^{(H)} \rangle \simeq H + 3^{2/3} H^{-1/3} + O(H^{-5/3})$ and by inserting it in Eq. (A.1) we arrive at

$$q = \alpha \left[(1-q)\xi\left(\frac{q}{1-q}\right) + \frac{q}{2} \right] \tag{A.5}$$

with

$$\xi(\lambda) = \int_0^{\infty} \frac{dH}{\sqrt{2\pi\lambda}} e^{-H^2/2\lambda} \left[\frac{(6H)^{2/3}}{2^{1/3}} + \cdots \right] = \frac{3^{2/3}\Gamma(5/6)}{\sqrt{\pi} 2^{1/3}} \lambda^{1/3} + \cdots . \tag{A.6}$$

Eq. (A.5) can now be solved for q, yielding $\kappa = 3/2$:

$$q = 1 - \frac{\sqrt{2}\,\pi^{3/4}(2-\alpha)^{3/2}}{24\,\Gamma(5/6)^{3/2}}\,. \tag{A.7}$$

The same scaling has been observed by solving the Schrödinger equation (A.2) numerically, discretizing the x-axis and employing imaginary-time evolution to find the ground state.

Knowing q as a function of α, we can now solve the $n = 0$ case of Eq. (4.16) with the same technique. It reads

$$m = \beta\gamma_{q/(1-q)} \star \langle \psi_0^{(H)} | x^2 | \psi_0^{(H)} \rangle^{\text{conn}}\,. \tag{A.8}$$

By means of the same variational ansatz we find that the connected average in the equation above is $3^{1/3}H^{-2/3}\theta(H) + \cdots$, and finally

$$m = \beta \frac{3^{1/3}\Gamma(1/6)}{2^{5/6}} \left(\frac{1-q}{q}\right)^{1/3}\,. \tag{A.9}$$

Thus we see that, as $q \to 1$, $\beta/m \to \infty$ and our approximation to take only the ground state becomes more and more reliable.

B. Appendix to Chapter 6

B.1. Explicit form of interactions and dissipator

We wish to compute explicitly Y_i and J_{ij} defined in Eqs. (6.19) and (6.20), respectively. To do so, we need Γ^{ω}_{ij} defined in Eq. (6.18), that we reproduce here:

$$\Gamma^{\omega}_{ij} := \frac{1}{\hbar^2}\int_0^\infty ds\, e^{i\omega s}\,\mathrm{Tr}_B\left[\rho_B^T\,\hat{E}_i^\dagger(t)\,\hat{E}_j(t-s)\right]. \tag{B.1}$$

Therefore, as a first thing we need to evolve the operators E_i in the interaction picture. Recalling that (Eqs. (6.8) and (6.17))

$$E_j := \xi_{jk}\psi_k + \mathrm{h.c.} = -i\sqrt{\frac{\hbar}{2V\rho\,\omega_k}}\gamma_j D_j^{ab} e_k^{ab} e^{i\mathbf{q}\cdot\mathbf{r}_j}\psi_k + \mathrm{h.c.}, \tag{B.2}$$

it holds

$$\begin{aligned}\hat{E}_i(t) &= e^{iH_{ph}t/\hbar}E_i e^{-iH_{ph}t/\hbar}\\ &= \sum_k \left(\xi_{ik}e^{-i\omega_k t}\psi_k + \xi_{ik}^* e^{i\omega_k t}\psi_k^\dagger\right).\end{aligned} \tag{B.3}$$

Thus, it follows

$$\begin{aligned}\hbar^2\Gamma^{\omega}_{ij} &= \int_0^\infty ds\, e^{i\omega s}\,\mathrm{Tr}_B\left\{\rho_B^T\sum_{kl}\left(\xi_{ik}e^{-i\omega_k t}\psi_k + \mathrm{h.c.}\right)\left(\xi_{jl}e^{-i\omega_l(t-s)}\psi_l + \mathrm{h.c.}\right)\right\}\\ &= \int_0^\infty ds\, e^{i\omega s}\sum_k\left\{\xi_{ik}\xi_{jk}^*\,e^{-i\omega_k s}\,\mathrm{Tr}_B\left[\rho_B^T\psi_k\psi_k^\dagger\right] + \xi_{ik}^*\xi_{jk}\,e^{i\omega_k s}\,\mathrm{Tr}_B\left[\rho_B^T\psi_k^\dagger\psi_k\right]\right\}\\ &= \int_0^\infty ds\, e^{i\omega s}\sum_k\left[\xi_{ik}\xi_{jk}^*\,e^{-i\omega_k s}\left(f_T(\hbar\omega_k)+1\right) + \xi_{ik}^*\xi_{jk}\,e^{i\omega_k s}\,f_T(\hbar\omega_k)\right],\end{aligned} \tag{B.4}$$

where we recall f_T is the Bose-Einstein distribution function at temperature T. We perform the time integral using the identity

$$\int_0^\infty ds\, e^{i\zeta s} = i\,\mathrm{PV}\frac{1}{\zeta} + \pi\delta(\zeta). \tag{B.5}$$

Plugging in the explicit expression of ξ_{ik} from Eqs. (6.8), we arrive at

$$\begin{aligned}\Gamma^{\omega}_{ij} = \frac{\gamma_i\gamma_j}{2\rho}\sum_{abcd}D_i^{ab}D_j^{cd}\sum_s\int\frac{d^3q}{(2\pi)^3}\frac{1}{\hbar\omega_{\mathbf{q}s}}e^{ab}_{\mathbf{q}s}e^{cd}_{\mathbf{q}s}\\ \times\left[\left(f_T(\hbar\omega_{\mathbf{q}s})+1\right)\left(i\mathrm{PV}\frac{1}{\omega-\omega_{\mathbf{q}s}}+\pi\delta(\omega-\omega_{\mathbf{q}s})\right)e^{i\mathbf{q}\cdot(\mathbf{r}_i-\mathbf{r}_j)}\right.\\ \left.+\,f_T(\hbar\omega_{\mathbf{q}s})\left(i\mathrm{PV}\frac{1}{\omega+\omega_{\mathbf{q}s}}+\pi\delta(\omega+\omega_{\mathbf{q}s})\right)e^{-i\mathbf{q}\cdot(\mathbf{r}_i-\mathbf{r}_j)}\right].\end{aligned} \tag{B.6}$$

B.1.1. The dissipation rates

The dissipation rates Y_i can be computed from Eq. (B.6) by taking the real part of Γ^{ω}_{ii} (see Eq. (6.19)):

$$Y_i = \left(\frac{\Delta_i}{\hbar\nu_i}\right)^2 2\,\mathrm{Re}\,\Gamma^{\nu_i}_{ii}\big|_{T=0}. \tag{B.7}$$

Hence, we need to compute (see Eq. (B.6))

$$\mathrm{Re}\,\Gamma^{\omega}_{ii} = \frac{\pi\gamma_i^2}{2\rho}\sum_{abcd} D_i^{ab}D_i^{cd}\sum_s \int \frac{d^3q}{(2\pi)^3}\frac{1}{\hbar\omega_{\mathbf{q}s}}\, e^{ab}_{\mathbf{q}s}e^{cd}_{\mathbf{q}s}\left[(f_T(\hbar\omega_{\mathbf{q}s})+1)\delta(\omega-\omega_{\mathbf{q}s})\right.$$
$$\left. + f_T(\hbar\omega_{\mathbf{q}s})\delta(\omega+\omega_{\mathbf{q}s})\right]. \tag{B.8}$$

One could in principle consider the longitudinal and transverse polarizations separately, however it is convenient to employ an isotropic Debye model with sound velocity

$$\frac{1}{v^3} := \frac{1}{3}\sum_s \frac{1}{v_s^3}. \tag{B.9}$$

Within this assumption, it is convenient to compute the angular averages summing over all polarizations as

$$\frac{1}{4\pi}\sum_{abcd}\sum_s \int d\Omega\, e^{ab}_{\mathbf{q}s}e^{cd}_{\mathbf{q}s}D_i^{ab}D_i^{cd} = \frac{1}{3}\,\mathrm{Tr}(D_i^2)\,q^2, \tag{B.10}$$

where $\mathrm{Tr}(D_i^2) := \sum_{ab} D_i^{ab}D_i^{ba}$. Thus,

$$\mathrm{Re}\,\Gamma^{\omega}_{ii} = \frac{\gamma_i^2\mathrm{Tr}(D_i^2)}{12\pi\rho\hbar v}\int_0^{\infty} dq\, q^3\left[(f_T(\hbar vq)+1)\delta(\omega-vq) + f_T(\hbar vq)\delta(\omega+vq)\right]. \tag{B.11}$$

We know from the theory of the GKSL equation [271, 272] that dissipation and dephasing rates are obtained by setting respectively $\omega = \pm\nu_i, 0$ in Eq. (B.11). However, as argued in the main text we are effectively at zero temperature: $f_{T=0} = 0$, and we are left with only

$$\mathrm{Re}\,\Gamma^{\nu_i}_{ii}\big|_{T=0} = \frac{\gamma_i^2\nu_i^3\mathrm{Tr}(D_i^2)}{12\pi\rho\hbar v^5}. \tag{B.12}$$

Notice in particular that $\Gamma^0_{ii} = 0$ since the phonons have zero density of states at $\omega = 0$. Using Eq. (B.7), we finally arrive at

$$Y_i = \frac{\Delta_i^2\gamma_i^2\nu_i\mathrm{Tr}(D_i^2)}{12\pi\rho\hbar^3v^5}, \tag{B.13}$$

that is exactly Eq. (6.21).

B.1.2. The interaction strengths

From the general considerations reported in the main text (see Sec. 6.2.3 and Fig. 6.1), we know that interactions take place mostly in the S^z–S^z channel. What we need to compute is the coefficient J_{ij} giving the strength of the interaction, and coming from the imaginary part

of Γ^0_{ij} of Eq. (B.6). With hindsight, we note that the temperature-dependent terms will not contribute; therefore, we just need to compute the following quantity:

$$\begin{aligned}\Pi_{ij} &:= -i\left[\Gamma^0_{ij} - \left(\Gamma^0_{ji}\right)^*\right] \\ &= \frac{\gamma_i\gamma_j}{4\rho}\sum_{abcd} D_i^{ab} D_j^{cd} \sum_s \mathrm{PV}\int \frac{d^3q}{(2\pi)^3}\,\frac{1}{\hbar\omega_{\mathbf{q}s}}\,(q^a\hat{e}^b_{\mathbf{q}s} + q^b\hat{e}^a_{\mathbf{q}s})(q^c\hat{e}^d_{\mathbf{q}s} + q^d\hat{e}^c_{\mathbf{q}s})\frac{e^{i\mathbf{q}\cdot(\mathbf{r}_i-\mathbf{r}_j)}}{-\omega_{\mathbf{q}s}}. \end{aligned} \tag{B.14}$$

The interactions J_{ij} are then given by (see Eq. (6.20))

$$J_{ij} = \frac{2\varepsilon_i}{\hbar\nu_i}\frac{2\varepsilon_j}{\hbar\nu_j}\,\frac{\hbar}{2}\,\Pi_{ij}. \tag{B.15}$$

We can proceed as follows: we split the different polarization contributions, then evaluate the angular integrals, and, finally, the $|\mathbf{q}|$ integral. Treating separately the different polarization here is crucial: as will be clear from Eq. (B.27), there is a contribution that vanishes if $v_L = v_T$.

Let us define some quantities that will soon appear in the computation:

$$I^{abcd}(\zeta) := \frac{1}{4\pi}\int d\Omega\,\hat{q}^a\hat{q}^b\hat{q}^c\hat{q}^d e^{i\zeta\cos\theta}, \tag{B.16}$$

$$I^{ab}(\zeta) := \frac{1}{4\pi}\int d\Omega\,\hat{q}^a\hat{q}^b e^{i\zeta\cos\theta}. \tag{B.17}$$

Explicitly, they read:

$$\begin{aligned} I^{xxyy}(\zeta) &= \frac{1}{3}I^{xxxx}(\zeta) = -\frac{3\zeta\cos\zeta + (\zeta^2-3)\sin\zeta}{\zeta^5}, \\ I^{xxzz}(\zeta) &= -\frac{\zeta(\zeta^2-12)\cos\zeta - (5\zeta^2-12)\sin\zeta}{\zeta^5}, \\ I^{zzzz}(\zeta) &= \frac{4\zeta(\zeta^2-6)\cos\zeta + (\zeta^4-12\zeta^2+24)\sin\zeta}{\zeta^5}, \\ I^{xx}(\zeta) &= \frac{-\zeta\cos\zeta + \sin\zeta}{\zeta^3}, \\ I^{zz}(\zeta) &= \frac{2\zeta\cos\zeta + (\zeta^2-2)\sin\zeta}{\zeta^3}. \end{aligned} \tag{B.18}$$

Similar ones are obtained exchanging x and y and permuting the indices; all the others are zero. We can parametrize them as

$$\begin{aligned} I^{abcd}(\zeta) &= \frac{1}{\zeta^5}\sum_{l=0}^{4} C_l^{abcd}\,\zeta^l\,s_l(\zeta), \\ I^{ab}(\zeta) &= \frac{1}{\zeta^3}\sum_{l=0}^{2} C_l^{ab}\,\zeta^l\,s_l(\zeta) \end{aligned} \tag{B.19}$$

where

$$s_l(\zeta) := \begin{cases} \sin\zeta & l \text{ even} \\ \cos\zeta & l \text{ odd}. \end{cases} \tag{B.20}$$

Let us start considering the longitudinally polarized modes. Since $\hat{\mathbf{e}}_{\mathbf{q}L} = \hat{\mathbf{q}}$, we find

$$\left[\Pi_{ij}\right]_L = -\frac{\gamma_i\gamma_j}{\rho}\sum_{abcd} D_i^{ab} D_j^{cd}\,\mathrm{PV}\int\frac{d^3q}{(2\pi)^3}\,\frac{1}{\hbar v_L^2 q^2}\,q^2\hat{q}^a\hat{q}^b\hat{q}^c\hat{q}^d e^{i\mathbf{q}\cdot(\mathbf{r}_i-\mathbf{r}_j)}. \tag{B.21}$$

Setting the $\hat{z}$ axis along $(\mathbf{r}_i - \mathbf{r}_j)$, defining the modulus distance $|\mathbf{r}_i - \mathbf{r}_j| = r_{ij}$ and $\zeta = q r_{ij}$, and using the definition of I^{abcd} in Eq. (B.16) above, we find

$$\begin{aligned}\left[\Pi_{ij}\right]_L &= -\frac{\gamma_i\gamma_j}{2\pi^2\rho\hbar v_L^2}\sum_{abcd} D_i^{ab}D_j^{cd}\,\mathrm{PV}\int dq\, q^2 I^{abcd}(qr_{ij}) \\ &= -\frac{\gamma_i\gamma_j}{2\pi^2\rho\hbar v_L^2 r_{ij}^3}\sum_{l=0}^{4}\left[\sum_{abcd} C_l^{abcd}D_i^{ab}D_j^{cd}\right]\,\mathrm{PV}\int d\zeta\,\zeta^{l-3}s_l(\zeta). \end{aligned} \tag{B.22}$$

One can check that all the IR divergences cancel out (since $C_0^{abcd} = -C_1^{abcd}$), while the UV divergences are harmless thanks to the oscillating functions $s_l(\zeta)$. We find

$$\begin{aligned}\left[\Pi_{ij}\right]_L &= -\frac{\gamma_i\gamma_j}{2\pi^2\rho\hbar v_L^2 r_{ij}^3}\sum_{abcd}\left(\frac{\pi}{4}C_0^{abcd} + \frac{\pi}{2}C_2^{abcd}\right)D_i^{ab}D_j^{cd} \\ &= -\frac{\gamma_i\gamma_j}{8\pi\rho\hbar v_L^2 r_{ij}^3}\sum_{abcd}(C_0^{abcd} + 2C_2^{abcd})D_i^{ab}D_j^{cd}. \end{aligned} \tag{B.23}$$

Now we perform a similar computation for the transversely polarized modes. Using the relation,

$$\sum_{s\ \mathrm{trans.}} \hat{e}^a_{\mathbf{q}s}\hat{e}^b_{\mathbf{q}s} = \delta^{ab} - \hat{q}^a\hat{q}^b, \tag{B.24}$$

we see that there are terms involving I^{ab} (coming from δ^{ab}) and terms involving I^{abcd} (coming form $\hat{q}^a\hat{q}^b$). It is easy to check that the result is

$$\left[\Pi_{ij}\right]_T = -\frac{\gamma_i\gamma_j}{8\pi\rho\hbar v_T^2 r_{ij}^3}\sum_{abcd}(2C_0^{ac}\delta^{bd} - C_0^{abcd} - 2C_2^{abcd})D_i^{ab}D_j^{cd}. \tag{B.25}$$

Summing the longitudinal and transverse contributions in Eqs. (B.23) and (B.25), we finally obtain

$$\Pi_{ij} = \frac{\gamma_i\gamma_j\mathbb{D}_{ij}}{8\pi\rho\hbar v^2 r_{ij}^3} \tag{B.26}$$

having defined

$$\mathbb{D}_{ij} := v^2\sum_{abcd}\left[-\frac{2C_0^{ac}\delta^{bd}}{v_T^2} + (C_0^{abcd} + 2C_2^{abcd})\left(\frac{1}{v_T^2} - \frac{1}{v_L^2}\right)\right]D_i^{ab}D_j^{cd}, \tag{B.27}$$

where v is the average velocity defined in Eq. (B.9). Despite the cumbersome appearance, $\mathbb{D}_{ij}$ are dimensionless random variables with zero average and standard deviation of order 1. Finally, by means of Eq. (B.15):

$$J_{ij} = \frac{\gamma_i\varepsilon_i}{\hbar\nu_i}\frac{\gamma_j\varepsilon_j}{\hbar\nu_j}\frac{\mathbb{D}_{ij}}{4\pi\rho v^2 r_{ij}^3}, \tag{B.28}$$

that is Eq. (6.22) of the main text.

B.2. Two-site observables within the diagonal unitary evolution

In this Section, we show how to compute with $O(N)$ steps the two-site density matrix ρ_{ij}, and therefore any two-site observable, for the Hamiltonian (6.23). Call the initial density

matrix

$$\rho_0 = \bigotimes_{i=1}^{N} \rho_{0,i} = \bigotimes_{i=1}^{N} \sum_{s_i,s_i'} \rho_{0,i}^{s_i s_i'} |s_i\rangle \langle s_i'| , \tag{B.29}$$

and recall that the Hamiltonian (6.23) reads explicitly

$$H_{TLS} + H_{LS} = -\frac{1}{2}\sum_i \hbar\nu_i S_i^z + \sum_{ij} J_{ij} S_i^z S_j^z .$$

Time evolving the density matrix according to the von Neumann equation and rearranging the sum, one finds

$$\rho(t) = \sum_{s,s'} \prod_i \rho_{0,i}^{s_i s_i'} |s\rangle \langle s'| \, e^{-i(H[s]-H[s'])t/\hbar} \tag{B.30}$$

with $H[s] = -\frac{1}{2}\sum_i \hbar\nu_i s_i + \sum_{ij} J_{ij} s_i s_j$, where $s_i = \pm 1$ is the projection of the spin-1/2 on the z axis. Without loss of generality, we can trace out all the spins but the first two. The matrix elements of the two-site reduced density matrix read

$$\begin{aligned}
\langle s_1 s_2| \, \rho_{12}(t) \, |s_1' s_2'\rangle &= \langle s_1 s_2| \, \mathrm{Tr}_{3\cdots N} \, \rho(t) \, |s_1' s_2'\rangle \\
&= \sum_{s_3 \cdots s_N} \rho_{0,1}^{s_1,s_1'} \rho_{0,2}^{s_2,s_2'} \rho_{0,3}^{s_3,s_3} \cdots \rho_{0,N}^{s_N,s_N} e^{-i(H[s_1 s_2 s_3 \cdots s_N] - H[s_1' s_2' s_3 \cdots s_N])t/\hbar} \\
&= \rho_{0,1}^{s_1,s_1'} \rho_{0,2}^{s_2,s_2'} e^{-i\Delta H_{12}[s]t/\hbar} \prod_{j=3}^{N} \left[\rho_{0,j}^{\uparrow,\uparrow} e^{-i\Delta H_{12j}[s]t/\hbar} + \rho_{0,j}^{\downarrow,\downarrow} e^{i\Delta H_{12j}[s]t/\hbar} \right],
\end{aligned} \tag{B.31}$$

having defined

$$\begin{aligned}
\Delta H_{12}[s] &:= 2J_{12}(s_1 s_2 - s_1' s_2') - \frac{\hbar\nu_1}{2}(s_1 - s_1') - \frac{\hbar\nu_2}{2}(s_2 - s_2'), \\
\Delta H_{12j}[s] &:= 2J_{1j}(s_1 - s_1') + 2J_{2j}(s_2 - s_2').
\end{aligned} \tag{B.32}$$

From the knowledge of ρ_{ij}, the concurrence follows by using Eq. (5.5).

Notice that an analogue procedure gives the k-site reduced density matrix with $O(k^2 N)$ steps. Thus, this computation allows to access few-sites observables for large system sizes.

B.3. Concurrence in a random state

Let us consider a system of N spin-1/2. A random, uniformly distributed state is $|\psi\rangle = U|\psi_0\rangle$, U being a Haar-random unitary, and $|\psi_0\rangle$ a reference state. Equivalently, a random state is $|\psi\rangle = \sum_{\{s\}} A_{\{s\}} |\{s\}\rangle$, with the coefficients $A_{\{s\}}$ being uniformly distributed over $\mathbb{C}P^{M-1}$, with $M = 2^N$.

The concurrence of two spins, say sites 1 and 2 wlog., follows from the knowledge of the square roots of the eigenvalues of the matrix $R_{12} = \rho_{12}(\sigma_y \otimes \sigma_y)\rho_{12}^*(\sigma_y \otimes \sigma_y)$. The exact determination of such eigenvalues has evaded our analytical attempts, but we can give an heuristic argument that captures the scaling with N. Consider, instead of the square roots of

the eigenvalues of R_{12}, directly the eigenvalues λ_a of ρ_{12}. Classical works [297, 298] give us their probability density function:

$$p(\lambda_1,\lambda_2,\lambda_3,\lambda_4) \propto \delta\Big(1-\sum_{a=1}^{4}\lambda_a\Big)\prod_{a=1}^{4}\lambda_a^{M-4}\prod_{a<b}(\lambda_a-\lambda_b)^2 \tag{B.33}$$

with the constraint $\lambda_a > 0$, $a = 1,\dots,4$. With hindsight, we perform the change of variables

$$\rho_{12} \equiv \frac{1}{4}\mathrm{Id} + \frac{1}{4\sqrt{M-4}}\tau_{12}, \qquad \lambda_a \equiv \frac{1}{4} + \frac{\mu_a}{4\sqrt{M-4}}, \tag{B.34}$$

so that

$$\begin{aligned} p(\mu_1,\mu_2,\mu_3,\mu_4) &\propto \delta\Big(\sum_{a=1}^{4}\mu_a\Big)\prod_{a=1}^{4}\left(1+\frac{\mu_a}{\sqrt{M-4}}\right)^{M-4}\prod_{a<b}(\mu_a-\mu_b)^2 \\ &\propto \delta\Big(\sum_{a=1}^{4}\mu_a\Big)\exp\left[-\frac{1}{2}\sum_a\mu_a^2+O\left(\frac{1}{\sqrt{M-4}}\right)\right]\prod_{a<b}(\mu_a-\mu_b)^2. \end{aligned} \tag{B.35}$$

We see that, at this order, we can let μ_a range from $-\infty$ to $+\infty$ if N is big enough.

At this point we note that not only the eigenvalues of τ_{12}, but every entry of the matrix is at most of order 1 because of our rescaling. This enables us to expand

$$\begin{aligned} \sqrt{R_{12}} &= \left[\frac{1}{16}\mathrm{Id}+\frac{1}{16\sqrt{M-4}}\left[\tau_{12}+(\sigma_y\otimes\sigma_y)\tau_{12}^*(\sigma_y\otimes\sigma_y)\right]+O\left(\frac{1}{M}\right)\right]^{1/2} \\ &= \frac{1}{4}\mathrm{Id}+\frac{1}{8\sqrt{M-4}}\left[\tau_{12}+(\sigma_y\otimes\sigma_y)\tau_{12}^*(\sigma_y\otimes\sigma_y)\right]+O\left(\frac{1}{M}\right) \end{aligned} \tag{B.36}$$

The matrix $\frac{1}{2}[\tau_{12}+(\sigma_y\otimes\sigma_y)\tau_{12}^*(\sigma_y\otimes\sigma_y)]$ is traceless and very roughly its eigenvalues will have a joint probability density function very similar to that of τ_{12}. For this reason, we can approximate the average concurrence with

$$\langle C\rangle \approx \int d\vec{\mu}\, p(\vec{\mu})\, \max\left\{0, \frac{2\mu_1-1}{4\sqrt{M-4}}-\frac{1}{2}\right\}, \tag{B.37}$$

where we have used the δ-function constraint and called μ_1 the largest eigenvalue. Integrating only on μ_1, and forgetting the presence of μ_2, μ_3, μ_4 (otherwise the integration becomes rather cumbersome), we find

$$\langle C\rangle \approx \frac{e^{-(M+\sqrt{M-4})/2}}{2\sqrt{2\pi}(M-4)^{3/2}}, \tag{B.38}$$

from which

$$\log_2\big(-\log\langle C\rangle\big) \approx \log(a)+bN+\cdots \tag{B.39}$$

with $a = 1/2$ and $b = 1$. As can be seen from Figure B.1, this scaling is correct, but the numerical factor a is different.

B.4. Integration of the GKSL master equation

The density matrix of the system can be parametrized as

$$\rho(t) = \sum_{\mu_1\cdots\mu_N} C_{\mu_1\cdots\mu_N}(t) S_1^{\mu_1}\otimes\cdots\otimes S_N^{\mu_N}, \tag{B.40}$$

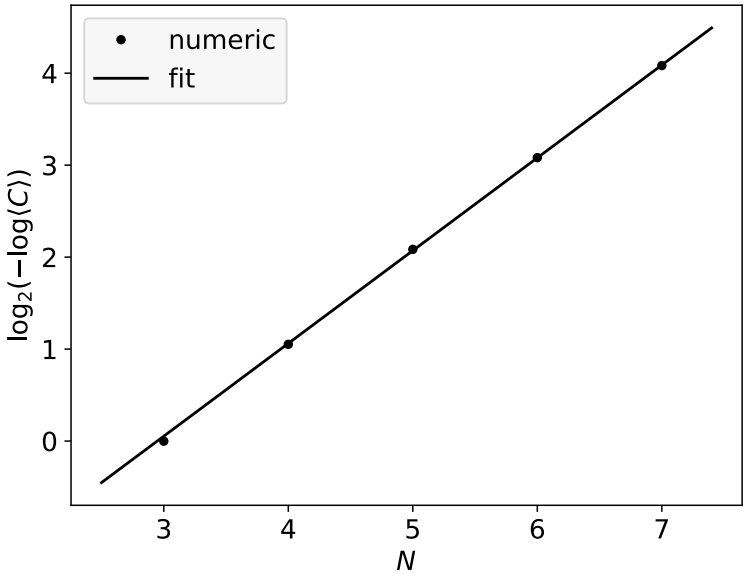

Figure B.1.: The average concurrence in a random state follows the scaling $\langle C\rangle \sim e^{-a2^{bN}}$. The dots show the concurrence averaged over 10^7 randomly generated states, and over every couple of spins for each state. A linear fit is shown for comparison: $b = 1.009(6)$, but $a = 0.127(3)$, differing from $a = 1/2$ found analytically (Eq. (B.39)).

where $S_i^{\mu_i} \in \{\mathrm{Id}_i, S_i^+, S_i^-, S_i^z\}$. Writing explicitly the GKSL equation (see Eqs. (6.15) and (6.23) in the main text), we get

$$\begin{aligned}\partial_t\rho(t) = -\frac{i}{\hbar}\Big[-\sum_i \frac{\hbar\nu_i}{2}S_i^z + \sum_{ij} J_{ij}S_i^zS_j^z,\ \rho(t)\Big] \\ + \sum_i Y_i f_T(\hbar\nu_i)\left[S_i^+\rho(t)S_i^- + S_i^-\rho(t)S_i^+ - 4\rho(t)\right] \\ + \sum_i Y_i\left[S_i^+\rho(t)S_i^- + \{\rho(t), S_i^z\} - 2\rho(t)\right].\end{aligned} \tag{B.41}$$

In the absence of the interactions (i.e. ignoring the term $\sum_{ij} J_{ij}S_i^zS_j^z$), the evolution can be easily computed, and the density matrix evolves as

$$\partial_t C_{\mu_1\cdots\mu_N} = \Big[\sum_i \lambda_i^{\mu_i}\Big]C_{\mu_1\cdots\mu_N} + \sum_i 4Y_i\ \delta^{\mu_i z}C_{\mu_1\cdots 0_i\cdots\mu_N}, \tag{B.42}$$

where the $\delta^{\mu_i z}$ are Kronecker deltas, the $\lambda_i^{\mu_i}$'s are given by

$$\lambda_i^z = -4Y_i(1+2f_T), \qquad \lambda_i^\pm = \frac{1}{2}\lambda_i^z \pm i\nu_i, \tag{B.43}$$

and $\lambda_i^0 = 0$. When interactions are suppressed, the TLSs evolve independently one from the other and any factorized initial state will remain such at all times. One has

$$\rho(t) = \bigotimes_{i=1}^N \sum_{\mu_i} P_i^{\mu_i}(t)S_i^{\mu_i} \implies C_{\mu_1\cdots\mu_N}(t) = P_1^{\mu_1}(t)\cdots P_N^{\mu_N}(t) \quad \forall t. \tag{B.44}$$

The interactions among TLSs make the evolution more complicated. Computing the commutator

$$\begin{aligned}\left[S_i^z S_j^z, S_i^{\mu_i} S_j^{\mu_j}\right] &= S_i^z S_i^{\mu_i}\left[S_j^z, S_j^{\mu_j}\right] + \left[S_i^z, S_i^{\mu_i}\right] S_j^{\mu_j} S_j^z \\ &= 2\sum_{\mu_i'\mu_j'}\big[(\delta^{\mu_i 0}\delta^{\mu_i' z} + \delta^{\mu_i z}\delta^{\mu_i' 0} + \delta^{\mu_i +}\delta^{\mu_i' +} - \delta^{\mu_i -}\delta^{\mu_i' -})(\delta^{\mu_j +}\delta^{\mu_j' +} - \delta^{\mu_j -}\delta^{\mu_j' -}) \\ &+ (\delta^{\mu_j 0}\delta^{\mu_j' z} + \delta^{\mu_j z}\delta^{\mu_j' 0} - \delta^{\mu_j +}\delta^{\mu_j' +} + \delta^{\mu_j -}\delta^{\mu_j' -})(\delta^{\mu_i +}\delta^{\mu_i' +} - \delta^{\mu_i -}\delta^{\mu_i' -})\big] S_i^{\mu_i'} S_j^{\mu_j'}, \end{aligned} \tag{B.45}$$

and defining

$$\zeta^{\mu\mu'} := \delta^{\mu 0}\delta^{\mu' 3} + \delta^{\mu 3}\delta^{\mu' 0}, \qquad \kappa^{\mu\mu'} := 2\delta^{\mu +}\delta^{\mu' +} - 2\delta^{\mu -}\delta^{\mu' -}, \tag{B.46}$$

one arrives at

$$\sum_{i\neq j} J_{ij}\left[S_i^z S_j^z, S_i^{\mu_i} S_j^{\mu_j}\right] = 2\sum_{i<j} J_{ij}\sum_{\mu_i'\mu_j'}\left[\zeta^{\mu_i\mu_i'}\kappa^{\mu_j\mu_j'} + (i\leftrightarrow j)\right] S_i^{\mu_i'} S_j^{\mu_j'}. \tag{B.47}$$

The full evolution of the density matrix is given by

$$\begin{aligned}\partial_t C_{\mu_1\cdots\mu_N} = &\sum_i \lambda_i^{\mu_i} C_{\mu_1\cdots\mu_N} + \sum_i 4Y_i\ \delta^{\mu_i z} C_{\mu_1\cdots 0_i\cdots\mu_N} \\ &- \frac{2i}{\hbar}\sum_{i<j} J_{ij}\sum_{\mu_i'\mu_j'}\left(\zeta^{\mu_i\mu_i'}\kappa^{\mu_j\mu_j'} + \kappa^{\mu_i\mu_i'}\zeta^{\mu_j\mu_j'}\right) C_{\mu_1\cdots\mu_i'\cdots\mu_j'\cdots\mu_N}. \end{aligned} \tag{B.48}$$

This is a systems of 4^N partial differential equations. We solved it by matrix exponentiation, using the library for linear algebra with sparse matrices contained in `SciPy(Python)`.

C. Appendix to Chapter 7

C.1. Estimate of the dipole tensor

As discussed in Section 7.1, we consider the dipole tensor D_i^{ab} as the difference between two random dipoles, one for each well of the TLS, according to Ref. [41]:

$$D_i = \frac{1}{2}\left(D_i^{(l)} - D_i^{(r)}\right). \tag{C.1}$$

Both $D_i^{(l)}$ and $D_i^{(r)}$ are assumed to be vector dipoles oriented in two random directions:

$$D_i^{(l,r)} = \delta\,[O^{(l,r)}]^T \begin{pmatrix} 0 & 0 & 0 \\ 0 & 0 & 0 \\ 0 & 0 & 1 \end{pmatrix} O^{(l,r)} \tag{C.2}$$

where $O^{(l)}$,$O^{(r)}$ are two Haar-random orthogonal matrices, and δ is a dimensionless number that needs to be fixed to match experiments and simulations. In Ref. [41], it has been argued that

$$[\gamma D_i]_{max} \approx 8\left(\frac{2\pi^2}{9}\right)^{2/3}\frac{\rho v^2}{q_D^3} \tag{C.3}$$

where $q_D = \frac{k_B T_D}{\hbar v}$, and v is the average over polarizations of the sound velocity (see Eq. (B.9)). For D_i given in Eqs. (C.1)–(C.2), we find that

$$[D_i]_{max} = \max\left(\frac{\mathrm{Tr}(D_i^2)}{3}\right)^{1/2} = \frac{\delta}{\sqrt{6}}. \tag{C.4}$$

Therefore, fixing γ from Table 6.1, we obtain: $\delta_{\mathrm{SiO_2}} \approx 8.46$, $\delta_{\mathrm{BK7}} \approx 9.34$, and $\delta_{\mathrm{PMMA}} \approx 6.42$. Fig. C.1 shows the resulting distributions of the dipole contractions $\mathrm{Tr}(D_i^2)/\delta^2$, given by

$$\mathrm{Tr}(D_i^2) := \sum_{ab} D_i^{ab} D_i^{ba}, \tag{C.5}$$

and $\mathbb{D}_{ij}/\delta^2$, given by (same definition given in Eq. (B.27))

$$\mathbb{D}_{ij} := v^2 \sum_{abcd}\left[-\frac{2C_0^{ac}\delta^{bd}}{v_T^2} + (C_0^{abcd} + 2C_2^{abcd})\left(\frac{1}{v_T^2} - \frac{1}{v_L^2}\right)\right] D_i^{ab} D_j^{cd}. \tag{C.6}$$

with C_0^{ab}, C_0^{abcd}, C_2^{abcd} defined in Eqs. (B.18)–(B.20).

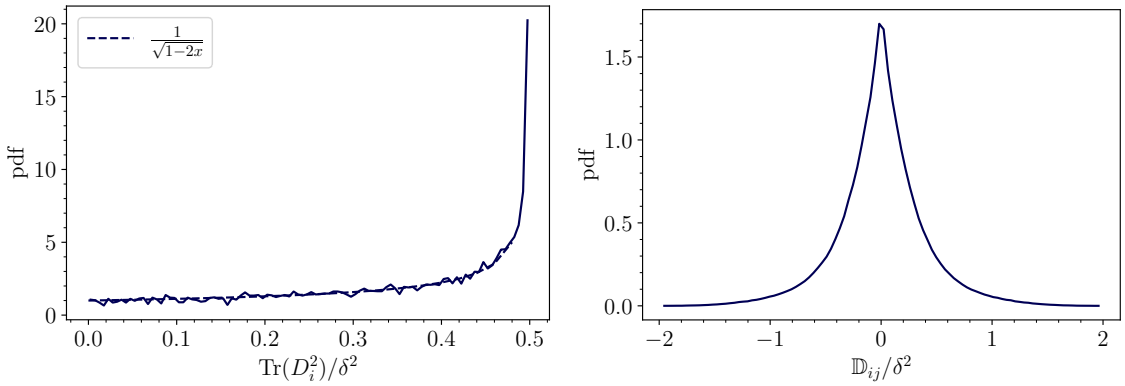

(a) (b)

Figure C.1.: (a) The distribution of $x := \mathrm{Tr}(D_i^2)/\delta^2$ is given by $p(x) = (1-2x)^{-1/2}$ (see also Ref. [41]). (b) Distribution of $\mathbb{D}_{ij}/\delta^2$, where $\mathbb{D}_{ij}$ is defined in Eq. (C.6). The distribution is sampled using D_i^{ab} of the form specified in Eqs. (C.1)-(C.2).

C.2. Computation of the Debye-Waller factor

In this Appendix, we compute explicitly the Debye-Waller factor of Eq. (7.17):

$$\frac{\Gamma_i^2}{2} = \gamma^2 \sum_{\mathbf{q}s} \frac{1}{\hbar\omega_{\mathbf{q}s}^3} \Xi_{i\mathbf{q}s}\Xi_{i\mathbf{q}s}^* \coth\left(\frac{\beta\hbar\omega_{\mathbf{q}s}}{2}\right) \tag{C.7}$$

$$= \frac{\gamma^2}{\rho\hbar} \sum_{abcd}\sum_{s} \int \frac{d^3q}{(2\pi)^3} \frac{1}{\omega_{\mathbf{q}s}^3} D_i^{ab} D_i^{cd} e_{\mathbf{q}s}^{ab} e_{\mathbf{q}s}^{cd} \coth\left(\frac{\beta\hbar\omega_{\mathbf{q}s}}{2}\right). \tag{C.8}$$

We can compute the angular average as in Eq. (B.10):

$$\frac{1}{4\pi}\sum_{abcd}\sum_{s}\int d\Omega\, e_{\mathbf{q}s}^{ab} e_{\mathbf{q}s}^{cd} D_i^{ab} D_i^{cd} = \frac{1}{3}\mathrm{Tr}(D_i^2)\, q^2, \tag{C.9}$$

and we find

$$\frac{\Gamma_i^2}{2} = \frac{\gamma^2 \mathrm{Tr}(D_i^2)}{6\pi^2\rho\hbar v^3} \int_0^{q_D} dq\, q \coth\left(\frac{\beta\hbar v q}{2}\right), \tag{C.10}$$

where q_D is the Debye wavevector which can be expressed in terms of a real-space UV cutoff a: $q_D = \sqrt[3]{6\pi^2}/a$. The previous is a well-known, condensed-matter-textbook integral, that is usually considered in the two regimes of low and high temperature [299]. In the end, one finds

$$\frac{\Gamma_i^2}{2} = \frac{\gamma^2 q_D^2 \mathrm{Tr}(D_i^2)}{6\pi^2\rho\hbar v^3} \mathcal{F}\left(\frac{\beta\hbar v q_D}{2}\right) \tag{C.11}$$

with

$$\mathcal{F}(w) := \int_0^1 d\zeta\, \zeta \coth(\zeta w) = -\frac{1}{2w^2}\mathrm{Li}_2(e^{-2w}) + \frac{1}{w}\log(1-e^{-2w}) + \frac{\pi^2}{12w^2} + \frac{1}{2}. \tag{C.12}$$

A more manageable expression can be found by using

$$\mathcal{F}(w) = \begin{cases} 1/w + O(w) & w \ll 1 \\ 1/2 + O(e^{-w}) & w \gg 1 \end{cases} \tag{C.13}$$

Considering that $w = \beta\hbar v q_D/2 = T_D/2T$, we note that high and low temperature regimes are defined with respect to $T_D/2$. Thus, in the limit of small temperature $T \gg T_D/2$, we can approximate $\mathcal{F} \approx 1/2$, and find

$$\frac{\Gamma_i^2}{2} = \frac{\gamma^2 q_D^2 \mathrm{Tr}(D_i^2)}{12\pi^2\rho\hbar v^3} + O\big(e^{-T_D/2T}\big). \tag{C.14}$$

We can rewrite the previous expression as

$$\frac{\Gamma_i^2}{2} = \frac{E_D^2}{4E_i^2} + O\big(e^{-T_D/2T}\big). \tag{C.15}$$

where $E_D := k_B T_D$ is the Debye energy and E_i is given in Eq. (7.20), that we reproduce here for readability:

$$E_i := \sqrt{\frac{3\pi^2\hbar^3\rho v^5}{\gamma^2 \mathrm{Tr}(D_i^2)}}. \tag{C.16}$$

The value of Γ_i^2 depends on the random variable $\mathrm{Tr}(D_i^2)$, whose distribution is shown in Fig. C.1a.

C.3. Fermi's golden rule computation

In this Section, by means of the Fermi's golden rule we estimate the decay rate of a TLS into phonons, namely Y_i of Eq. (7.30), reproduced here for readability:

$$Y_i = \sum_f \frac{2\pi}{\hbar} \left| \langle f, \downarrow | \, \overline{\Delta}_i \sigma_i^- e^{i\Gamma_{i,0}\tilde{b}_i^\dagger} e^{-i\Gamma_{i,0}\tilde{b}_i} \, |0, \uparrow\rangle \right|^2 \rho_f(2\epsilon_i)$$

Let us separate the contributions $Y_i^{(n)}$ coming from final states with a fixed number n of phonons. Thus, we sum over all the n-phonon configurations allowed by energy conservation:

$$\frac{1}{V^n}\sum_f = \frac{1}{n!}\sum_{s_1\cdots s_n}\int \frac{d^3q_1}{(2\pi)^3}\cdots\frac{d^3q_n}{(2\pi)^3}\delta\left(2\epsilon_i - \sum_k \hbar\omega_{\mathbf{q}_k s_k}\right), \tag{C.17}$$

where $n!$ comes from the fact that the n bosons in the final state are indistinguishable. The matrix element is instead formed by two contributions:

$$\left| \, \langle\downarrow| \, \overline{\Delta}_i \sigma_i^- \, |\uparrow\rangle \, \right|^2 = \overline{\Delta}_i^2. \tag{C.18}$$

for the TLSs, and

$$\left| \, \langle \mathbf{q}_1 s_1, \cdots, \mathbf{q}_n s_n | \, e^{i\Gamma_{i,0}\tilde{b}_i^\dagger} \, |0\rangle \, \right|^2 = \prod_{k=1}^n \left[\frac{2\gamma^2}{\hbar\omega^3_{\mathbf{q}_k s_k}} |\Xi_{i\mathbf{q}_k s_k}|^2 \right] \tag{C.19}$$

for the phonons. Notice that we are not considering the case in which $q_k = q_{k'}$ for some $k \neq k'$, since it is subleading. Hence, we find

$$Y_i^{(n)} = \frac{2\pi V^n}{\hbar n!}\sum_{s_1\cdots s_n}\int \frac{d^3q_1}{(2\pi)^3}\cdots\frac{d^3q_n}{(2\pi)^3}\,\overline{\Delta}_i^2 \prod_{k=1}^n \left[\frac{2\gamma^2}{\hbar\omega^3_{\mathbf{q}_k s_k}} |\Xi_{i\mathbf{q}_k s_k}|^2 \right] \delta\left(2\epsilon_i - \sum_k \hbar\omega_{\mathbf{q}s}\right) \tag{C.20}$$

We now exponentiate the δ-function via Laplace transform:

$$\widetilde{Y}_i^{(n)}(\lambda) = \int_0^\infty d\epsilon\, e^{-2\lambda\epsilon}\, Y_i^{(n)}(2\epsilon). \tag{C.21}$$

In this way, all the q integrals are factorized, and similar to ones already computed for the Debye-Waller factor in Appendix C.2. We find

$$\frac{2\gamma^2}{\hbar\rho}\sum_{abcd}\sum_s \int \frac{d^3q}{(2\pi)^3}\frac{1}{\omega_{\mathbf{q}s}^3} e^{-\lambda\hbar\omega_{\mathbf{q}s}} D_i^{ab} D_i^{cd} e_{\mathbf{q}s}^{ab} e_{\mathbf{q}s}^{cd} = \frac{\gamma^2 \mathrm{Tr}(D_i^2)}{3\pi^2\hbar\rho v^3}\int_0^\infty dq\, q\, e^{-\eta q - \lambda\hbar v q} \tag{C.22}$$

$$= \frac{\gamma^2 \mathrm{Tr}(D_i^2)}{3\pi^2\hbar\rho v^3}\frac{1}{(\eta+\lambda\hbar v)^2} \tag{C.23}$$

having employed an exponential cutoff $\eta \approx 1/q_D$. Thus, we find that the Laplace-transformed rate is[1]

$$\widetilde{Y}_i^{(n)}(\lambda) = \frac{2\pi\overline{\Delta}_i^2}{\hbar n!}\left[\frac{\gamma^2\mathrm{Tr}(D_i^2)}{3\pi^2\hbar\rho v^3}\frac{1}{(\eta+\lambda\hbar v)^2}\right]^n, \tag{C.24}$$

The inverse Laplace transform is

$$\int_{-i\infty}^{+i\infty}\frac{d\lambda}{2\pi i}\frac{e^{2\lambda\epsilon}}{(\eta+\lambda\hbar v)^{2n}} = \frac{(2\epsilon)^{2n-1}e^{-2\eta\epsilon/\hbar v}}{(\hbar v)^{2n}(2n-1)!}. \tag{C.25}$$

Hence,

$$Y_i^{(n)} = \frac{\pi\overline{\Delta}_i^2 e^{-2\eta\epsilon_i/\hbar v}}{\hbar\epsilon_i n!(2n-1)!}\left[\frac{\gamma^2\epsilon_i^2\mathrm{Tr}(D_i^2)}{3\pi^2\hbar^3\rho v^5}\right]^n. \tag{C.26}$$

Summing all the n-phonon contributions, one has the series

$$\sum_{n\geq 1}\frac{w^n}{n!(2n-1)!} = w\,{}_pF_q\left(;\frac{3}{2},2;\frac{w}{4}\right), \tag{C.27}$$

where ${}_pF_q$ is a generalized hypergeometric function, with asymptotics

$$w\,{}_pF_q\left(;\frac{3}{2},2;\frac{w}{4}\right) = \begin{cases} w + \dfrac{w^2}{12} + O(w^3) & w \ll 1 \\ \exp\left(\dfrac{3w^{1/3}}{4^{1/3}}\right)\left[\dfrac{w^{1/6}}{2^{1/3}\sqrt{3\pi}} + O(w^{-1/6})\right] & w \gg 1. \end{cases} \tag{C.28}$$

Therefore, the final result is

$$Y_i = \sum_{n\geq 1} Y_i^{(n)} = \frac{\pi\overline{\Delta}_i^2\epsilon_i e^{-2\eta\epsilon_i/\hbar v}}{\hbar E_i^2}\,{}_pF_q\left(;\frac{3}{2},2;\frac{\epsilon_i^2}{4E_i^2}\right) \tag{C.29}$$

with E_i given in Eq. (C.16).

[1] Notice that V^n is cancelled by the $1/V^n$ coming from the product of $|\Xi_{i\mathbf{q}_\mathbf{k}s_k}|^2$ in Eq. (C.20).

D. Appendix to Chapter 8

D.1. Energy of the initial states

In the l-bit model in Eq. (8.1), given a disorder realization $\{J_{ij}\}$, we sample the local magnetization configurations $\{m_i\} = \{\langle\sigma_i^z\rangle\}$ with probability $\propto e^{-E/T}$, T being a fictitious temperature to be gradually lowered. Since $m_i \in [-1, 1]$ are continuous variables, the annealing procedure has easy access to states down to the edge of the spectrum. From $\{m_i\}$, we fix the coefficients in Eq. (8.2) as $A_i = \sqrt{(1+m_i)/2}$, and $B_i = e^{i\phi_i}\sqrt{(1-m_i)/2}$. This choice guarantees that $\langle\psi_0|H_{l\text{-bit}}|\psi_0\rangle = E$, i.e., the quantum initial state has an energy expectation value equal to the desired one.

For what concerns our choice of the energy scale, namely

$$\varepsilon := \frac{E}{N\sqrt{h^2/3 + 2J_0^2/(e^{2/\kappa}-1)}} \tag{D.1}$$

(see also the the main text), the reasoning goes as follows. The Hamiltonian in Eq. (8.1) can be interpreted as a *classical* spin glass, if one substitutes $\sigma_i^z \longrightarrow s_i = \pm 1$. Then, one can compute the (annealed) density of states of the model, finding that with high probability the ground state is at $E = -N\sqrt{h^2/4 + 4J_0^2/(e^{2/\kappa}-1)}$ (see also Ref. [294]). Changing the spins to *continuous* variables $\sigma_i^z \longrightarrow m_i \in [-1, 1]$ will just modify the prefactors of h^2 and $J_0^2/(e^{2/\kappa}-1)$, without changing much the scale. For this reason, we have chosen to put in Eq. (D.1) simply the sum of the variances of h_i and $\sum_j J_{ij}$. The ground state will not be exactly at $\varepsilon = -1$, but close to it.

D.2. Analytical estimates of local time scales

Let us consider the l-bit model. Throughout this study, we were concerned in computing the "one-site concurrence" $C_i(t) = \sum_j C_{ij}(t)$, Eq. (8.3), to see how it decayed in time. The concurrence is a complicated non-linear function of the two-site reduced density matrix $\rho_{i,j}$, therefore it is really hard to make analytical predictions for it. However, one can hope to get a rough estimate of its behavior by considering instead the correlation function $\langle\sigma_i^x(t)\sigma_j^x(t)\rangle$. This type of correlation functions were already considered in previous works (see e.g. Ref. [233]), and are easy to access. Choosing $i = 0$ and $j = 1$ without loss of generality, it explicitly reads

$$\begin{aligned}\left\langle\sigma_0^x(t)\sigma_1^x(t)\right\rangle = \sum_{s_0,s_1=\pm1} (\rho_{0,0})_{s_0,-s_0}(\rho_{0,1})_{s_1,-s_1} e^{-2ih_1 s_0 t - 2ih_2 s_1 t + 8iJ_{01}s_0 s_1 t} \\ \times \prod_{j\neq 0,1}\left[e^{-4iJ_{0j}s_0 t - 4iJ_{1j}s_1 t}\cos^2\frac{\theta_j}{2} + e^{4iJ_{0j}s_0 t + 4iJ_{1j}s_1 t}\sin^2\frac{\theta_j}{2}\right],\end{aligned} \tag{D.2}$$

where $\rho_{0,0}$ and $\rho_{0,1}$ are the initial density matrices of sites 0 and 1, and θ_j is the azimuthal angle on the Bloch sphere for the initial state of site j. We take a further step, and also simplify $\theta_j \equiv \pi/2$, i.e. we choose a particular initial condition at infinite temperature. As a result, we find that $\langle \sigma_0^x(t)\sigma_1^x(t)\rangle$ is an oscillating function, modulated by envelopes of the form

$$A_\pm(t) := \prod_{j\neq 0,1} \left|\cos\left(4J_{0j}t \pm 4J_{1j}t\right)\right|. \tag{D.3}$$

It is clear that, if we want to understand the leading-order behaviour in time, we can reduce to study the simpler function

$$A(t) := \prod_{j\neq 0} \left|\cos\left(J_{0j}t\right)\right| \tag{D.4}$$

where, we recall, J_{0j} are Gaussian variables of zero average and standard deviation $w_j := J_0 e^{-|j|/\kappa}$.

A first consequence of Eq. (D.4) is that $A(\infty) \simeq 2^{-L/2}$ at infinite time, for finite chains. This is related also to the final value of the concurrence, exponentially small in the system size, as discussed in the main text.

Then, one can estimate the *typical* value of $A(t)$ by means of $\mathrm{typ}[A(t)] = \exp\overline{\ln A(t)}$ (one needs to average the *logarithm* of A because, with hindsight, there will be a power-law tail). Since

$$\overline{\ln A(t)} = \sum_j \int dJ_{0j}\, \frac{e^{-J_{0j}^2/2w_j^2}}{\sqrt{2\pi w_j^2}}\, \ln\left|\cos(J_{0j}t)\right|, \tag{D.5}$$

we just need to compute the integral

$$\int dJ_{0j}\, \frac{e^{-J_{0j}^2/2w_j^2}}{\sqrt{2\pi w_j^2}}\, \ln\left|\cos(J_{0j}t)\right| \tag{D.6}$$

$$= \int dJ_{0j}\, \frac{e^{-J_{0j}^2/2w_j^2}}{\sqrt{2\pi w_j^2}}\, \left[\ln\left|1+e^{2iJ_{0j}t}\right| - \ln 2\right] \tag{D.7}$$

$$= \int dJ_{0j}\, \frac{e^{-J_{0j}^2/2w_j^2}}{\sqrt{2\pi w_j^2}} \sum_{n\geq 1} \frac{(-1)^{n+1}}{n} e^{2inJ_{0j}t} - \ln 2 \tag{D.8}$$

$$= \sum_{n\geq 1} \frac{(-1)^{n+1}}{n} e^{-2n^2 w_j^2 t^2} - \ln 2. \tag{D.9}$$

Now, we can proceed by approximating

$$\sum_{n\geq 1} \frac{(-1)^{n+1}}{n} e^{-2n^2 w_j^2 t^2} \approx \begin{cases} 0 & w_j^2 t^2 \gtrsim 1 \\ \ln 2 & w_j^2 t^2 \lesssim 1, \end{cases} \tag{D.10}$$

which implies

$$\sum_j \left\{ \sum_{n\geq 1} \frac{(-1)^{n+1}}{n} e^{-2n^2 w_j^2 t^2} - \ln 2 \right\} \approx -N(t)\ln 2 \tag{D.11}$$

with $N(t)$ given by

$$N(t) = \#\{j \mid w_j^2\, t^2 > 1\} = \begin{cases} 2\kappa \ln\left(J_0 t\right) & t > 1/J_0 \\ 0 & t < 1/J_0. \end{cases} \tag{D.12}$$

Finally, we find

$$\mathrm{typ}[A(t)] = \begin{cases} (J_0 t)^{-\kappa \ln 4} & t > 1/J_0 \\ 1 & t < 1/J_0. \end{cases} \tag{D.13}$$

Substituting this typical value in the definition of τ, Eq. (8.4), we get

$$\mathrm{typ}[\tau] = J_0^{-1} \exp\left(\frac{\int_0^\infty dt\ \mathrm{typ}[A(t)]\ \ln(J_0 t)}{\int_0^\infty dt\ \mathrm{typ}[A(t)]} \right) \tag{D.14}$$

$$= (eJ_0)^{-1} \exp\left\{ \frac{1}{\kappa \ln 4 - 1} \right\}. \tag{D.15}$$

D.3. Finite size and finite disorder effects

In view of the strong finite-size effects (see Fig. 8.1a in the main text), let us first consider the probability distribution function (pdf) of τ_i. In Fig. D.1 we show the distribution of the local relaxation times of the concurrence, computed within the XXZ model. The tail of the distribution is cut away according to the following procedure. We observe that in some instances the nearest-neighbor concurrence $C_{ii+1}(t)$ becomes numerically indistinguishable from 0 at a time t^*, and then stays equal to 0 definitively. We perform an evolution lasting only a finite time t_{fin}, so for the finite size we consider there will be many sites and realizations with $t^* > t_{\mathrm{fin}}$. This is the reason why the full distributions in Figs. D.1 and 8.1a show such a huge peak at large times: it is formed by the contributions of $C_{ii+1}(t)$ which have not yet vanished on the finite-time window t_{fin} of our evolution, for the finite system size we consider. In order to get rid of this peak, we choose a certain truncation time $t_{\mathrm{tr}} \leq t_{\mathrm{fin}}$, and select only the sites and the realizations for which $t^* < t_{\mathrm{tr}}$. As we can see in Fig. D.1 the huge peak disappears and there is a large-time tail which depends on the chosen value of t_{tr}. The small-time structure is, on the opposite, quite independent of the truncation, so we expect that it has a physical meaning. There is a peak around $\log_{10}\tau \simeq -1$, which resembles the one appearing in the l-bit distributions; however, another peak is present around $\log_{10}\tau \simeq 1$. The two-peak structure has no equal in the l-bit model results; we argue that this might be due to the n-body interactions with $n \geq 3$ missing in the l-bit model.

Fig. D.2a shows the pdf's of $\log_{10}(\tau_i)$, obtained within the l-bit model for different values of L, at $\kappa = 1$, $\varepsilon = 0$. We see that, when $L \leq 20$, the probability distribution presents a peak at $\tau_i = O(t_{\mathrm{fin}})$, where t_{fin} is the final time used in the numerical simulations for the time evolution. This is the same effect observed in Fig. 8.1a. In particular, we see that the shape of the pdf's at $L = 10, 15, 20$ strongly resembles the behavior observed in the XXZ model, confirming that those results are strongly affected by finite-size effects. In Fig. D.2b–D.2c we reproduce the pdf's at $L = 16$, $\varepsilon = 0$, and different values of κ an t_{fin}. In the presence of finite-size effects we do not observe the decay of the pdf that is found in larger system sizes. We observe instead a peak in the distribution at $\tau_i = t_{\mathrm{fin}}$.

As anticipated in the main text, the correlation function $G_\tau(r)$ defined in Eq. (8.5) is a self-averaging quantity, as depicted in Fig. D.3. It is indeed only slightly sensitive to finite-size effects (see Fig. D.3a), and to disorder fluctuations (see Fig. D.3b).

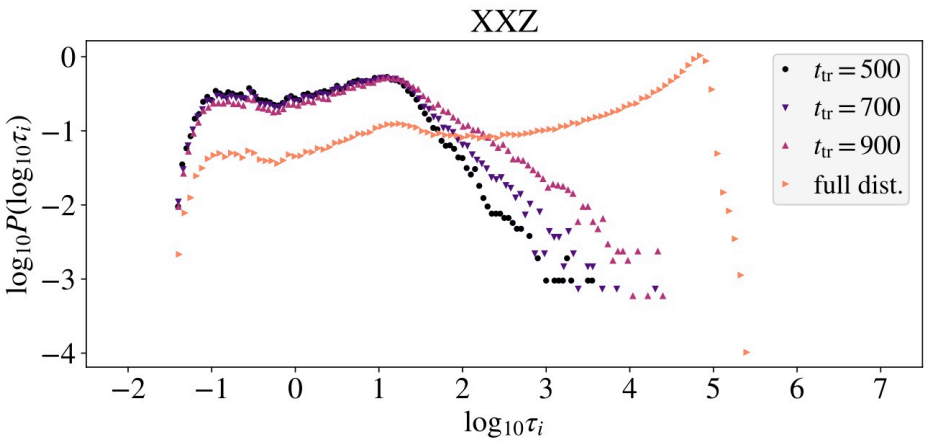

(a)

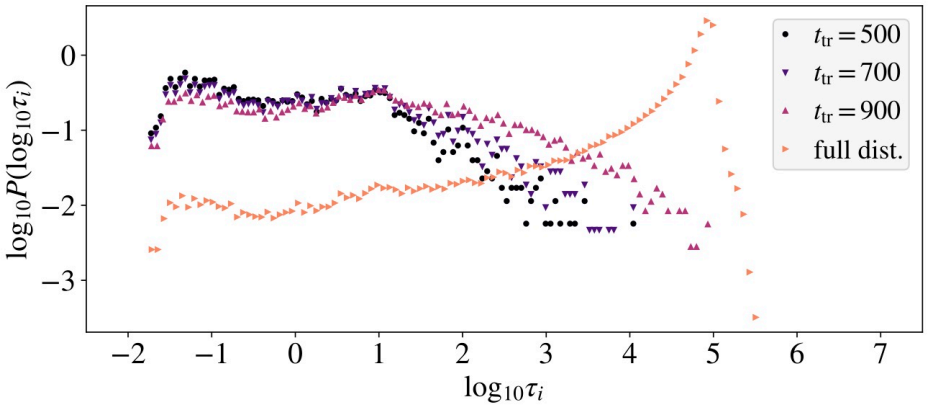

(b)

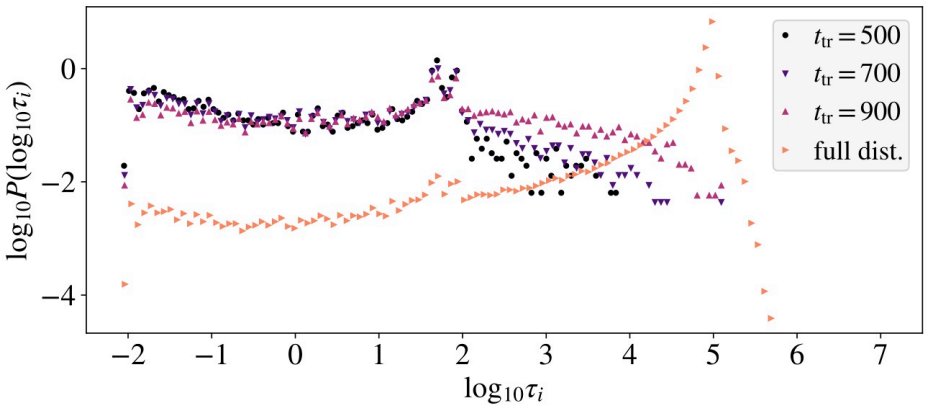

(c)

Figure D.1.: Results for the XXZ model. We show the pdf's of $\log_{10}\tau_i$, truncated as described in the text. The simulations were performed with a chain of length $L = 16$, final time $t_{\rm fin} = 1000$, and disorder strength $W = 9$ (panel (a)), $W = 15$ (panel (b)), $W = 25$ (panel (c)). We compare the truncated distributions with the corresponding full distribution. Data from at least 8000 disorder realizations.

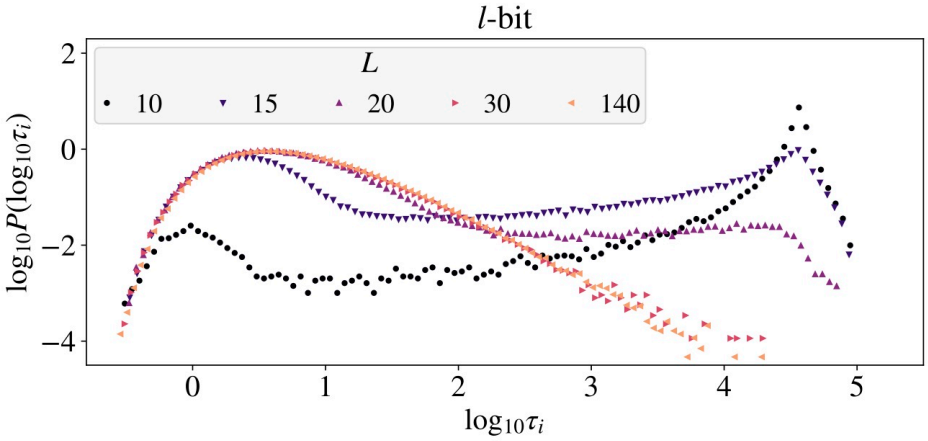

(a)

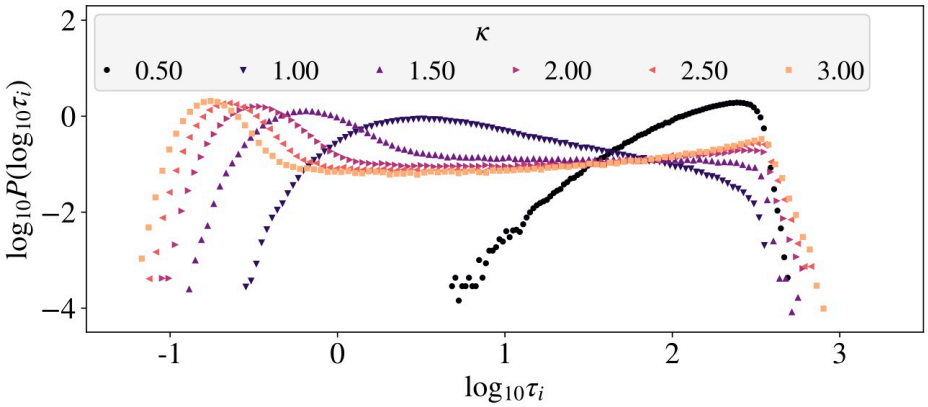

(b)

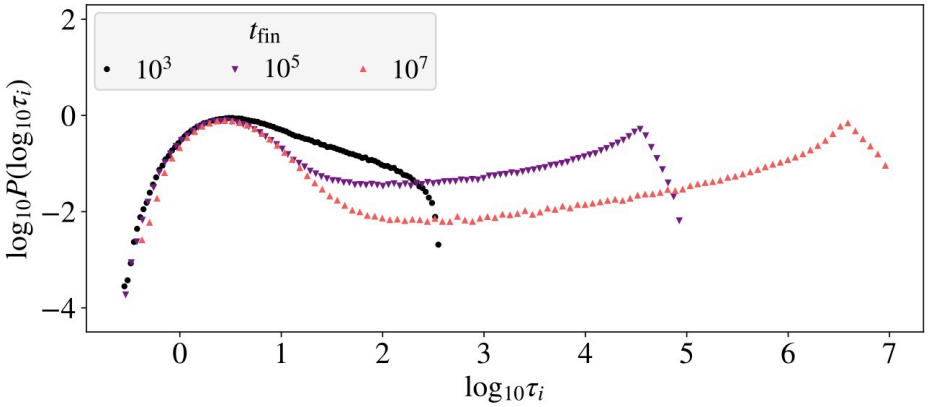

(c)

Figure D.2.: Pdf's of $\log_{10}(\tau_i)$, obtained within the l-bit model. (a) Results for $\kappa = 1$, $\varepsilon = 0$, and different values of L. We see that, when the system size is too small, the pdf's present a spurious peak at large values of τ_i. Indeed, entanglement cannot spread over many sites, and the concurrence of some strongly interacting couples remains finite even at infinite times ($C_i(\infty) = O(2^{-L})$). We collected data from 20 initial states for, at least, 300 disorder realizations. (b) Results for $L = 16$, $\varepsilon = 0$, and different values of κ. Data collected from 21000 disorder realizations. (c) Results for $L = 16$, $\kappa = 1$, $\varepsilon = 0$, and different values of the final time of the time evolution, t_{fin}. Data collected from 21000 disorder realizations.

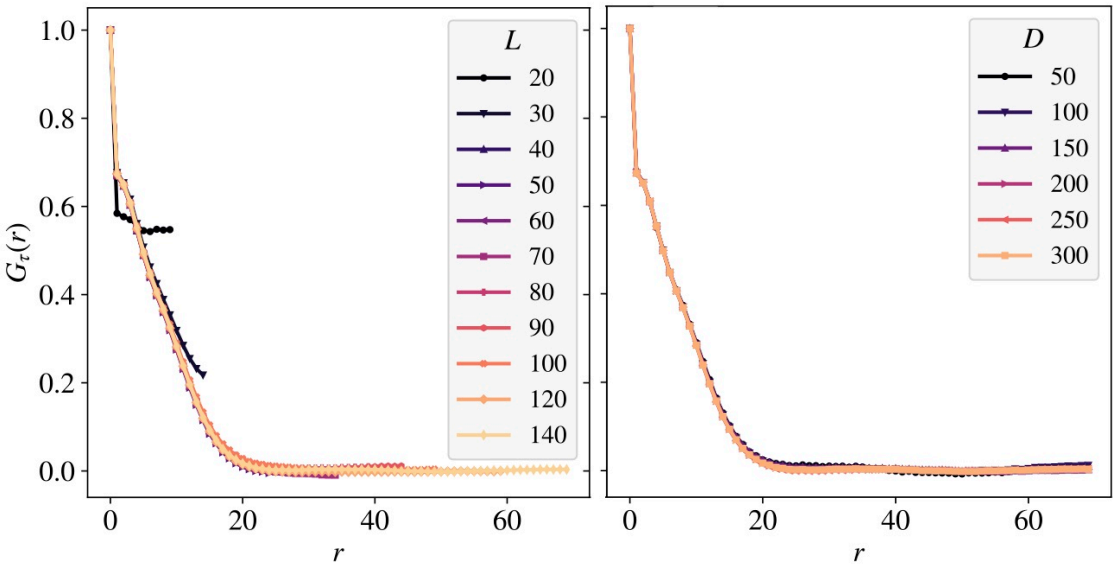

(a) (b)

Figure D.3.: $G_\tau(r)$ defined in the main text, Eq. (8.5). Results for the l-bit model (8.1) for: (a) $\kappa = 1$, $\varepsilon = 0$, and various system sizes L, averaged over $D = 300$ disorder realizations and 20 initial states; (b) $\kappa = 1$, $\varepsilon = 0$, $L = 140$, averaged over a different number of disorder realizations D, and 20 initial states. We see that $G_\tau(r)$ converges quickly to its thermodynamic value (panel (a)), and is almost independent on the number of disorder realizations (panel (b)).

Bibliography

[1] L. Berthier and G. Biroli, "Theoretical perspective on the glass transition and amorphous materials," *Rev. Mod. Phys.*, vol. 83, no. 2, p. 587, 2011. DOI: 10.1103/RevModPhys.83.587.

[2] P. G. Debenedetti and F. H. Stillinger, "Supercooled liquids and the glass transition," *Nature*, vol. 410, no. 6825, p. 259, 2001. DOI: 10.1038/35065704.

[3] F. H. Stillinger, "A topographic view of supercooled liquids and glass formation," *Science*, vol. 267, no. 5206, p. 1935, 1995. DOI: 10.1126/science.267.5206.1935.

[4] I. Gutzow and J. Schmelzer, *The vitreous state: Thermodynamics, Structure, Rheology and Crystallization*. Springer, 1995. DOI: 10.1007/978-3-662-03187-2.

[5] C. A. Angell, "Perspective on the glass transition," *J. Chem. Phys Solids*, vol. 49, no. 8, p. 863, 1988. DOI: 10.1016/0022-3697(88)90002-9.

[6] C. A. Angell, K. L. Ngai, G. B. McKenna, P. F. McMillan, and S. W. Martin, "Relaxation in glassforming liquids and amorphous solids," *J. Appl. Phys.*, vol. 88, no. 6, p. 3113, 2000. DOI: 10.1063/1.1286035.

[7] W. Kob, "Course 5: Supercooled liquids, the glass transition, and computer simulations," in *Slow relaxations and nonequilibrium dynamics in condensed matter*, Springer, 2003, p. 199.

[8] J. C. Dyre, "Colloquium: The glass transition and elastic models of glass-forming liquids," *Rev. Mod. Phys.*, vol. 78, no. 3, p. 953, 2006. DOI: 10.1103/RevModPhys.78.953.

[9] L. Leuzzi and T. M. Nieuwenhuizen, *Thermodynamics of the glassy state*. CRC Press, 2007. DOI: 10.1201/9781420012439.

[10] S. A. Kivelson and G. Tarjus, "In search of a theory of supercooled liquids," *Nature Mater.*, vol. 7, no. 11, p. 831, 2008. DOI: 10.1038/nmat2304.

[11] A. Cavagna, "Supercooled liquids for pedestrians," *Phys. Rep.*, vol. 476, no. 4, p. 51, 2009. DOI: 10.1016/j.physrep.2009.03.003.

[12] K. Binder and W. Kob, *Glassy materials and disordered solids: An introduction to their statistical mechanics*. World Scientific, 2011. DOI: 10.1063/1.2364252.

[13] E. Donth, *The glass transition: relaxation dynamics in liquids and disordered materials*. Springer, 2013, vol. 48. DOI: 10.1063/1.1537917.

[14] G. Biroli and J. P. Garrahan, "Perspective: The glass transition," *J. Chem. Phys.*, vol. 138, no. 12, 12A301, 2013. DOI: 10.1063/1.4795539.

[15] M. Mézard, G. Parisi, and M. A. Virasoro, *Spin glass theory and beyond: An Introduction to the Replica Method and Its Applications*. World Scientific, 1987, vol. 9.

[16] G. Parisi and F. Zamponi, "Mean-field theory of hard sphere glasses and jamming," *Rev. Mod. Phys.*, vol. 82, no. 1, p. 789, 2010. DOI: 10.1103/RevModPhys.82.789.

[17] P. Charbonneau, J. Kurchan, G. Parisi, P. Urbani, and F. Zamponi, "Fractal free energy landscapes in structural glasses," *Nature Commun.*, vol. 5, no. 1, p. 1, 2014. DOI: 10.1038/ncomms4725.

[18] T. E. Angelini, E. Hannezo, X. Trepat, M. Marquez, J. J. Fredberg, and D. A. Weitz, "Glass-like dynamics of collective cell migration," *Proc. Natl. Acad. Sci. U.S.A.*, vol. 108, no. 12, p. 4714, 2011. DOI: 10.1073/pnas.1010059108.

[19] J. P. Garrahan, "Dynamic heterogeneity comes to life," *Proc. Natl. Acad. Sci. U.S.A.*, vol. 108, no. 12, p. 4701, 2011. DOI: 10.1073/pnas.1101436108.

[20] S. C. Glotzer, N. Jan, T. Lookman, A. B. MacIsaac, and P. H. Poole, "Dynamical heterogeneity in the Ising spin glass," *Phys. Rev. E*, vol. 57, no. 6, p. 7350, 1998. DOI: 10.1103/PhysRevE.57.7350.

[21] M. D. Ediger, "Spatially heterogeneous dynamics in supercooled liquids," *Ann. Rev. Phys. Chem.*, vol. 51, no. 1, p. 99, 2000. DOI: 10.1146/annurev.physchem.51.1.99.

[22] S. C. Glotzer, "Spatially heterogeneous dynamics in liquids: Insights from simulation," *J. Non-Cryst. Solids*, vol. 274, no. 1, p. 342, 2000. DOI: 10.1016/S0022-3093(00)00225-8.

[23] L. Berthier, G. Biroli, J.-P. Bouchaud, L. Cipelletti, and W. van Saarloos, *Dynamical heterogeneities in glasses, colloids, and granular media*. Oxford University Press, 2011, vol. 150. DOI: 10.1093/acprof:oso/9780199691470.001.0001.

[24] L. Berthier, "Dynamic heterogeneity in amorphous materials," *Physics*, vol. 4, p. 42, 2011. DOI: 10.1103/Physics.4.42.

[25] D. L. Anderson, "Through the glass lightly," *Science*, vol. 267, no. 5204, p. 1618, 1995. DOI: 10.1126/science.267.5204.1609-a.

[26] G. Adam and J. H. Gibbs, "On the temperature dependence of cooperative relaxation properties in glass-forming liquids," *J Chem. Phys.*, vol. 43, no. 1, p. 139, 1965. DOI: 10.1063/1.1696442.

[27] D. R. Reichman and P. Charbonneau, "Mode-coupling theory," *J. Stat. Mech.*, P05013, 2005. DOI: 10.1088/1742-5468/2005/05/P05013.

[28] G. Tarjus, S. A. Kivelson, Z. Nussinov, and P. Viot, "The frustration-based approach of supercooled liquids and the glass transition: A review and critical assessment," *J. Phys. Condens. Matter*, vol. 17, no. 50, R1143, 2005. DOI: 10.1088/0953-8984/17/50/R01.

[29] D. Chandler and J. P. Garrahan, "Dynamics on the way to forming glass: Bubbles in space-time," *Annu. Rev. Phys. Chem.*, vol. 61, p. 191, 2010. DOI: 10.1146/annurev.physchem.040808.090405.

[30] G. Biroli and J.-P. Bouchaud, "The random first-order transition theory of glasses: A critical assessment," *Structural Glasses and Supercooled Liquids: Theory, Experiment, and Applications*, p. 31, 2012.

[31] R. Zeller and R. Pohl, "Thermal conductivity and specific heat of noncrystalline solids," *Phys. Rev. B*, vol. 4, no. 6, p. 2029, 1971. DOI: 10.1103/PhysRevB.4.2029.

[32] T. S. Grigera, V. Martín-Mayor, G. Parisi, and P. Verrocchio, "Phonon interpretation of the 'boson peak'in supercooled liquids," *Nature*, vol. 422, no. 6929, p. 289, 2003. DOI: 10.1038/nature01475.

[33] W. A. Phillips, "Two-level states in glasses," *Rep. Progr. Phys.*, vol. 50, no. 12, p. 1657, 1987. DOI: 10.1088/0034-4885/50/12/003.

[34] P. W. Anderson, B. Halperin, and C. M. Varma, "Anomalous low-temperature thermal properties of glasses and spin glasses," *Philos. Mag.*, vol. 25, no. 1, p. 1, 1972. DOI: 10.1080/14786437208229210.

[35] W. Phillips, "Tunneling states in amorphous solids," *J. Low Temp. Phys.*, vol. 7, no. 3, p. 351, 1972. DOI: 10.1007/BF00660072.

[36] V. Lubchenko, "Low-temperature anomalies in disordered solids: A cold case of contested relics?" *Adv. Phys. X*, vol. 3, no. 1, p. 1 510 296, 2018. DOI: 10.1080/23746149.2018.1510296.

[37] J. Lisenfeld, G. J. Grabovskij, C. Müller, J. H. Cole, G. Weiss, and A. V. Ustinov, "Observation of directly interacting coherent two-level systems in an amorphous material," *Nature Comm.*, vol. 6, no. 1, p. 6182, 2015. DOI: 10.1038/ncomms7182.

[38] D. Khomenko, C. Scalliet, L. Berthier, D. R. Reichman, and F. Zamponi, "Depletion of two-level systems in ultrastable computer-generated glasses," *Phys. Rev. Lett.*, vol. 124, no. 22, p. 225 901, 2020. DOI: 10.1103/PhysRevLett.124.225901.

[39] D. Khomenko, D. R. Reichman, and F. Zamponi, "Relationship between two-level systems and quasilocalized normal modes in glasses," *Phys. Rev. Mater.*, vol. 5, no. 5, p. 055 602, 2021. DOI: 10.1103/PhysRevMaterials.5.055602.

[40] L. Faoro and L. B. Ioffe, "Interacting tunneling model for two-level systems in amorphous materials and its predictions for their dephasing and noise in superconducting microresonators," *Phys. Rev. B*, vol. 91, no. 1, p. 014 201, 2015. DOI: 10.1103/PhysRevB.91.014201.

[41] H. M. Carruzzo and C. C. Yu, "Why phonon scattering in glasses is universally small at low temperatures," *Phys. Rev. Lett.*, vol. 124, no. 7, p. 075 902, 2020. DOI: 10.1103/PhysRevLett.124.075902.

[42] J. Jäckle, "On the ultrasonic attenuation in glasses at low temperatures," *Z. Phys.*, vol. 257, no. 3, p. 212, 1972. DOI: 10.1007/BF01401204.

[43] R. B. Stephens, "Low-temperature specific heat and thermal conductivity of noncrystalline dielectric solids," *Phys. Rev. B*, vol. 8, no. 6, p. 2896, 1973. DOI: 10.1103/PhysRevB.8.2896.

[44] U. Buchenau, M. Prager, N. Nücker, A. Dianoux, N. Ahmad, and W. Phillips, "Low-frequency modes in vitreous silica," *Phys. Rev. B*, vol. 34, no. 8, p. 5665, 1986. DOI: 10.1103/PhysRevB.34.5665.

[45] V. Malinovsky, V. Novikov, P. Parshin, A. Sokolov, and M. Zemlyanov, "Universal form of the low-energy (2 to 10 mev) vibrational spectrum of glasses," *Europhys. Lett.*, vol. 11, no. 1, p. 43, 1990. DOI: 10.1209/0295-5075/11/1/008/.

[46] A. Fefferman, R. Pohl, A. Zehnder, and J. Parpia, "Acoustic properties of amorphous silica between 1 and 500 mk," *Phys. Rev. Lett.*, vol. 100, no. 19, p. 195 501, 2008. DOI: 10.1103/PhysRevLett.100.195501.

[47] A. C. Anderson, B. Golding, J. Graebner, S. Hunklinger, J. Jäckle, W. Phillips, R. Pohl, M. Schickfus, and D. Weaire, *Amorphous solids: low-temperature properties*. Springer, 2012, vol. 24. DOI: 10.1007/978-3-642-81534-8.

[48] P. Esquinazi, *Tunneling systems in amorphous and crystalline solids*. Springer, 2013. DOI: 10.1007/978-3-662-03695-2.

[49] C. Enss, "Beyond the tunneling model: Quantum phenomena in ultracold glasses," *Physica (Amsterdam)*, vol. 316B, 2002. DOI: 10.1016/S0921-4526(02)00419-2.

[50] V. Karpov, I. Klinger, and F. Ignat'Ev, "Theory of the low-temperature anomalies in the thermal properties of amorphous structures," *Zh. Eksp. Teor. Fiz*, vol. 84, p. 760, 1983.

[51] U. Buchenau, Y. M. Galperin, V. Gurevich, D. Parshin, M. Ramos, and H. Schober, "Interaction of soft modes and sound waves in glasses," *Phys. Rev. B*, vol. 46, no. 5, p. 2798, 1992. DOI: 10.1103/PhysRevB.46.2798.

[52] D. Parshin, "Soft potential model and universal properties of glasses," *Physica Scripta*, vol. 1993, no. T49A, p. 180, 1993. DOI: 10.1088/0031-8949/1993/T49A/030.

[53] A. J. Leggett and C. C. Yu, "Low temperature properties of amorphous materials: Through a glass darkly," *Comments Condens. Matter Phys.*, vol. 14, p. 231, 1988.

[54] A. J. Leggett, "Amorphous materials at low temperatures: Why are they so similar?" *Physica B*, vol. 169, no. 1, p. 322, 1991. DOI: 10.1016/0921-4526(91)90246-B.

[55] A. J. Leggett and D. C. Vural, ""Tunneling two-level systems" model of the low-temperature properties of glasses: Are "smoking-gun" tests possible?" *J. Phys. Chem. B*, vol. 117, no. 42, p. 12 966, 2013. DOI: 10.1021/jp402222g.

[56] A.-M. Boiron, P. Tamarat, B. Lounis, R. Brown, and M. Orrit, "Are the spectral trails of single molecules consistent with the standard two-level system model of glasses at low temperatures?" *Chem. Phys.*, vol. 247, no. 1, p. 119, 1999. DOI: 10.1016/S0301-0104(99)00140-8.

[57] I. Y. Eremchev, Y. G. Vainer, A. V. Naumov, and L. Kador, "Low-temperature dynamics in amorphous polymers and low-molecular-weight glasses–what is the difference?" *Phys. Chem. Chem. Phys.*, vol. 13, no. 5, p. 1843, 2011. DOI: 10.1039/C0CP01690J.

[58] G. J. Grabovskij, T. Peichl, J. Lisenfeld, G. Weiss, and A. V. Ustinov, "Strain tuning of individual atomic tunneling systems detected by a superconducting qubit," *Science*, vol. 338, no. 6104, p. 232, 2012. DOI: 10.1126/science.1226487.

[59] J. Lasjaunias, A. Ravex, M. Vandorpe, and S. Hunklinger, "The density of low energy states in vitreous silica: Specific heat and thermal conductivity down to 25 mk," *Solid State Commun.*, vol. 17, no. 9, p. 1045, 1975. DOI: 10.1016/0038-1098(75)90251-3.

[60] M. A. Ramos, "Are universal "anomalous" properties of glasses at low temperatures truly universal?" *Low Temp. Phys.*, vol. 46, no. 2, p. 104, 2020. DOI: 10.1063/10.0000527.

[61] S. Ludwig, C. Enss, P. Strehlow, and S. Hunklinger, "Direct coupling of magnetic fields to tunneling systems in glasses," *Phys. Rev. Lett.*, vol. 88, no. 7, p. 075 501, 2002. DOI: 10.1103/PhysRevLett.88.075501.

[62] P. Nagel, A. Fleischmann, S. Hunklinger, and C. Enss, "Novel isotope effects observed in polarization echo experiments in glasses," *Phys. Rev. Lett.*, vol. 92, no. 24, p. 245 511, 2004. DOI: 10.1103/PhysRevLett.92.245511.

[63] G. Jug, "Theory of the thermal magnetocapacitance of multicomponent silicate glasses at low temperature," *Philos. Mag.*, vol. 84, no. 33, p. 3599, 2004. DOI: 10.1080/14786430417331284027.

[64] G. Jug, S. Bonfanti, and W. Kob, "Realistic tunnelling states for the magnetic effects in non-metallic real glasses," *Philos. Mag.*, vol. 96, no. 7, p. 648, 2016. DOI: 10.1080/14786435.2015.1109717.

[65] R. O. Pohl, X. Liu, and E. Thompson, "Low-temperature thermal conductivity and acoustic attenuation in amorphous solids," *Rev. Mod. Phys.*, vol. 74, no. 4, p. 991, 2002. DOI: 10.1103/RevModPhys.74.991.

[66] M. Schechter, P. Nalbach, and A. L. Burin, "Nonuniversality and strongly interacting two-level systems in glasses at low temperatures," *New J. Phys.*, vol. 20, no. 6, p. 063 048, 2018. DOI: 10.1088/1367-2630/aac930.

[67] W. Arnold and S. Hunklinger, "Experimental evidence for the direct interaction between two-level systems in glasses at very low temperatures," *Solid State Comm.*, vol. 17, no. 7, p. 883, 1975. DOI: 10.1016/0038-1098(75)90743-7.

[68] J. L. Black and B. I. Halperin, "Spectral diffusion, phonon echoes, and saturation recovery in glasses at low temperatures," *Phys. Rev. B*, vol. 16, no. 6, p. 2879, 1977. DOI: 10.1103/PhysRevB.16.2879.

[69] P. Strehlow, C. Enss, and S. Hunklinger, "Evidence for a phase transition in glasses at very low temperature: A macroscopic quantum state of tunneling systems?" *Phys. Rev. Lett.*, vol. 80, no. 24, p. 5361, 1998. DOI: 10.1103/PhysRevLett.80.5361.

[70] A. L. Burin, D. Natelson, D. D. Osheroff, and Y. Kagan, "Interactions between tunneling defects in amorphous solids," *Tunneling systems in amorphous and crystalline solids*, p. 223, 1998.

[71] J. Classen, T. Burkert, C. Enss, and S. Hunklinger, "Anomalous frequency dependence of the internal friction of vitreous silica," *Phys. Rev. Lett.*, vol. 84, no. 10, p. 2176, 2000. DOI: 10.1103/PhysRevLett.84.2176.

[72] C. Enss and S. Hunklinger, "Incoherent tunneling in glasses at very low temperatures," *Phys. Rev. Lett.*, vol. 79, no. 15, p. 2831, 1997. DOI: 10.1103/PhysRevLett.79.2831.

[73] J. Joffrin and A. Levelut, "Virtual phonon exchange in glasses," *J. Phys.*, vol. 36, no. 9, p. 811, 1975. DOI: 10.1051/jphys:01975003609081100.

[74] K. Kassner and R. Silbey, "Interactions of two-level systems in glasses," *J. Phys. Condens. Matter*, vol. 1, no. 28, p. 4599, 1989. DOI: 10.1088/0953-8984/1/28/009.

[75] A. L. Burin, L. A. Maksimov, and I. Y. Polishchuk, "The dephasing rate in glasses at ultra low temperatures," *Czech. J. Phys.*, vol. 46, no. 4, p. 2271, 1996. DOI: 10.1007/BF02571127.

[76] O. Asban, A. Amir, Y. Imry, and M. Schechter, "Effect of interactions and disorder on the relaxation of two-level systems in amorphous solids," *Phys. Rev. B*, vol. 95, no. 14, p. 144 207, 2017. DOI: 10.1103/PhysRevB.95.144207.

[77] S. F. Swallen, K. L. Kearns, M. K. Mapes, Y. S. Kim, R. J. McMahon, M. D. Ediger, T. Wu, L. Yu, and S. Satija, "Organic glasses with exceptional thermodynamic and kinetic stability," *Science*, vol. 315, no. 5810, p. 353, 2007. DOI: 10.1126/science.1135795.

[78] D. Queen, X. Liu, J. Karel, T. Metcalf, and F. Hellman, "Excess specific heat in evaporated amorphous silicon," *Phys. Rev. Lett.*, vol. 110, no. 13, p. 135 901, 2013. DOI: 10.1103/PhysRevLett.110.135901.

[79] X. Liu, D. R. Queen, T. H. Metcalf, J. E. Karel, and F. Hellman, "Hydrogen-free amorphous silicon with no tunneling states," *Phys. Rev Lett.*, vol. 113, no. 2, p. 025 503, 2014. DOI: 10.1103/PhysRevLett.113.025503.

[80] T. Pérez-Castañeda, C. Rodríguez-Tinoco, J. Rodríguez-Viejo, and M. A. Ramos, "Suppression of tunneling two-level systems in ultrastable glasses of indomethacin," *Proc. Natl. Acad. Sci. U.S.A*, vol. 111, no. 31, p. 11 275, 2014. DOI: 10.1073/pnas.1405545111.

[81] M. D. Ediger, "Perspective: Highly stable vapor-deposited glasses," *J. Chem. Phys.*, vol. 147, no. 21, p. 210 901, 2017. DOI: 10.1063/1.5006265.

[82] B. Seoane, D. R. Reid, J. J. de Pablo, and F. Zamponi, "Low-temperature anomalies of a vapor deposited glass," *Phys. Rev. Mater.*, vol. 2, no. 1, p. 015 602, 2018. DOI: 10.1103/PhysRevMaterials.2.015602.

[83] T. Pérez-Castañeda, R. J. J. Riobóo, and M. A. Ramos, "Low-temperature thermal properties of a hyperaged geological glass," *J. Phys. Condens. Matter*, vol. 25, no. 29, p. 295 402, 2013. DOI: 10.1088/0953-8984/25/29/295402.

[84] T. Pérez-Castañeda, R. J. Jiménez-Riobóo, and M. A. Ramos, "Two-level systems and boson peak remain stable in 110-million-year-old amber glass," *Phys. Rev. Lett.*, vol. 112, no. 16, p. 165 901, 2014. DOI: 10.1103/PhysRevLett.112.165901.

[85] J. De Yoreo, W. Knaak, M. Meissner, and R. Pohl, "Low-temperature properties of crystalline $(KBr)_{1-x}(KCN)_x$: A model glass," *Phys. Rev. B*, vol. 34, no. 12, p. 8828, 1986. DOI: 10.1103/PhysRevB.34.8828.

[86] C. C. Yu and H. M. Carruzzo, "Two-level systems and the tunneling model: A critical view," *arXiv:2101.02787*, 2021.

[87] A. J. Liu and S. R. Nagel, "Nonlinear dynamics: Jamming is not just cool any more," *Nature*, vol. 396, no. 6706, p. 21, 1998. DOI: 10.1038/23819.

[88] V. Trappe, V. Prasad, L. Cipelletti, P. Segre, and D. A. Weitz, "Jamming phase diagram for attractive particles," *Nature*, vol. 411, no. 6839, p. 772, 2001. DOI: 10.1038/35081021.

[89] C. Scalliet, L. Berthier, and F. Zamponi, "Absence of marginal stability in a structural glass," *Phys. Rev. Lett.*, vol. 119, no. 20, p. 205 501, 2017. DOI: 10.1103/PhysRevLett.119.205501.

[90] ——, "Marginally stable phases in mean-field structural glasses," *Phys. Rev. E*, vol. 99, no. 1, p. 012 107, 2019. DOI: 10.1103/PhysRevE.99.012107.

[91] ——, "Nature of excitations and defects in structural glasses," *Nature Commun.*, vol. 10, no. 1, p. 1, 2019. DOI: 10.1038/s41467-019-13010-x.

[92] L. Berthier, G. Biroli, P. Charbonneau, E. I. Corwin, S. Franz, and F. Zamponi, "Gardner physics in amorphous solids and beyond," *J. Chem. Phys.*, vol. 151, no. 1, p. 010 901, 2019. DOI: 10.1063/1.5097175.

[93] J. Kurchan, G. Parisi, P. Urbani, and F. Zamponi, "Exact theory of dense amorphous hard spheres in high dimension. II. The high density regime and the gardner transition," *J. Phys. Chem. B*, vol. 117, no. 42, p. 12 979, 2013. DOI: 10.1021/jp402235d.

[94] P. Charbonneau, J. Kurchan, G. Parisi, P. Urbani, and F. Zamponi, "Exact theory of dense amorphous hard spheres in high dimension. III. The full replica symmetry breaking solution," *J. Stat. Mech.*, vol. 2014, no. 10, p. 10 009, 2014. DOI: 10.1088/1742-5468/2014/10/P10009.

[95] ——, "Glass and jamming transitions: From exact results to finite-dimensional descriptions," *Annu. Rev. Condens. Matter Phys.*, vol. 8, p. 265, 2017. DOI: 10.1146/annurev-conmatphys-031016-025334.

[96] G. Biroli and P. Urbani, "Liu-Nagel phase diagrams in infinite dimension," *SciPost Phys.*, vol. 4, no. 4, p. 20, 2018. DOI: 10.21468/SciPostPhys.4.4.020.

[97] L. Berthier, P. Charbonneau, Y. Jin, G. Parisi, B. Seoane, and F. Zamponi, "Growing timescales and lengthscales characterizing vibrations of amorphous solids," *Proc. Natl. Acad. Sci. U.S.A*, vol. 113, no. 30, p. 8397, 2016. DOI: 10.1073/pnas.1607730113.

[98] B. Seoane and F. Zamponi, "Spin-glass-like aging in colloidal and granular glasses," *Soft Matter*, vol. 14, no. 25, p. 5222, 2018. DOI: 10.1039/C8SM00859K.

[99] Q. Liao and L. Berthier, "Hierarchical landscape of hard disk glasses," *Phys. Rev. X*, vol. 9, no. 1, p. 011 049, 2019. DOI: 10.1103/PhysRevX.9.011049.

[100] M. A. Moore and A. J. Bray, "Disappearance of the de Almeida-Thouless line in six dimensions," *Phys. Rev. B*, vol. 83, no. 22, p. 224 408, 2011. DOI: 10.1103/PhysRevB.83.224408.

[101] P. Urbani and G. Biroli, "Gardner transition in finite dimensions," *Phys. Rev. B*, vol. 91, no. 10, p. 100 202, 2015. DOI: 10.1103/PhysRevB.91.100202.

[102] P. Charbonneau and S. Yaida, "Nontrivial critical fixed point for replica-symmetry-breaking transitions," *Phys. Rev. Lett.*, vol. 118, no. 21, p. 215 701, 2017. DOI: 10.1103/PhysRevLett.118.215701.

[103] D. H. Rojas *et al.*, "Numerical study of the microscopic structure of jammed systems: From inferring their dynamics to finite size scaling," *arXiv:2107.03939*, 2021.

[104] S. Franz and G. Parisi, "Recipes for metastable states in spin glasses," *J. Phys. I*, vol. 5, no. 11, p. 1401, 1995. DOI: 10.1051/jp1:1995201.

[105] G. Biroli and P. Urbani, "Breakdown of elasticity in amorphous solids," *Nat. Phys.*, vol. 12, no. 12, p. 1130, 2016. DOI: 10.1038/nphys3845.

[106] H. Yoshino and F. Zamponi, "Shear modulus of glasses: Results from the full replica-symmetry-breaking solution," *Phys. Rev. E*, vol. 90, no. 2, p. 022 302, 2014. DOI: 10.1103/PhysRevE.90.022302.

[107] F. H. Stillinger, "Exponential multiplicity of inherent structures," *Phys. Rev. E*, vol. 59, no. 1, p. 48, 1999. DOI: 10.1103/PhysRevE.59.48.

[108] C. S. O'Hern, L. E. Silbert, A. J. Liu, and S. R. Nagel, "Jamming at zero temperature and zero applied stress: The epitome of disorder," *Phys. Rev. E*, vol. 68, no. 1, p. 011 306, 2003. DOI: 10.1103/PhysRevE.68.011306.

[109] P. Charbonneau, E. I. Corwin, G. Parisi, and F. Zamponi, "Jamming criticality revealed by removing localized buckling excitations," *Phys. Rev. Lett.*, vol. 114, no. 12, p. 125 504, 2015. DOI: 10.1103/PhysRevLett.114.125504.

[110] S. Franz and G. Parisi, "The simplest model of jamming," *J. Phys. A*, vol. 49, no. 14, p. 145 001, 2016.

[111] F. Rosenblatt, "The perceptron: A probabilistic model for information storage and organization in the brain.," *Psychol. Rev.*, vol. 65, no. 6, p. 386, 1958. DOI: 10.1037/h0042519.

[112] S. Franz, A. Sclocchi, and P. Urbani, "Critical jammed phase of the linear perceptron," *Phys. Rev. Lett.*, vol. 123, no. 11, p. 115 702, 2019. DOI: 10.1103/PhysRevLett.123.115702.

[113] S. Franz, T. Maimbourg, G. Parisi, and A. Scardicchio, "Impact of jamming criticality on low-temperature anomalies in structural glasses," *Proc. Natl. Acad. Sci. U.S.A*, vol. 116, no. 28, p. 13 768, 2019. DOI: 10.1073/pnas.1820360116.

[114] C. Artiaco, P. Baldan, and G. Parisi, "Exploratory study of the glassy landscape near jamming," *Phys. Rev. E*, vol. 101, no. 5, p. 052 605, 2020. DOI: 10.1103/PhysRevE.101.052605.

[115] C. Artiaco, R. Díaz Hernández Rojas, G. Parisi, and F. Ricci-Tersenghi, "An iterative linear programming algorithm for jamming hard spheres," *In preparation*, 2021.

[116] G. B. Dantzig and M. N. Thapa, *Linear programming 1: introduction*. Springer, 2006.

[117] ——, *Linear programming 2: theory and extensions*. Springer, 2006.

[118] A. Donev, S. Torquato, F. H. Stillinger, and R. Connelly, "A linear programming algorithm to test for jamming in hard-sphere packings," *J. Comput. Phys.*, vol. 197, no. 1, p. 139, 2004. DOI: 10.1016/j.jcp.2003.11.022.

[119] S. Torquato and Y. Jiao, "Robust algorithm to generate a diverse class of dense disordered and ordered sphere packings via linear programming," *Phys. Rev. E*, vol. 82, no. 6, p. 061 302, 2010. DOI: 10.1103/PhysRevE.82.061302.

[120] E. Bitzek, P. Koskinen, F. Gähler, M. Moseler, and P. Gumbsch, "Structural relaxation made simple," *Phys. Rev. Lett.*, vol. 97, no. 17, p. 170 201, 2006. DOI: 10.1103/PhysRevLett.97.170201.

[121] P. Charbonneau, E. I. Corwin, R. C. Dennis, R. D. H. Rojas, H. Ikeda, G. Parisi, and F. Ricci-Tersenghi, "Finite-size effects in the microscopic critical properties of jammed configurations: A comprehensive study of the effects of different types of disorder," *Phys. Rev. E*, vol. 104, no. 1, p. 014 102, 2021. DOI: 10.1103/PhysRevE.104.014102.

[122] R. D. H. Rojas, G. Parisi, and F. Ricci-Tersenghi, "Inferring the particle-wise dynamics of amorphous solids from the local structure at the jamming point," *Soft Matter*, vol. 17, no. 4, p. 1056, 2021. DOI: 10.1039/C9SM02283J.

[123] A. Ninarello, L. Berthier, and D. Coslovich, "Models and algorithms for the next generation of glass transition studies," *Phys. Rev. X*, vol. 7, p. 021 039, 2017. DOI: 10.1103/PhysRevX.7.021039.

[124] T. S. Grigera and G. Parisi, "Fast monte carlo algorithm for supercooled soft spheres," *Phys. Rev. E*, vol. 63, no. 4, p. 045 102, 2001. DOI: 10.1103/PhysRevE.63.045102.

[125] J. P. Hansen and I. R. McDonald, *Theory of simple liquids*. Elsevier, 1990.

[126] M. Wyart, "Marginal stability constrains force and pair distributions at random close packing," *Phys. Rev. Lett.*, vol. 109, no. 12, p. 125 502, 2012. DOI: 10.1103/PhysRevLett.109.125502.

[127] C. P. Goodrich, A. J. Liu, and S. R. Nagel, "Finite-size scaling at the jamming transition," *Phys. Rev. Lett.*, vol. 109, no. 9, p. 095 704, 2012. DOI: 10.1103/PhysRevLett.109.095704.

[128] E. Lerner, G. Düring, and M. Wyart, "Low-energy non-linear excitations in sphere packings," *Soft Matter*, vol. 9, p. 8252, 2013. DOI: 10.1039/C3SM50515D.

[129] A. B. Hopkins, F. H. Stillinger, and S. Torquato, "Disordered strictly jammed binary sphere packings attain an anomalously large range of densities," *Phys. Rev. E*, vol. 88, no. 2, p. 022 205, 2013. DOI: 10.1103/PhysRevE.88.022205.

[130] V. Oganesyan and D. A. Huse, "Localization of interacting fermions at high temperature," *Phys. Rev. B*, vol. 75, no. 15, p. 155 111, 2007. DOI: 10.1103/PhysRevB.75.155111.

[131] R Development Core Team, *R: A language and environment for statistical computing*, R Foundation for Statistical Computing, 2008.

[132] G. Parisi, "On the statistical properties of the large time zero temperature dynamics of the SK model," *Fractals*, vol. 11, p. 161, 2003. DOI: 10.1142/9789812778109_0017.

[133] P. Charbonneau, Y. Jin, G. Parisi, C. Rainone, B. Seoane, and F. Zamponi, "Numerical detection of the gardner transition in a mean-field glass former," *Phys. Rev. E*, vol. 92, no. 1, p. 012 316, 2015. DOI: 10.1103/PhysRevE.92.012316.

[134] C. Artiaco, F. Balducci, G. Parisi, and A. Scardicchio, "Quantum jamming: Critical properties of a quantum mechanical perceptron," *Phys. Rev. A*, vol. 103, no. 4, p. L040203, 2021. DOI: 10.1103/PhysRevA.103.L040203.

[135] F. Rosenblatt, "Principles of neurodynamics. perceptrons and the theory of brain mechanisms," Cornell Aeronautical Lab Inc Buffalo NY, Tech. Rep., 1961.

[136] M. Minsky and S. A. Papert, *Perceptrons: An introduction to computational geometry*. MIT press, 1969.

[137] E. Gardner and B. Derrida, "Optimal storage properties of neural network models," *J. Phys. A*, vol. 21, no. 1, p. 271, 1988. DOI: 10.1088/0305-4470/21/1/031.

[138] E. Gardner, "The space of interactions in neural network models," *J. Phys. A*, vol. 21, no. 1, p. 257, 1988. DOI: 10.1088/0305-4470/21/1/030.

[139] M. A. Nielsen, *Neural networks and deep learning*. Determination press, 2015, vol. 25.

[140] M. Mezard and A. Montanari, *Information, physics, and computation*. Oxford University Press, 2009.

[141] S. Kirkpatrick and B. Selman, "Critical behavior in the satisfiability of random boolean expressions," *Science*, vol. 264, no. 5163, p. 1297, 1994. DOI: 10.1126/science.264.5163.1297.

[142] R. Monasson, R. Zecchina, S. Kirkpatrick, B. Selman, and L. Troyansky, "Determining computational complexity from characteristic 'phase transitions'," *Nature*, vol. 400, no. 6740, p. 133, 1999. DOI: 10.1038/22055.

[143] M. Mézard and G. Parisi, "The Bethe lattice spin glass revisited," *Eur. Physi. J. B*, vol. 20, no. 2, p. 217, 2001. DOI: 10.1007/PL00011099.

[144] A. K. Hartmann and M. Weigt, *Phase transitions in combinatorial optimization problems: Basics, algorithms and statistical mechanics*. John Wiley & Sons, 2006.

[145] F. Krzakała, A. Montanari, F. Ricci-Tersenghi, G. Semerjian, and L. Zdeborová, "Gibbs states and the set of solutions of random constraint satisfaction problems," *Proc. Natl. Acad. Sci. U.S.A*, vol. 104, no. 25, p. 10 318, 2007. DOI: 10.1073/pnas.0703685104.

[146] M. Mézard, G. Parisi, and R. Zecchina, "Analytic and algorithmic solution of random satisfiability problems," *Science*, vol. 297, no. 5582, pp. 812–815, 2002.

[147] S. Franz, G. Parisi, M. Sevelev, P. Urbani, and F. Zamponi, "Universality of the SAT-UNSAT (jamming) threshold in non-convex continuous constraint satisfaction problems," *SciPost Phys.*, vol. 2, no. 3, p. 19, 2017. DOI: 10.21468/SciPost.Report.121.

[148] S. Torquato, T. M. Truskett, and P. G. Debenedetti, "Is random close packing of spheres well defined?" *Phys. Rev. Lett.*, vol. 84, no. 10, p. 2064, 2000. DOI: 10.1103/PhysRevLett.84.2064.

[149] P. Charbonneau, E. I. Corwin, G. Parisi, and F. Zamponi, "Universal microstructure and mechanical stability of jammed packings," *Phys. Rev. Lett.*, vol. 109, no. 20, p. 205 501, 2012. DOI: 10.1103/PhysRevLett.109.205501.

[150] S. Franz, G. Parisi, P. Urbani, and F. Zamponi, "Universal spectrum of normal modes in low-temperature glasses," *Proc. Natl. Acad. Sci. U.S.A*, vol. 112, no. 47, p. 14 539, 2015. DOI: 10.1073/pnas.1511134112.

[151] A. Altieri, S. Franz, and G. Parisi, "The jamming transition in high dimension: An analytical study of the TAP equations and the effective thermodynamic potential," *J. Stat. Mech.*, p. 093 301, 2016. DOI: 10.1088/1742-5468/2016/09/093301.

[152] M. Nielsen and I. Chuang, *Quantum Computation and Quantum Information*. Cambridge University Press, Cambridge, 2000.

[153] A. Bray and M. Moore, "Replica theory of quantum spin glasses," *J. Phys. C*, vol. 13, no. 24, p. L655, 1980. DOI: 10.1088/0022-3719/13/24/005.

[154] J. Miller and D. A. Huse, "Zero-temperature critical behavior of the infinite-range quantum ising spin glass," *Phys. Rev. Lett.*, vol. 70, no. 20, p. 3147, 1993. DOI: 10.1103/PhysRevLett.70.3147.

[155] M. Guo, R. N. Bhatt, and D. A. Huse, "Quantum critical behavior of a three-dimensional ising spin glass in a transverse magnetic field," *Phys. Rev. Lett.*, vol. 72, no. 26, p. 4137, 1994. DOI: 10.1103/PhysRevLett.72.4137.

[156] H. Rieger and A. P. Young, "Zero-temperature quantum phase transition of a two-dimensional ising spin glass," *Phys. Rev. Lett.*, vol. 72, no. 26, p. 4141, 1994. DOI: 10.1103/PhysRevLett.72.4141.

[157] N. Read, S. Sachdev, and J. Ye, "Landau theory of quantum spin glasses of rotors and Ising spins," *Phys. Rev. B*, vol. 52, no. 1, p. 384, 1995. DOI: 10.1103/PhysRevB.52.384.

[158] C. Laumann, A. Scardicchio, and S. L. Sondhi, "Cavity method for quantum spin glasses on the Bethe lattice," *Phys. Rev. B*, vol. 78, no. 13, p. 134 424, 2008. DOI: 10.1103/PhysRevB.78.134424.

[159] B. Altshuler, H. Krovi, and J. Roland, "Anderson localization makes adiabatic quantum optimization fail," *Proc. Natl. Acad. Sci. U.S.A*, vol. 107, no. 28, p. 12 446, 2010. DOI: 10.1073/pnas.1002116107.

[160] C. R. Laumann, A. Pal, and A. Scardicchio, "Many-body mobility edge in a mean-field quantum spin glass," *Phys. Rev. Lett.*, vol. 113, no. 20, p. 200 405, 2014. DOI: 10.1103/PhysRevLett.113.200405.

[161] C. R. Laumann, R. Moessner, A. Scardicchio, and S. L. Sondhi, "Quantum annealing: The fastest route to quantum computation?" *Eur. Phys. J. Spec. Top.*, vol. 224, no. 1, p. 75, 2015. DOI: 10.1140/epjst/e2015-02344-2.

[162] R. Nandkishore and D. A. Huse, "Many-body localization and thermalization in quantum statistical mechanics," *Annu. Rev. Condens. Matter Phys.*, vol. 6, no. 1, p. 15, 2015. DOI: 10.1146/annurev-conmatphys-031214-014726.

[163] C. L. Baldwin, C. R. Laumann, A. Pal, and A. Scardicchio, "The many-body localized phase of the quantum random energy model," *Phys. Rev. B*, vol. 93, no. 2, p. 024 202, 2016. DOI: 10.1103/PhysRevB.93.024202.

[164] G. Mossi and A. Scardicchio, "Ergodic and localized regions in quantum spin glasses on the Bethe lattice," *Philos. Trans. R. Soc. London A*, vol. 375, no. 2108, p. 20 160 424, 2017. DOI: 10.1098/rsta.2016.0424.

[165] D. A. Abanin and Z. Papić, "Recent progress in many-body localization," *Ann. Phys.*, vol. 529, no. 7, p. 1 700 169, 2017. DOI: 10.1002/andp.201700169.

[166] J. Z. Imbrie, V. Ros, and A. Scardicchio, "Local integrals of motion in many-body localized systems," *Ann. Phys.*, vol. 529, no. 7, p. 1 600 278, 2017. DOI: 10.1002/andp.201600278.

[167] A. Chandran, I. H. Kim, G. Vidal, and D. A. Abanin, "Constructing local integrals of motion in the many-body localized phase," *Phys. Rev. B*, vol. 91, no. 8, p. 085 425, 2015. DOI: 10.1103/PhysRevB.91.085425.

[168] C. L. Baldwin and C. R. Laumann, "Quantum algorithm for energy matching in hard optimization problems," *Phys. Rev. B*, vol. 97, no. 22, p. 224 201, 2018. DOI: 10.1103/PhysRevB.97.224201.

[169] V. N. Smelyanskiy, K. Kechedzhi, S. Boixo, S. V. Isakov, H. Neven, and B. Altshuler, "Nonergodic delocalized states for efficient population transfer within a narrow band of the energy landscape," *Phys. Rev. X*, vol. 10, no. 1, p. 011 017, 2020. DOI: 10.1103/PhysRevX.10.011017.

[170] Z. Nussinov, P. Johnson, M. J. Graf, and A. V. Balatsky, "Mapping between finite temperature classical and zero temperature quantum systems: Quantum critical jamming and quantum dynamical heterogeneities," *Phys. Rev. B*, vol. 87, no. 18, p. 184 202, 2013. DOI: 10.1103/PhysRevB.87.184202.

[171] M. Lewenstein, "Quantum perceptrons," *J. Mod. Opt.*, vol. 41, no. 12, p. 2491, 1994. DOI: 10.1080/09500349414552331.

[172] G. Schehr, "Low-temperature specific heat of some quantum mean-field glassy phases," *Phys. Rev. B*, vol. 71, no. 18, p. 184 204, 2005. DOI: 10.1103/PhysRevB.71.184204.

[173] A. Andreanov and M. Müller, "Long-range quantum ising spin glasses at t= 0: Gapless collective excitations and universality," *Phys. Rev. Lett.*, vol. 109, no. 17, p. 177 201, 2012. DOI: 10.1103/PhysRevLett.109.177201.

[174] A. Young, "Stability of the quantum Sherrington-Kirkpatrick spin glass model," *Phys. Rev. E*, vol. 96, no. 3, p. 032 112, 2017. DOI: 10.1103/PhysRevE.96.032112.

[175] G. Biroli and L. F. Cugliandolo, "Quantum Thouless-Anderson-Palmer equations for glassy systems," *Phys. Rev. B*, vol. 64, no. 1, p. 014 206, 2001. DOI: 10.1103/PhysRevB.64.014206.

[176] L. F. Cugliandolo, D. R. Grempel, and C. A. da Silva Santos, "Imaginary-time replica formalism study of a quantum spherical p-spin-glass model," *Phys. Rev. B*, vol. 64, no. 1, p. 014 403, 2001. DOI: 10.1103/PhysRevB.64.014403.

[177] S. Sachdev, *Quantum Phase Transitions*. Cambridge University Press, 1999.

[178] J. Reinisch and A. Heuer, "Local properties of the potential-energy landscape of a model glass: Understanding the low-temperature anomalies," *Phys. Rev. B*, vol. 70, no. 6, p. 064 201, 2004.

[179] ——, "What is moving in silica at 1 K? a computer study of the low-temperature anomalies," *Phys. Rev. Lett.*, vol. 95, no. 15, p. 155 502, 2005. DOI: 10.1103/PhysRevB.70.064201.

[180] P. W. Anderson, "Absence of diffusion in certain random lattices," *Phys. Rev.*, vol. 109, no. 5, p. 1492, 1958. DOI: 10.1103/PhysRev.109.1492.

[181] E. Abrahams, *50 years of Anderson Localization*. World Scientific, 2010, vol. 24.

[182] I. V. Gornyi, A. D. Mirlin, and D. G. Polyakov, "Interacting electrons in disordered wires: Anderson localization and low-t transport," *Phys. Rev. Lett.*, vol. 95, no. 20, p. 206 603, 2005. DOI: 10.1103/PhysRevLett.95.206603.

[183] D. Basko, I. Aleiner, and B. Altshuler, "Metal–insulator transition in a weakly interacting many-electron system with localized single-particle states," *Ann. Phys.*, vol. 321, no. 5, pp. 1126–1205, 2006. DOI: 10.1016/j.aop.2005.11.014.

[184] J. M. Deutsch, "Quantum statistical mechanics in a closed system," *Phys. Rev. A*, vol. 43, no. 4, p. 2046, 1991. DOI: 10.1103/PhysRevA.43.2046.

[185] M. Srednicki, "Chaos and quantum thermalization," *Phys. Rev. E*, vol. 50, no. 2, p. 888, 1994. DOI: 10.1103/PhysRevE.50.888.

[186] M. Rigol, V. Dunjko, and M. Olshanii, "Thermalization and its mechanism for generic isolated quantum systems," *Nature*, vol. 452, no. 7189, p. 854, 2008. DOI: 10.1038/nature06838.

[187] L. D'Alessio, Y. Kafri, A. Polkovnikov, and M. Rigol, "From quantum chaos and eigenstate thermalization to statistical mechanics and thermodynamics," *Adv. Phys.*, vol. 65, no. 3, p. 239, 2016. DOI: 10.1080/00018732.2016.1198134.

[188] M. Rigol and M. Srednicki, "Alternatives to eigenstate thermalization," *Phys. Rev. Lett.*, vol. 108, no. 11, p. 110 601, 2012. DOI: 10.1103/PhysRevLett.108.110601.

[189] A. D. Luca and A. Scardicchio, "Ergodicity breaking in a model showing many-body localization," *Europhys. Lett.*, vol. 101, no. 3, p. 37 003, 2013. DOI: 10.1209/0295-5075/101/37003.

[190] D. A. Huse, R. Nandkishore, and V. Oganesyan, "Phenomenology of fully many-body-localized systems," *Phys. Rev. B*, vol. 90, no. 17, p. 174 202, 2014. DOI: 10.1103/PhysRevB.90.174202.

[191] D. J. Luitz, N. Laflorencie, and F. Alet, "Many-body localization edge in the random-field heisenberg chain," *Phys. Rev. B*, vol. 91, no. 8, p. 081 103, 2015. DOI: 10.1103/PhysRevB.91.081103.

[192] M. Serbyn, Z. Papić, and D. A. Abanin, "Criterion for many-body localization-delocalization phase transition," *Phys. Rev. X*, vol. 5, no. 4, p. 041 047, 2015. DOI: 10.1103/PhysRevX.5.041047.

[193] J. Z. Imbrie, "On many-body localization for quantum spin chains," *J. Stat. Phys.*, vol. 163, no. 5, p. 998, 2016. DOI: 10.1007/s10955-016-1508-x.

[194] ——, "Diagonalization and many-body localization for a disordered quantum spin chain," *Phys. Rev. Lett.*, vol. 117, no. 2, p. 027 201, 2016. DOI: 10.1103/PhysRevLett.117.027201.

[195] M. Serbyn, Z. Papić, and D. A. Abanin, "Thouless energy and multifractality across the many-body localization transition," *Phys. Rev. B*, vol. 96, no. 10, p. 104 201, 2017. DOI: 10.1103/PhysRevB.96.104201.

[196] J.-Y. Choi, S. Hild, J. Zeiher, P. Schauß, A. Rubio-Abadal, T. Yefsah, V. Khemani, D. A. Huse, I. Bloch, and C. Gross, "Exploring the many-body localization transition in two dimensions," *Science*, vol. 352, no. 6293, p. 1547, 2016. DOI: 10.1126/science.aaf8834.

[197] D. A. Abanin, E. Altman, I. Bloch, and M. Serbyn, "Colloquium: Many-body localization, thermalization, and entanglement," *Rev. Mod. Phys.*, vol. 91, no. 2, p. 021 001, 2019. DOI: 10.1103/RevModPhys.91.021001.

[198] M. Žnidarič, T. Prosen, and P. Prelovšek, "Many-body localization in the heisenberg XXZ magnet in a random field," *Phys. Rev. B*, vol. 77, no. 6, p. 064 426, 2008. DOI: 10.1103/PhysRevB.77.064426.

[199] A. Pal and D. A. Huse, "Many-body localization phase transition," *Phys. Rev. B*, vol. 82, no. 17, p. 174 411, 2010. DOI: 10.1103/PhysRevB.82.174411.

[200] T. C. Berkelbach and D. R. Reichman, "Conductivity of disordered quantum lattice models at infinite temperature: Many-body localization," *Phys. Rev. B*, vol. 81, no. 22, p. 224 429, 2010. DOI: 10.1103/PhysRevB.81.224429.

[201] J. A. Kjäll, J. H. Bardarson, and F. Pollmann, "Many-body localization in a disordered quantum ising chain," *Phys. Rev. Lett.*, vol. 113, no. 10, p. 107 204, 2014. DOI: 10.1103/PhysRevLett.113.107204.

[202] M. Brenes, M. Dalmonte, M. Heyl, and A. Scardicchio, "Many-body localization dynamics from gauge invariance," *Phys. Rev. Lett.*, vol. 120, no. 3, p. 030 601, 2018. DOI: 10.1103/PhysRevLett.120.030601.

[203] M. Schreiber, S. S. Hodgman, P. Bordia, H. P. Lüschen, M. H. Fischer, R. Vosk, E. Altman, U. Schneider, and I. Bloch, "Observation of many-body localization of interacting fermions in a quasirandom optical lattice," *Science*, vol. 349, no. 6250, p. 842, 2015. DOI: 10.1126/science.aaa7432.

[204] P. Bordia, H. P. Lüschen, S. S. Hodgman, M. Schreiber, I. Bloch, and U. Schneider, "Coupling identical one-dimensional many-body localized systems," *Phys. Rev. Lett.*, vol. 116, no. 14, p. 140 401, 2016. DOI: 10.1103/PhysRevLett.116.140401.

[205] J. Smith, A. Lee, P. Richerme, B. Neyenhuis, P. W. Hess, P. Hauke, M. Heyl, D. A. Huse, and C. Monroe, "Many-body localization in a quantum simulator with programmable random disorder," *Nature Phys.*, vol. 12, no. 10, p. 907, 2016. DOI: 10.1038/NPHYS3783.

[206] A. Lukin, M. Rispoli, R. Schittko, M. E. Tai, A. M. Kaufman, S. Choi, V. Khemani, J. Léonard, and M. Greiner, "Probing entanglement in a many-body–localized system," *Science*, vol. 364, no. 6437, p. 256, 2019. DOI: 10.1126/science.aau0818.

[207] S. Kondov, W. McGehee, W. Xu, and B. DeMarco, "Disorder-induced localization in a strongly correlated atomic hubbard gas," *Phys. Rev. Lett.*, vol. 114, no. 8, p. 083 002, 2015. DOI: 10.1103/PhysRevLett.114.083002.

[208] P. Bordia, H. Lüschen, S. Scherg, S. Gopalakrishnan, M. Knap, U. Schneider, and I. Bloch, "Probing slow relaxation and many-body localization in two-dimensional quasiperiodic systems," *Phys. Rev. X*, vol. 7, no. 4, p. 041 047, 2017. DOI: 10.1103/PhysRevX.7.041047.

[209] W. De Roeck and J. Z. Imbrie, "Many-body localization: Stability and instability," *Philos. Trans. R. Soc. A*, vol. 375, no. 2108, p. 20 160 422, 2017. DOI: 10.1098/rsta.2016.0422.

[210] D. J. Luitz, F. Huveneers, and W. De Roeck, "How a small quantum bath can thermalize long localized chains," *Phys. Rev. Lett.*, vol. 119, no. 15, p. 150 602, 2017. DOI: 10.1103/PhysRevLett.119.150602.

[211] P. Ponte, C. Laumann, D. A. Huse, and A. Chandran, "Thermal inclusions: How one spin can destroy a many-body localized phase," *Phil. Trans. R. Soc. A*, vol. 375, no. 2108, p. 20 160 428, 2017. DOI: 10.1098/rsta.2016.0428.

[212] G. De Tomasi, F. Pollmann, and M. Heyl, "Efficiently solving the dynamics of many-body localized systems at strong disorder," *Phys. Rev. B*, vol. 99, no. 24, p. 241 114, 2019. DOI: 10.1103/PhysRevB.99.241114.

[213] I.-D. Potirniche, S. Banerjee, and E. Altman, "Exploration of the stability of many-body localization in $d > 1$," *Phys. Rev. B*, vol. 99, no. 20, p. 205 149, 2019. DOI: 10.1103/PhysRevB.99.205149.

[214] T. B. Wahl, A. Pal, and S. H. Simon, "Signatures of the many-body localized regime in two dimensions," *Nat. Phys.*, vol. 15, no. 2, p. 164, 2019. DOI: 10.1038/s41567-018-0339-x.

[215] H. Théveniaut, Z. Lan, G. Meyer, and F. Alet, "Transition to a many-body localized regime in a two-dimensional disordered quantum dimer model," *Phys. Rev. R*, vol. 2, no. 3, p. 033 154, 2020. DOI: 10.1103/PhysRevResearch.2.033154.

[216] M. Ovadia, D. Kalok, I. Tamir, S. Mitra, B. Sacépé, and D. Shahar, "Evidence for a finite-temperature insulator," *Sci. Rep.*, vol. 5, no. 1, p. 1, 2015. DOI: 10.1038/srep13503.

[217] K. X. Wei, C. Ramanathan, and P. Cappellaro, "Exploring localization in nuclear spin chains," *Phys. Rev. Lett.*, vol. 120, no. 7, p. 070 501, 2018. DOI: 10.1103/PhysRevLett.120.070501.

[218] D. M. Silevitch, C. Tang, G. Aeppli, and T. F. Rosenbaum, "Tuning high-q nonlinear dynamics in a disordered quantum magnet," *Nature Comm.*, vol. 10, no. 1, p. 1, 2019. DOI: 10.1038/s41467-019-11985-1.

[219] M. Serbyn, Z. Papić, and D. A. Abanin, "Local conservation laws and the structure of the many-body localized states," *Phys. Rev. Lett.*, vol. 111, no. 12, p. 127 201, 2013. DOI: 10.1103/PhysRevLett.111.127201.

[220] V. Ros, M. Müller, and A. Scardicchio, "Integrals of motion in the many-body localized phase," *Nucl. Phys. B*, vol. 891, p. 420, 2015. DOI: 10.1016/j.nuclphysb.2014.12.014.

[221] T. E. O'Brien, D. A. Abanin, G. Vidal, and Z. Papić, "Explicit construction of local conserved operators in disordered many-body systems," *Phys. Rev. B*, vol. 94, no. 14, p. 144 208, 2016. DOI: 10.1103/PhysRevB.94.144208.

[222] A. Chandran, A. Pal, C. Laumann, and A. Scardicchio, "Many-body localization beyond eigenstates in all dimensions," *Phys. Rev. B*, vol. 94, no. 14, p. 144 203, 2016. DOI: 10.1103/PhysRevB.94.144203.

[223] V. K. Varma, A. Raj, S. Gopalakrishnan, V. Oganesyan, and D. Pekker, "Length scales in the many-body localized phase and their spectral signatures," *Phys. Rev. B*, vol. 100, no. 11, p. 115 136, 2019. DOI: 10.1103/PhysRevB.100.115136.

[224] P. Peng, Z. Li, H. Yan, K. X. Wei, P. Cappellaro, *et al.*, "Comparing many-body localization lengths via nonperturbative construction of local integrals of motion," *Phys. Rev. B*, vol. 100, no. 21, p. 214 203, 2019. DOI: 10.1103/PhysRevB.100.214203.

[225] Y. B. Lev and D. R. Reichman, "Dynamics of many-body localization," *Phys. Rev. B*, vol. 89, no. 22, p. 220 201, 2014. DOI: 10.1103/PhysRevB.89.220201.

[226] K. Agarwal, S. Gopalakrishnan, M. Knap, M. Müller, and E. Demler, "Anomalous diffusion and griffiths effects near the many-body localization transition," *Phys. Rev. Lett.*, vol. 114, no. 16, p. 160 401, 2015. DOI: 10.1103/PhysRevLett.114.160401.

[227] M. Žnidarič, A. Scardicchio, and V. K. Varma, "Diffusive and subdiffusive spin transport in the ergodic phase of a many-body localizable system," *Phys. Rev. Lett.*, vol. 117, no. 4, p. 040 601, 2016. DOI: 10.1103/PhysRevLett.117.040601.

[228] V. K. Varma, A. Lerose, F. Pietracaprina, J. Goold, and A. Scardicchio, "Energy diffusion in the ergodic phase of a many body localizable spin chain," *J. Stat. Mech.*, vol. 2017, no. 5, p. 053 101, 2017. DOI: 10.1088/1742-5468/aa668b.

[229] I. Khait, S. Gazit, N. Y. Yao, and A. Auerbach, "Spin transport of weakly disordered heisenberg chain at infinite temperature," *Phys. Rev. B*, vol. 93, no. 22, p. 224 205, 2016. DOI: 10.1103/PhysRevB.93.224205.

[230] J. H. Bardarson, F. Pollmann, and J. E. Moore, "Unbounded growth of entanglement in models of many-body localization," *Phys. Rev. Lett.*, vol. 109, no. 1, p. 017 202, 2012. DOI: 10.1103/PhysRevLett.109.017202.

[231] M. Serbyn, Z. Papić, and D. A. Abanin, "Universal slow growth of entanglement in interacting strongly disordered systems," *Phys. Rev. Lett.*, vol. 110, no. 26, p. 260 601, 2013. DOI: 10.1103/PhysRevLett.110.260601.

[232] A. Nanduri, H. Kim, and D. A. Huse, "Entanglement spreading in a many-body localized system," *Phys. Rev. B*, vol. 90, no. 6, p. 064 201, 2014. DOI: 10.1103/PhysRevB.90.064201.

[233] M. Serbyn, Z. Papić, and D. A. Abanin, "Quantum quenches in the many-body localized phase," *Phys. Rev. B*, vol. 90, no. 17, p. 174 302, 2014. DOI: 10.1103/PhysRevB.90.174302.

[234] M. Serbyn, A. A. Michailidis, D. A. Abanin, and Z. Papić, "Power-law entanglement spectrum in many-body localized phases," *Phys. Rev. Lett.*, vol. 117, no. 16, p. 160 601, 2016. DOI: 10.1103/PhysRevLett.117.160601.

[235] M. Žnidarič, "Entanglement in a dephasing model and many-body localization," *Phys. Rev. B*, vol. 97, no. 21, p. 214 202, 2018. DOI: 10.1103/PhysRevB.97.214202.

[236] M. Serbyn, M. Knap, S. Gopalakrishnan, Z. Papić, N. Y. Yao, C. R. Laumann, D. A. Abanin, M. D. Lukin, and E. A. Demler, "Interferometric probes of many-body localization," *Phys. Rev. Lett.*, vol. 113, no. 14, p. 147 204, 2014. DOI: 10.1103/PhysRevLett.113.147204.

[237] H. Kim and D. A. Huse, "Ballistic spreading of entanglement in a diffusive nonintegrable system," *Phys. Rev. Lett.*, vol. 111, no. 12, p. 127 205, 2013. DOI: 10.1103/PhysRevLett.111.127205.

[238] S. Hill and W. K. Wootters, "Entanglement of a pair of quantum bits," *Phys. Rev. Lett.*, vol. 78, no. 26, p. 5022, 1997. DOI: 10.1103/PhysRevLett.78.5022.

[239] W. K. Wootters, "Entanglement of formation of an arbitrary state of two qubits," *Phys. Rev. Lett.*, vol. 80, no. 10, p. 2245, 1998. DOI: 10.1103/PhysRevLett.80.2245.

[240] V. Coffman, J. Kundu, and W. K. Wootters, "Distributed entanglement," *Phys. Rev. A*, vol. 61, no. 5, p. 052 306, 2000. DOI: 10.1103/PhysRevA.61.052306.

[241] L. Amico, R. Fazio, A. Osterloh, and V. Vedral, "Entanglement in many-body systems," *Rev. Mod. Phys.*, vol. 80, no. 2, p. 517, 2008. DOI: 10.1103/RevModPhys.80.517.

[242] F. Iemini, A. Russomanno, D. Rossini, A. Scardicchio, and R. Fazio, "Signatures of many-body localization in the dynamics of two-site entanglement," *Phys. Rev. B*, vol. 94, no. 21, p. 214 206, 2016. DOI: 10.1103/PhysRevB.94.214206.

[243] P. Jurcevic, B. P. Lanyon, P. Hauke, C. Hempel, P. Zoller, R. Blatt, and C. F. Roos, "Quasiparticle engineering and entanglement propagation in a quantum many-body system," *Nature*, vol. 511, no. 7508, p. 202, 2014. DOI: 10.1038/nature13461.

[244] T. Fukuhara, S. Hild, J. Zeiher, P. Schauß, I. Bloch, M. Endres, and C. Gross, "Spatially resolved detection of a spin-entanglement wave in a bose-hubbard chain," *Phys. Rev. Lett.*, vol. 115, no. 3, p. 035 302, 2015. DOI: 10.1103/PhysRevLett.115.035302.

[245] P. Ponte, A. Chandran, Z. Papić, and D. A. Abanin, "Periodically driven ergodic and many-body localized quantum systems," *Ann. Phys.*, vol. 353, p. 196, 2015. DOI: 10.1016/j.aop.2014.11.008.

[246] D. A. Abanin, W. De Roeck, and F. Huveneers, "Theory of many-body localization in periodically driven systems," *Ann. Phys.*, vol. 372, p. 1, 2016. DOI: 10.1016/j.aop.2016.03.010.

[247] J. Zhang, P. Hess, A. Kyprianidis, P. Becker, A. Lee, J. Smith, G. Pagano, I.-D. Potirniche, A. C. Potter, A. Vishwanath, *et al.*, "Observation of a discrete time crystal," *Nature*, vol. 543, no. 7644, p. 217, 2017. DOI: 10.1038/nature21413.

[248] K. Sacha and J. Zakrzewski, "Time crystals: A review," *Rep. Progr. Phys.*, vol. 81, no. 1, p. 016 401, 2017. DOI: 10.1088/1361-6633/aa8b38.

[249] M. Schiulaz and M. Müller, "Ideal quantum glass transitions: Many-body localization without quenched disorder," *AIP Conf. Proc.*, vol. 1610, no. 1, pp. 11–23, 2014. DOI: 10.1063/1.4893505.

[250] Z. Papić, E. M. Stoudenmire, and D. A. Abanin, "Many-body localization in disorder-free systems: The importance of finite-size constraints," *Ann. Phys.*, vol. 362, p. 714, 2015. DOI: 10.1016/j.aop.2015.08.024.

[251] M. Pino, L. B. Ioffe, and B. L. Altshuler, "Nonergodic metallic and insulating phases of josephson junction chains," *Proc. Natl. Acad. Sci. U.S.A.*, vol. 113, no. 3, p. 536, 2015. DOI: 10.1073/pnas.1520033113.

[252] N. Y. Yao, C. R. Laumann, J. I. Cirac, M. D. Lukin, and J. E. Moore, "Quasi-many-body localization in translation-invariant systems," *Phys. Rev. Lett.*, vol. 117, no. 24, p. 240 601, 2016. DOI: 10.1103/PhysRevLett.117.240601.

[253] R. M. Nandkishore and S. L. Sondhi, "Many-body localization with long-range interactions," *Phys. Rev. X*, vol. 7, no. 4, p. 041 021, 2017. DOI: 10.1103/PhysRevX.7.041021.

[254] M. Schulz, C. A. Hooley, R. Moessner, and F. Pollmann, "Stark many-body localization," *Phys. Rev. Lett.*, vol. 122, no. 4, p. 040 606, 2019. DOI: 10.1103/PhysRevLett.122.040606.

[255] E. van Nieuwenburg, Y. Baum, and G. Refael, "From bloch oscillations to many-body localization in clean interacting systems," *Proc. Natl. Acad. Sci. U.S.A.*, vol. 116, no. 19, p. 9269, 2019. DOI: 10.1073/pnas.1819316116.

[256] G. Giudici, F. M. Surace, J. E. Ebot, A. Scardicchio, and M. Dalmonte, "Breakdown of ergodicity in disordered $U(1)$ lattice gauge theories," *Phys. Rev. Res.*, vol. 2, no. 3, p. 032 034, 2020. DOI: 10.1103/PhysRevResearch.2.032034.

[257] R. Nandkishore, S. Gopalakrishnan, and D. A. Huse, "Spectral features of a many-body-localized system weakly coupled to a bath," *Phys. Rev. B*, vol. 90, no. 6, p. 064 203, 2014. DOI: 10.1103/PhysRevB.90.064203.

[258] E. Levi, M. Heyl, I. Lesanovsky, and J. P. Garrahan, "Robustness of many-body localization in the presence of dissipation," *Phys. Rev. Lett.*, vol. 116, no. 23, p. 237 203, 2016. DOI: 10.1103/PhysRevLett.116.237203.

[259] M. H. Fischer, M. Maksymenko, and E. Altman, "Dynamics of a many-body-localized system coupled to a bath," *Phys. Rev. Lett.*, vol. 116, no. 16, p. 160 401, 2016. DOI: 10.1103/PhysRevLett.116.160401.

[260] M. V. Medvedyeva, T. Prosen, and M. Žnidarič, "Influence of dephasing on many-body localization," *Phys. Rev. B*, vol. 93, no. 9, p. 094 205, 2016. DOI: 10.1103/PhysRevB.93.094205.

[261] B. Everest, I. Lesanovsky, J. P. Garrahan, and E. Levi, "Role of interactions in a dissipative many-body localized system," *Phys. Rev. B*, vol. 95, no. 2, p. 024 310, 2017. DOI: 10.1103/PhysRevB.95.024310.

[262] R. Nandkishore and S. Gopalakrishnan, "Many body localized systems weakly coupled to baths," *Ann. Phys.*, vol. 529, no. 7, p. 1 600 181, 2017. DOI: 10.1002/andp.201600181.

[263] I. Vakulchyk, I. Yusipov, M. Ivanchenko, S. Flach, and S. Denisov, "Signatures of many-body localization in steady states of open quantum systems," *Phys. Rev. B*, vol. 98, no. 2, p. 020 202, 2018. DOI: 10.1103/PhysRevB.98.020202.

[264] S. Gopalakrishnan and S. Parameswaran, "Dynamics and transport at the threshold of many-body localization," *Phys. Rep.*, vol. 862, pp. 1–62, 2020. DOI: 10.1016/j.physrep.2020.03.003.

[265] E. Wybo, M. Knap, and F. Pollmann, "Entanglement dynamics of a many-body localized system coupled to a bath," *Phys. Rev. B*, vol. 102, no. 6, p. 064 304, 2020. DOI: 10.1103/PhysRevB.102.064304.

[266] C. Artiaco, F. Balducci, and A. Scardicchio, "Signatures of many-body localization in the dynamics of two-level systems in glasses," *Phys. Rev. B*, vol. 103, no. 21, p. 214 205, 2021. DOI: 10.1103/PhysRevB.103.214205.

[267] F. Mahmood, D. Chaudhuri, S. Gopalakrishnan, R. Nandkishore, and N. Armitage, "Observation of a marginal Fermi glass," *Nat. Phys.*, vol. 17, no. 5, p. 627, 2021. DOI: 10.1038/s41567-020-01149-0.

[268] B. Ruzicka, T. Scopigno, S. Caponi, A. Fontana, O. Pilla, P. Giura, G. Monaco, E. Pontecorvo, G. Ruocco, and F. Sette, "Evidence of anomalous dispersion of the generalized sound velocity in glasses," *Phys. Rev. B*, vol. 69, no. 10, p. 100 201, 2004. DOI: 10.1103/PhysRevB.69.100201.

[269] J. F. Berret and M. Meißner, "How universal are the low temperature acoustic properties of glasses?" *Z. Phys. B*, vol. 70, no. 1, p. 65, 1988. DOI: 10.1007/BF01320540.

[270] S. Hunklinger and A. Raychaudhuri, "Chapter 3: Thermal and elastic anomalies in glasses at low temperatures," in, ser. Progress in Low Temperature Physics, D. Brewer, Ed., vol. 9, Elsevier, 1986, p. 265. DOI: 10.1016/S0079-6417(08)60015-3.

[271] H.-P. Breuer and F. Petruccione, *The Theory of Open Quantum Systems*. Oxford University Press, 2007, p. 656. DOI: 10.1093/acprof:oso/9780199213900.001.0001.

[272] D. Manzano, "A short introduction to the Lindblad master equation," *AIP Adv.*, vol. 10, no. 2, p. 025 106, 2020. DOI: 10.1063/1.5115323.

[273] V. Gorini, A. Kossakowski, and E. C. G. Sudarshan, "Completely positive dynamical semigroups of n-level systems," *J. Math. Phys.*, vol. 17, no. 5, p. 821, 1976. DOI: 10.1063/1.522979.

[274] G. Lindblad, "On the generators of quantum dynamical semigroups," *Commun. Math. Phys.*, vol. 48, no. 2, p. 119, 1976. DOI: 10.1007/BF01608499.

[275] D. Chruściński and S. Pascazio, "A brief history of the GKLS equation," *arXiv:1710.05993*, 2017. DOI: 10.1142/S1230161217400017.

[276] N. Y. Yao, C. R. Laumann, S. Gopalakrishnan, M. Knap, M. Müller, E. A. Demler, and M. D. Lukin, "Many-body localization in dipolar systems," *Phys. Rev. Lett.*, vol. 113, no. 24, p. 243 002, 2014. DOI: 10.1103/PhysRevLett.113.243002.

[277] A. L. Burin, "Many-body delocalization in a strongly disordered system with long-range interactions: Finite-size scaling," *Phys. Rev. B*, vol. 91, no. 9, p. 094 202, 2015. DOI: 10.1103/PhysRevB.91.094202.

[278] X. Deng, A. L. Burin, and I. M. Khaymovich, "Anisotropy-mediated reentrant localization," *arXiv:2002.00013*, 2020.

[279] M. Pino, "Entanglement growth in many-body localized systems with long-range interactions," *Phys. Rev. B*, vol. 90, no. 17, p. 174 204, 2014. DOI: 10.1103/PhysRevB.90.174204.

[280] C. Artiaco, F. Balducci, M. Fabrizio, and A. Scardicchio, "Signatures of many-body localization in the dynamics of two-level systems in glasses in the strong-coupling limit," *In preparation*, 2021.

[281] C. Artiaco, F. Balducci, M. Heyl, A. Russomanno, and A. Scardicchio, "Spatio-temporal heterogeneities of entanglement in the many-body localized phase," *arXiv:2108.05594*, 2021.

[282] A. Vulpiani, M. Falcioni, and P. Castiglione, *Chaos and Coarse Graining in Statistical Mechanics*. Cambridge University Press, 2008.

[283] A. J. Lichtenberg and M. A. Lieberman, *Regular and chaotic dynamics*. Springer, 2013, vol. 38.

[284] M. V. Berry, "Regular and irregular motion," *AIP Conf. Proc.*, vol. 46, no. 1, p. 16, 1978. DOI: 10.1063/1.31417.

[285] A. Polkovnikov, K. Sengupta, A. Silva, and M. Vengalattore, "Colloquium: Nonequilibrium dynamics of closed interacting quantum systems," *Rev. Mod. Phys.*, vol. 83, no. 3, p. 863, 2011. DOI: 10.1103/RevModPhys.83.863.

[286] M. A. Nielsen and I. L. Chuang, *Quantum Computation and Quantum Information*. Cambridge University Press, 2010. DOI: 10.1017/CBO9780511976667.

[287] P. Facchi, G. Florio, G. Parisi, and S. Pascazio, "Maximally multipartite entangled states," *Phys. Rev. A*, vol. 77, no. 6, p. 060 304, 2008. DOI: 10.1103/PhysRevA.77.060304.

[288] P. Facchi, G. Florio, U. Marzolino, G. Parisi, and S. Pascazio, "Multipartite entanglement and frustration," *New J. Phys.*, vol. 12, no. 2, p. 025 015, 2010. DOI: 10.1088/1367-2630/12/2/025015.

[289] G. De Chiara, S. Montangero, P. Calabrese, and R. Fazio, "Entanglement entropy dynamics of Heisenberg chains," *J. Stat. Mech.*, vol. 2006, no. 03, P03001, 2006. DOI: 10.1088/1742-5468/2006/03/p03001.

[290] F. Pietracaprina, G. Parisi, A. Mariano, S. Pascazio, and A. Scardicchio, "Entanglement critical length at the many-body localization transition," *J. Stat. Mech.*, vol. 2017, no. 11, p. 113 102, 2017. DOI: 10.1088/1742-5468/aa9338.

[291] J. Goold, C. Gogolin, S. R. Clark, J. Eisert, A. Scardicchio, and A. Silva, "Total correlations of the diagonal ensemble herald the many-body localization transition," *Phys. Rev. B*, vol. 92, no. 18, p. 180 202, 2015. DOI: 10.1103/PhysRevB.92.180202.

[292] B. Olmos, I. Lesanovsky, and J. P. Garrahan, "Facilitated spin models of dissipative quantum glasses," *Phys. Rev. Lett.*, vol. 109, no. 2, p. 020 403, 2012. DOI: 10.1103/PhysRevLett.109.020403.

[293] Z. Lan, M. van Horssen, S. Powell, and J. P. Garrahan, "Quantum slow relaxation and metastability due to dynamical constraints," *Phys. Rev. Lett.*, vol. 121, no. 4, p. 040 603, 2018. DOI: 10.1103/PhysRevLett.121.040603.

[294] B. Derrida, "Random-energy model: An exactly solvable model of disordered systems," *Phys. Rev. B*, vol. 24, no. 5, p. 2613, 1981. DOI: 10.1103/PhysRevB.24.2613.

[295] F. Alet and N. Laflorencie, "Many-body localization: An introduction and selected topics," *Compt. Rend. Phys.*, vol. 19, no. 6, p. 498, 2018. DOI: 10.1016/j.crhy.2018.03.003.

[296] R. B. Sidje, "Expokit: A software package for computing matrix exponentials," *ACM Trans. Math. Softw.*, vol. 24, no. 1, p. 130, 1998. DOI: 10.1145/285861.285868.

[297] S. Lloyd and H. Pagels, "Complexity as thermodynamic depth," *Ann. Phys.*, vol. 188, no. 1, p. 186, 1988. DOI: 10.1016/0003-4916(88)90094-2.

[298] D. N. Page, "Average entropy of a subsystem," *Phys. Rev. Lett.*, vol. 71, no. 9, p. 1291, 1993. DOI: 10.1103/PhysRevLett.71.1291.

[299] G. Grosso and G. Pastori Parravicini, *Solid State Physics*, Second Edition. Academic Press, 2014. DOI: 10.1016/B978-0-12-385030-0.00020-7.